Doctoral thesis

Indian Institute of Technology Guwahati

Development of an affordable and state-of-art optical super-resolution imaging system utilizing stochastic optical reconstruction microscopy

Anupam Bharadwaj

Optical Imaging Laboratory, Department of Physics,

Indian Institute of Technology Guwahati,

Guwahati-781039, Assam, India

2026

DOCTORAL THESIS

INDIAN INSTITUTE OF TECHNOLOGY GUWAHATI

Development of an affordable and state-of-art optical super-resolution imaging system utilizing stochastic optical reconstruction microscopy

Thesis submitted in partial fulfillment of the requirements for the degree of

Doctor of Philosophy

of the

Indian Institute of Technology Guwahati.

by

Anupam Bharadwaj

Thesis Supervisor: **Prof. Bosanta R. Boruah**

Optical Imaging Laboratory, Department of Physics,
Indian Institute of Technology Guwahati,
Guwahati-781039, Assam, India.

2026

Dedicated to my beloved parents

Observation, reason and experiment make up what we call the scientific method.

– Richard P. Feynman

Declaration

Mr Anupam Bharadwaj
Roll No.: 196121101
Department of Physics,
Indian Institute of Technology Guwahati,
Guwahati-781039, Assam, India.
E-mail: abharadwaj@iitg.ac.in

I now declare that the findings in this thesis are based on experiments I carried out under Prof. Bosanta Ranjan Boruah's supervision at the Department of Physics, Indian Institute of Technology Guwahati, Guwahati, India. This thesis has not been submitted to any other university, institute, or organization to confer a degree, diploma, or associateship.

Anupam Bharadwaj

Date: 2026-07-01

Certificate

Prof. Bosanta Ranjan Boruah
Department of Physics,
Indian Institute of Technology Guwahati,
Guwahati-781039, Assam, India.
Phone: (+91) 361-258-2725 (O)
E-mail: brboruah@iitg.ac.in

This is to certify that the work presented in the thesis titled **'Development of an affordable and state-of-art optical super-resolution imaging system utilizing stochastic optical reconstruction microscopy'**, authored by **Anupam Bharadwaj** (Roll No. 196121101), a student of the Department of Physics at the Indian Institute of Technology Guwahati, has been conducted under my supervision in fulfillment of the requirements for the degree of Doctor of Philosophy.

This thesis, in its entirety or in part, has not been submitted for consideration for another associateship, diploma, or degree elsewhere.

Bosanta R. Boruah

Date: 2026-07-01

Acknowledgments

I sincerely thank my supervisor, Prof. Bosanta R. Boruah, for his unwavering support, inspiration, and insightful guidance throughout my doctoral studies, which greatly strengthened my understanding of the research and helped me overcome every technical challenge.

I am deeply thankful to Prof. Bithiah G. Jaganathan for her mentorship during sample preparation and for providing access to her laboratory facilities.

I also extend my gratitude to my doctoral committee members, Prof. Tarak Nath Dey, Prof. Ashwini Kumar, and Prof. Bithiah G. Jaganathan, for their constructive feedback and encouragement during my progress presentations and overall. My sincere thanks to the Heads of the Department, departmental staff, and the technical team for their constant support, and to the Ministry of Education (formerly the Ministry of Human Resource Development (MHRD)), India, for providing the fellowship through IIT Guwahati.

I gratefully acknowledge the collaboration with the Imperial College London group, especially Prof. Paul M. W. French, Prof. Mark Neil, Prof. Christopher Dunsby, Sunil Kumar, Edwin Garcia, and Jonathan Lightley, whose insightful discussions enriched this work. Special thanks to Dr. Anupam Sarma (B. Borroah Cancer Research Institute) for providing essential histopathology samples, Dr. Ranjan Kalita for help with the openFrame setup, and Dr. Amalesh Kumar, Amit Sharma, Rumela Mitra, and Sam P. Matthew for their assistance in biological sample preparation. I would also like to take this opportunity to thank my colleagues and friends, especially Saraswati, Pranjal, Shilpa, Neeraj, Nimish, Pawan, Bishnu, and Deepjyoti, for their support and encouragement during my PhD journey.

Beyond direct mentorship, I wish to acknowledge the profound inspiration drawn from Prof. Richard P. Feynman, whom I never had the privilege of meeting, yet whose enthusiasm for science, lucid teachings, timeless works, and joyful way of being have continuously motivated me and shaped my approach to learning and research.

Lastly, I would like to sincerely thank my family for their unconditional love and unwavering concern for my well-being. I am grateful to my grandparents, Late Dineshwar Sarmah and Chandrika Devi; my parents, Late Kiran Chandra Sarmah and Nirmali Goswami; my sister, Himadree; my uncles, Gajendra and Niranjan; and

my aunt, Binita. I fondly acknowledge the support and affection of my maternal uncle, Late Biswajeet Goswami, and my aunt, Late Kanika Devi, whose presence and guidance during the good old days remain deeply cherished.

This work stands on the support, inspiration, and kindness of many others who may not be named here individually. I thank you all sincerely.

Abstract

Optical microscopy plays a crucial role in biological and biomedical sciences, although its resolving power is fundamentally restricted to ≈ 200 nm due to diffraction. Optical super-resolution microscopy (OSRM) techniques, such as SIM, STED, and STORM, can overcome this barrier and achieve resolutions from about 100 nm down to a few tens of nanometers. However, the high cost and complexity of commercial OSRM systems limit their accessibility in low resource organizations. Besides, in regions such as Asia and the Indian subcontinent, hot and humid climates can significantly impact the performance of OSRM, further exacerbating access. Since STORM can be implemented relatively easily and in an affordable way in a widefield microscope, in this thesis, we develop a modular STORM system based on an open-source microscopy concept. The modular platform, referred to as openFrame, is built using industry-grade components and open-source control software, enabling brightfield, widefield epi-fluorescence, and super-resolution imaging with STORM at a much lower cost compared to the commercial systems. We present sample preparation and preservation protocols for STORM and demonstrate that the developed system operates reliably in sub-tropical environmental conditions. We additionally address a few major challenges in STORM, using this modular platform. First, we introduce a UV-violet assisted photoinduced recovery mechanism that significantly extends the blinking duration of fluorophores in an imaging buffer, namely, Mowiol with β-ME, thereby increasing the number of localizations and improving the image resolution in STORM. We then implement a holographic user-defined illumination scheme that allows excitation of arbitrary regions of interest on the sample plane, leaving other regions unilluminated except the targeted ones and thus enabling spatial time-lapse STORM while minimizing the photodamage of the unilluminated regions. We combine STORM with confocal and image scanning microscopes to get high-resolution and super-resolution images of the same sample region using a single microscope platform. This integration ensures that if STORM fails to reconstruct a super-resolved image, at least a high-resolution image of the beam scanning microscope will be available. Overall, the developments of advanced microscopy demonstrated here expand the reach of state-of-art optical super-resolution imaging to resource limited organizations and provide valuable tools and schemes for biological and biomedical research.

Acronyms

AF - Alexa Fluor
AD - Arduino
ADCF - Analog-to-digital conversion factor
ADU - Analog-to-digital unit
Amp - Ampere
AU - Arbitrary unit
β-ME - Beta-mercaptoethanol
BFP - Back focal plane
BP - Bandpass
CAD - Computer aided design
CGH - Computer generated hologram
CMOS - Complementary metal oxide semiconductor
cm - centimeter
DAC - Digital-to-analog
DBC - Dichroic beam combiner
DBS - Dichroic beam splitter
DL - Diode laser
DLL - Dynamic library link
EMCCD - Electron multiplying charge-coupled device
FBS - Fetal bovine serum
FCA - Fibre coupler adapter
FOV - Field of view
FRC - Fourier ring correlation
fps - Frames per second
FWHM - Full width at half maximum
H&E - Hematoxylin and eosin
ISM - Image scanning microscopy
kW - kilowatt
LCSLM - Liquid crystal spatial light modulator
LD - Laser driver
LED - Light emitting diode
μm - micrometer

MMOF - Multimode optical fibre

mm - millimeter

μL - micro liter

MO - Microscope objective

MSCs - Mesenchymal stem cells

NA - Numerical aperture

nm - nanometer

NTC - Negative temperature coefficient

OSRM - Optical super-resolution microscopy

PBS - Phosphate buffered saline

PC - Personal computer

PH - Pin hole

piSTORM - programmable illumination in stochastic optical reconstruction microscopy

PSF - Point spread function

QE - Quantum efficiency

QD - Quantum dot

ROI - Region of interest

SIM - Structured illumination microscopy

SLM - Spatial light modulator

SMLM - Single molecule localization microscopy

SNR - Signal to noise ratio

STED - Stimulated emission depletion

STORM - Stochastic optical reconstruction microscopy

TEC - Thermoelectric cooler

UV - Ultraviolet

V - Volt

W - Watt

Contents

List of Figures

List of Tables

Chapter 1

Introduction and Overview of the Thesis

1.1 Introduction

Microscopy involves constructing images of objects with finer details that are otherwise impossible to observe with an unassisted eye. An important criterion that determines the useful information present in a microscopic image is the resolution of the imaging system. However, as Abbe suggested in 1873 [1], diffraction limits the resolution of any imaging device. According to Abbe, no imaging device can resolve details smaller than approximately half the wavelength of light used for imaging. As such, obtaining resolution beyond this limit will require specialized microscopy methods or instruments. Once the resolution is obtained beyond the diffraction limit, we achieve super-resolution. In addition to achieving higher resolution, a particular microscopy technique must allow non-invasive imaging and the ability to image dry and wet samples, enabling live cell microscopy applications [2, 3, 4]. In this context, far-field optical microscopy can provide a non invasive approach for imaging of both dry and wet samples, including biological samples. However, a conventional optical microscope can provide resolution up to $\approx$ 200 nm only, due to the diffraction limit. Yet there are many phenomena taking place at a length scale much smaller than the above resolution limit.

Over the past two and a half decades, there have been concerted efforts to improve the resolution limit of optical microscopes beyond the diffraction limit [5]. These methods are collectively named optical super-resolution microscopy (OSRM) techniques. Out of all the reported OSRM techniques, Structured Illumination Microscopy (SIM) [6, 7], Stimulated Emission Depletion (STED) microscopy [8], and single molecule localization techniques such as Stochastic Optical Reconstruction

Microscopy (STORM) [9] are the prominent ones. While SIM provides a significant improvement in resolution compared to conventional widefield microscopes, resolving structures at $\leq$ 100 nm, STED, which is a confocal based technique, and STORM, which is based on widefield microscopy, can achieve resolution at $\leq$ 30 nm. The experimental setup of STED is more complicated and involves spatio-temporal alignment of the excitation beam and depletion beam, which is very crucial. However, STORM can be implemented easily with minimal changes in a conventional widefield microscope, thereby making it more cost-effective compared to the STED microscope. A detailed comparison between these techniques is provided in Chapter 2.

OSRM techniques in recent years have made great strides and helped us in early assessment of cancer, whose number of occurrences, particularly in Asia and the Indian subcontinent, is increasing at an alarming rate. Studies using conventional optical microscopes are not sufficient to reveal the underlying reason behind cancer causing agents. OSRM techniques, with their improved resolution capabilities, can identify and track structural alterations that traditional histopathology tools are unable to detect. In both the pre-diagnosis and post-diagnosis phases, this can greatly assist with the accurate management of the illness. There have already been reports of using super-resolution microscopes in the diagnosis, such as in the pre-stages of breast cancer (HER2 receptor on membrane protrusions in human breast cancer specimens) [10], head and neck cancer [11], and blood cancer (detection of CD19 on myeloma) [12].

However, commercial optical super-resolution microscopes are not easily affordable for the majority of research organizations, clinics, medical and educational labs, even though there is a development of cutting-edge OSRM techniques. According to the tenets of open science [13], the unfulfilled needs of these institutions can be addressed by creating cutting-edge, reasonably priced, scientific-grade optical super-resolution microscopes. Over the last decade, open-source computer programs, software, and hardware platforms for advanced microscopy have made significant strides [14]. These developments could not only lower the cost of hardware and software but also provide both novice and experienced users with the flexibility to modify the already available commercial instruments or build their own system from the basic setup. The open-source approach fosters greater adaptability in microscopy research, enabling users to customize instruments to their specific needs. Additionally, open-source tools offer the advantage of easy maintenance and upgrades, preventing

obsolescence. By integrating the latest advancements, researchers can enhance the longevity and performance of their equipment without relying on proprietary solutions, thereby optimizing costs and efficiency over time. Therefore, developing an affordable and open-source super-resolution microscope, such as STORM, in areas with organizations lacking enough financial resources can facilitate carrying out research work in the area of biological and biomedical sciences, which may contribute to advanced medical diagnosis.

While affordably realizing STORM is crucial for enhancing accessibility, there is also a need to address the important question of the feasibility of its implementation in regions with a hot and humid climate, like the Indian subcontinent. Such a climate can bring serious challenges to the sample preparation/preservation process and the system components, be it optics or electronics [15, 16, 17]. Higher temperature accelerates thermal drift of the sample, as well as evaporation of imaging buffers/media, and accelerates microbial growth on the sample. Humidity, on the other hand, affects the optics and camera sensors by allowing condensation to form on their surfaces. Excess temperature and humidity can also affect the performance of sensitive components present in the sample stage, camera, laser drivers and lasers, leading to malfunctions. Therefore, it is essential to evaluate the implementation and performance of a low-cost STORM scheme despite the above stated challenges.

However, in addition to the affordability and implementation challenges, there are other important challenges that can affect the performance of any STORM system.

The achievable resolution in the reconstructed image of a STORM system depends on the total number of photons detected from a point object, which directly depends on the the number of fluorescence blinking events, which, on the other hand, depends on the duration for which fluorescence blinking continues before the fluorophores get photobleached. Any increase in the fluorescence blinking duration essentially contributes towards improving the image resolution. Therefore, it is imperative to investigate the effect of any external perturbation on the specimen/sample, which might add to the duration of emission or blinking.

In STORM imaging, normally, the entire field of view (FOV) of the sample plane is illuminated, and it is not possible with the current illumination scheme in STORM to illuminate only a user-defined region of interest. Therefore, if the region of interest to be imaged is smaller than the whole illumination area, molecules outside the region of interest may get photobleached. Moreover, different regions

within the same FOV might have different emission intensities, depending on the density of structures of the sample. If these regions are excited with the same excitation intensity simultaneously, then there can be varying levels of brightness across the regions. Thus, it is important in STORM to incorporate a user-defined illumination beam profile to match any arbitrarily shaped region on the sample with spatially varying intensity levels.

As mentioned already, the quality of the super-resolved image in STORM depends on the adequate blinking behavior of each fluorophore. Since the imaging is done in a widefield microscope, if the STORM imaging scheme does not work, the user is left with a diffraction limited fluorescence image of the specimen only. Thus, if the widefield microscope is combined with a scanning microscope by using suitable optics and other hardware components, the user will be able to perform both high-resolution imaging, such as confocal microscopy or image scanning microscopy (ISM) with array detection [18] and STORM of the same specimen. In such a case, if STORM fails to reconstruct a super-resolved image, then the confocal or array detection will produce at least a high-resolution fluorescence image of the same specimen area. Therefore, it will be worth exploring if the STORM setup can be optically combined with a confocal or array detection setup to perform imaging of the same specimen area.

In this thesis, we first describe the implementation of an open-source and affordable advanced optical microscope at IIT Guwahati in a collaborative research with Imperial College London. We leverage a modular microscope platform [19] named as openFrame based on the open microscopy concept, with industry-grade and reasonably priced components and open-source software. The openFrame-based microscope can be developed at a price much lower than the equivalent commercially available microscopes. We demonstrate brightfield and fluorescence imaging in widefield mode and compare the results with commercial optical microscopes. We then implement STORM in the modular microscope as an affordable solution for super-resolved fluorescence imaging and demonstrate STORM imaging of biological specimens in the sub-tropical humid climate. We then employ our openFrame-based STORM setup to address some of the important challenges mentioned above. We propose a UV light based photoinduced recovery mechanism of the fluorophore to significantly increase the blinking duration. We also introduce a holographic illumination beam profile design to enable illumination of an arbitrary user-defined area of interest and thereby perform spatial time-lapse STORM imaging of the sample.

We then demonstrate how the STORM setup can be combined with beam scanning microscope to perform both STORM imaging and confocal or image scanning microscopy of the same specimen.

Below, we present a chapter-wise summary of the thesis.

1.2 Overview of the Thesis Chapters

Chapter 1 serves as a short introduction to optical super-resolution and the need for cost-effective implementation of optical super-resolution microscopy using STORM. The Chapter discusses the challenges in the current state-of-art STORM, the proposed objectives, and finally provides a summary of the thesis's key points.

Chapter 2 provides a general introduction with a brief historical insight into microscopy and why the resolution is important in microscopy. The Chapter further discusses the techniques to go beyond the diffraction limited resolution for obtaining optical super-resolution and the reason behind choosing STORM, especially a sub-variant of STORM, i.e., easySTORM, for our work. It also provides a detailed explanation of working in STORM, which includes the fundamentals, the photoswitching or blinking mechanism, and the image reconstruction process.

Chapter 3 comprehensively describes the development of an affordable modular research-grade optical microscope [19], utilizing accessible electrical components, optics, industry-grade lasers, cameras, and open-source software. To show the performance of the setup, detailed investigations are done on physical targets, biological cells and histopathological tissue sections. The Chapter then compares our results with commercial optical microscopes to show the efficacy of our affordable optical microscope.

Chapter 4 demonstrates the implementation of easySTORM [20] in our affordable modular optical microscope to perform single-color and multi-color imaging on physical and biological structures. It covers in detail the image acquisition steps and image reconstruction process, as well as the sample preparation steps, along with the challenges we faced during the implementation of STORM.

Chapter 5 introduces the photoinduced recovery mechanism [21] in STORM and the experimental validation of resolution enhancement in STORM using this mechanism. It presents different combinations of excitation and the photoinduced recovery beam parameters for the fluorophores in an imaging buffer, so as to obtain the best super-resolved image. In addition to this, the Chapter also reports the application

of our optimized STORM in various human non-cancerous and cancerous cell lines to understand the changes in structural widths of their cytoskeletal elements.

Chapter 6 presents a novel dynamic holographic beam modulation scheme to realize arbitrary and user-defined illumination of the sample plane of a STORM system. The scheme is employed for STORM imaging of both quantum dots and biological specimens and can also be applied to other single molecule localization microscopes. This Chapter also presents the integration of a STORM system with a beam scanning confocal microscope and an image scanning microscope. The working of the combined system is demonstrated by performing STORM, confocal and array scanning imaging of the same area of a quantum dot sample.

Chapter 7 provides a comprehensive summary of the key findings and contributions of this thesis. It also discusses potential directions for future research, including improvements to the current state-of-art, expansion of its applications, and integration with other imaging modalities.

* * *

Chapter 2

Introduction to optical microscopy and optical super-resolution

2.1 Introduction

In physical and biological sciences, microscopy has long been vital because it provides a window into the complex world of microstructures, cells, tissues, and microorganisms. The invention of early magnifying lenses in the late 16th century marked the beginning of microscopy [22]. An important milestone was reached with Zacharias Janssen's invention of the compound microscope [23]. During the ensuing period, prominent individuals like Antonie van Leeuwenhoek, the first person to examine single-celled creatures [24] and Robert Hooke, who first used the term "cell" in his book "Micrographia" in 1665 [25], helped to improve microscopy. Since then, microscopy has continued to evolve with the development of sophisticated imaging technology, making it possible for researchers to see structures normally undetectable to the unassisted human eye.

As mentioned in Chapter 1, resolution in microscopy is an important criterion that defines the amount of important information present in a microscope image. In far-field optical microscopy, the resolution is restricted by the objective lens's ability to capture diffracted light from the sample. Thus, there is a limit on the resolution achievable in different microscopy techniques. For example, in optical microscopy, if violet light is considered as the imaging wavelength, then it is possible to attain a best resolution of $\approx$ 200 nm. However, the invention of the electron microscope in the 1930s, pioneered by Ernst Ruska [26], brought a significant leap in resolution, allowing scientists to view structures at the Angstrom scale. Nevertheless, radiation from the electron microscope is highly destructive to biological samples. Notably,

any radiation below ≈ 400 nm can lead to severe phototoxicity or photobleaching of the samples in biological studies. Thus, optical microscopy with visible radiation is more suitable for biological imaging. Furthermore, the electron microscope only allows imaging of dry and dead samples coated with a thin conducting layer [2, 3], in contrast with the optical microscope, which allows imaging of dry, wet, and living samples. Hence, an optical microscope serves as a suitable alternative for imaging biological samples, including live cells. In the last few decades, there have been several efforts to enhance the resolution of the optical microscope and thereby to be able to see details of the sample beyond the diffraction limit. Such imaging techniques are, in general, termed optical super-resolution microscopy (OSRM) techniques. The current thesis is centered on how a standard optical microscope can be upgraded in an affordable manner to realize imaging beyond the diffraction limit by implementing an OSRM scheme known as stochastic optical reconstruction microscopy (STORM). In this Chapter, we first discuss the resolution limit due to diffraction and how, in recent years, it has been overcome with innovative approaches employing visible wavelengths (≈ 400 nm to 700 nm). We discuss different optical microscopy techniques that can cross the diffraction limit, followed by a discussion on some well-acknowledged advanced imaging techniques that can very easily surpass this limit and achieve true super-resolution. The Chapter then outlines the rationale for choosing STORM as the preferred super-resolution technique in this thesis. The Chapter concludes by describing the fundamentals of STORM, the mechanism of stochastic switching, reconstruction, and different variants of STORM.

2.2 Diffraction limit of resolution

The resolution limit of an imaging system or a microscope can be defined as the distance between two point objects in the sample plane that can be clearly seen or resolved in its image. According to the laws of geometrical optics, the above distance can be infinitely small. However, as a light beam passes through an imaging lens typically having a circular aperture, it undergoes diffraction, due to which a plane wave passing through the lens may not get focused to an infinitesimally small point, but rather to a diffraction limited volume. Abbe in 1873 showed that the resolution limit of an optical microscope due to diffraction is given as $d \approx \lambda/2NA$, where λ is the light wavelength, and NA is the numerical aperture of the objective lens. Hence, the best resolution with an optical microscope, according to Abbe, considering NA=1, is

$\lambda/2$. Rayleigh later stated that the image of a point source, called the point spread function (PSF), due to diffraction through an ideal lens with a circular aperture or the objective lens, would give rise to a pattern known as the Airy function [27]. For two closely spaced point sources, Rayleigh quantified the resolution limit as the minimum distance between them at which the peak of one PSF coincides with the minimum of the other PSF. This distance is given as d $\approx 0.61\lambda/\text{NA}$. An optical microscope that can form images with details below the above stated resolution limits can be termed an optical super-resolution microscope.

2.3 Optical super-resolution microscopy

Optical microscopes can be classified into two categories depending on the type of illumination and imaging of the sample, namely, point scanning and widefield microscopes [28, 29]. In a point scanning microscope, a focused laser beam is used to scan point by point over an area on the sample. Scanning can be performed with mirrors, for example, galvo scanning mirrors [30, 31]. Subsequently, the net reflected or fluorescence signal from each scanned point is recorded on the detector and stored in the computer, which is later processed to construct the final image. Unlike the point scanning microscope, the widefield microscope illuminates an entire area on the sample at a time. The reflected or the fluorescence signal is then captured on the detector as an image. Widefield microscopes are more suitable for two-dimensional imaging than point scanning microscopes. In contrast, point scanning microscopes are more suitable for the depth imaging of thick biological samples. The first approach to touch the diffraction barrier was by Marvin Minsky, who developed a point scanning imaging technique, known as the confocal microscope, in 1957 [32], that can deliver a resolution up to $\approx$ 200 nm in the lateral direction [28]. The confocal technique is based on forming the image by collecting light from the sample plane that passes through a physical pin hole kept in front of the detector and optically conjugate to the sample plane, as shown in Figure 2.1. Owing to the pin hole, there is a significant enhancement in the axial resolution and a marginal enhancement in the lateral resolution. In theory, the best resolution with a confocal microscope is achieved when the diameter of the pin hole is zero. However, this corresponds to no light reaching the detector. Even if the radius of the pinhole is kept very small, it affects the signal to noise ratio (SNR) in the stored data to form the image.

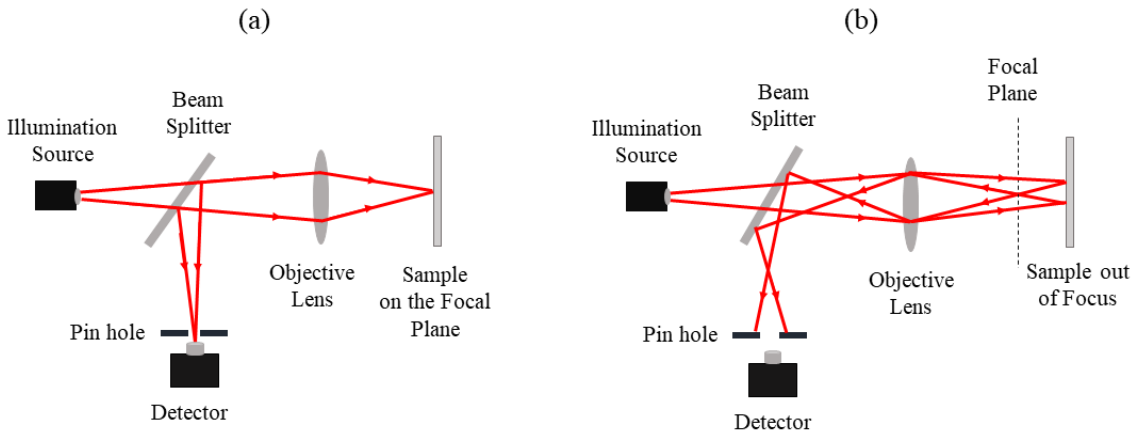

Figure 2.1: Principle of a confocal microscope: (a) The pin hole allows the light from the sample to reach the detector when the sample is on the focal plane. (b) When the sample is out of focus, the same pin hole obstructs the light from reaching the detector.

To resolve the noise issue in the confocal microscope, especially when the pinhole is to be made smaller in order to enhance the resolution performance, image scanning microscopy (ISM) [18] has been proposed. ISM is basically a point scanning microscope with the pinhole and the detector, in the case of a confocal microscope, replaced by an array detector (AD). An array detector can be a digital camera, which images the illumination spot on its array of sensor pixels for each scan position. Pixel reassignment [33] of the data captured with the array detector can help achieve a resolution enhancement by a factor $\sqrt{2}$ relative to the confocal microscope. Figure 2.2 depicts the pixel reassignment process in ISM. The light from the sample plane for each scan position is focused on the camera, and its location in the reconstructed image array, as seen in Figure 2.2 (a), is noted. However, before adding the focal spot at the given location of the image array, the size of the spot is reduced by a factor of two and then added to the given location as seen in Figure 2.2 (b). The above process is then repeated for all scan positions to obtain the reconstructed ISM image. However, achieving a resolution below 100 nm is not possible with either confocal or ISM.

In the last two decades, optical microscopy techniques have progressed further and have been able to circumvent the diffraction barrier, allowing resolution below 100 nm, utilizing either near-field or far-field techniques [9]. Near-field microscopy is usually applicable to fixed samples only, has a small field of view, and can be slow. Thus, in achieving higher resolution and surpassing the diffraction limit, advances in far-field optical microscopy techniques, leading to OSRM, have been more

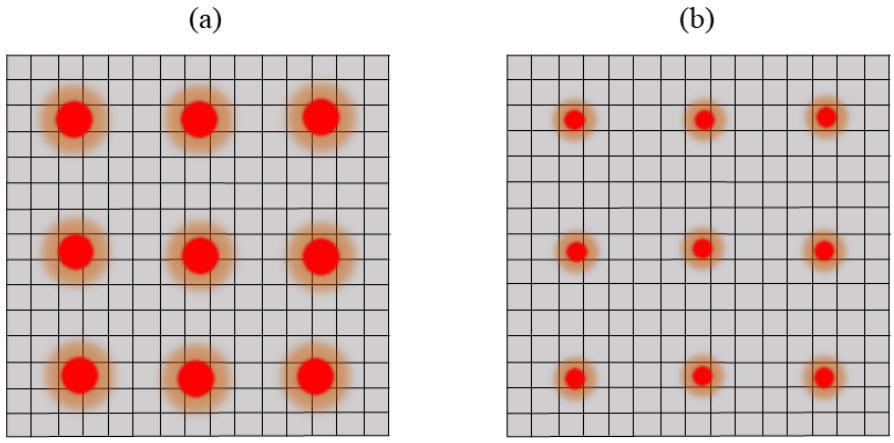

Figure 2.2: Pixel reassignment in ISM: (a) The focal spot for each scan position is mapped to the respective location of an image array with initial value 0, (b) The focal spot is scaled down to half before adding the same to the image array, and the process is repeated for all scan positions to get the final reconstructed image.

vital. As mentioned in Chapter 1, the most widely used OSRM techniques include point scanning-based stimulated emission depletion (STED) microscopy, and widefield based structured illumination microscopy (SIM) and single molecule localization microscopy (SMLM), such as STORM. SIM uses a spatially structured light

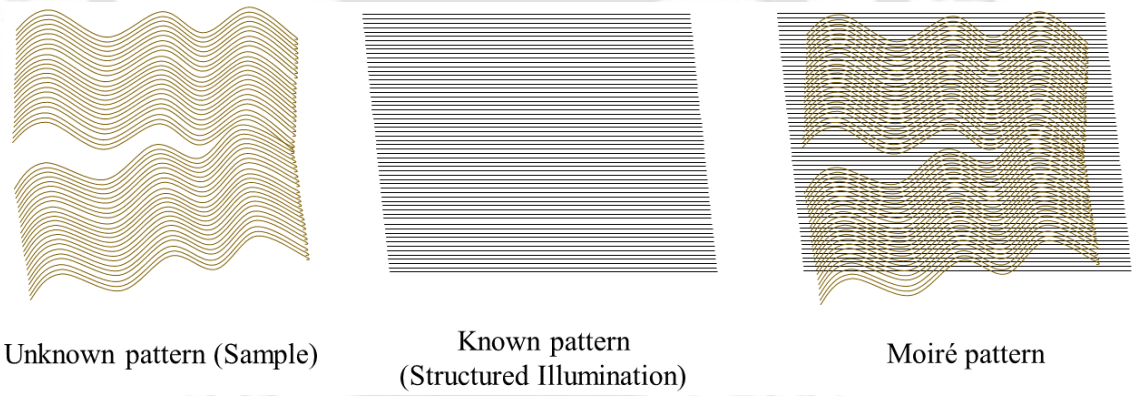

Figure 2.3: Principle of SIM: The Unknown pattern (i.e. Sample) is superimposed with a known illumination pattern (Structured Illumination) to get the Moiré fringes. Final image is constructed by extracting the high-frequency content from multiple Moiré fringes corresponding to different orientations of the illumination pattern.

(high-frequency mesh-like pattern) to illuminate the sample [7]. The high-frequency content of the sample, which is otherwise not available, gets superposed with the structured content or the pattern to produce Moiré pattern, as shown in Figure 2.3. The high-frequency information in the sample plane can then be extracted from multiple widefield images obtained by moving and rotating the structured pattern

in different directions. The extraction of high-resolution data involves the application of a suitable algorithm to the captured images. The idea of STED [8] is based

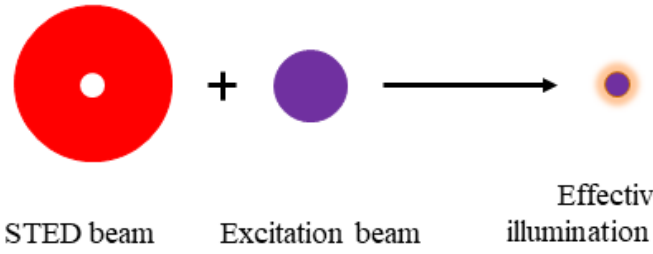

Figure 2.4: Going beyond the diffraction barrier using STED: a STED beam (doughnut-shaped intensity beam) and an Excitation beam, when aligned precisely, create a narrower Effective illumination spot by depleting the fluorescent markers outside the zero of the STED beam.

on stimulated emission and depletion of the molecules in the sample plane based on the confocal imaging technique. Here, the fluorescence emission of molecules surrounding the centre of the excitation spot in the sample plane is inhibited by depleting the excited states via stimulated emission. This requires the use of a suitably engineered laser beam, with a doughnut-shaped focal spot, called the STED beam, at a wavelength slightly higher than the excitation wavelength, in addition to the excitation beam. The excitation beam, which has a Gaussian intensity profile, excites all the molecules in the sample plane that lie within the area of the excitation spot. However, before the molecules undergo fluorescence emission, the STED beam arrives and depletes the excited molecules in the surrounding area of the centre. Thus, the confocal detector receives light coming from the molecules at the centre of the focal spot only, thereby drastically narrowing the effective PSF, as shown in Figure 2.4. Resolution of the STED microscope is given by,

$$r_{dough} \approx \lambda/2NA\sqrt{1 + (I_{sted}/I_{sat})} \tag{2.1}$$

where I_{sted} is the intensity of the STED beam and I_{sat} is the saturation intensity at which the probability of the fluorescence decreases by 50%. Maximizing the term I_{sted}/I_{sat} breaks the diffraction barrier and allows us to achieve resolution in the range 20-30 nm.

On the other hand, in STORM, fluorescent molecules in the sample plane of a widefield microscope are localized by switching them on and off stochastically (i.e., fluorescence blinking) using a suitable excitation source. The reconstructed image

can provide a lateral resolution comparable to that of STED. At present, STORM only works with fixed samples and necessitates more complex sample preparation than SIM and STED. However, instrumentation wise, STORM is much easier to implement compared to STED.

Below, we highlight the advantages of STORM over SIM and STED.

1. Conventional SIM provides around twofold increase in resolution compared to widefield microscopes, discerning structures at $\approx$ 100 nm and achieving lateral resolution close to $\lambda/4$NA. STED and STORM, on the other hand, can resolve structures as fine as $\approx$ 10 nm. However, they usually achieve resolutions between 20 and 50 nm for biological samples and suffer from limitations mostly due to the available laser power and the characteristics of the fluorophores.

2. SIM is more of a surface imaging technique rather than a three-dimensional or depth resolved imaging technique. STED and STORM, on the other hand, have numerous applications in surface and three-dimensional imaging.

3. STED necessitates a more intricate and costly setup, usually requiring well synchronized excitation and depletion pulses as well as a collinear alignment of beams. The two beams need to be derived from an ultrafast laser.

4. Among different techniques, directSTORM (dSTORM) [34], a variation of STORM, is more straightforward and economical than STED. Stochastic switching between emissive and dark states in fluorophores in an appropriate chemical environment is the basis of dSTORM, with a continuous wave laser excitation affecting the switching rates.

Overall, SMLM methods such as STORM provide resolution better than SIM and are less expensive and simpler to implement than the STED microscope. Consequently, we have chosen to implement STORM in this thesis.

2.4 Stochastic optical reconstruction microscopy

As discussed already, resolution refers to the smallest distance (d) at which two distinct features of the object can be well resolved in the image, as shown in Figure 2.5 (a). STORM doesn't directly surpass the diffraction limit by narrowing the imaging PSF but instead overcomes it by controlling the spatial distribution of fluorophore

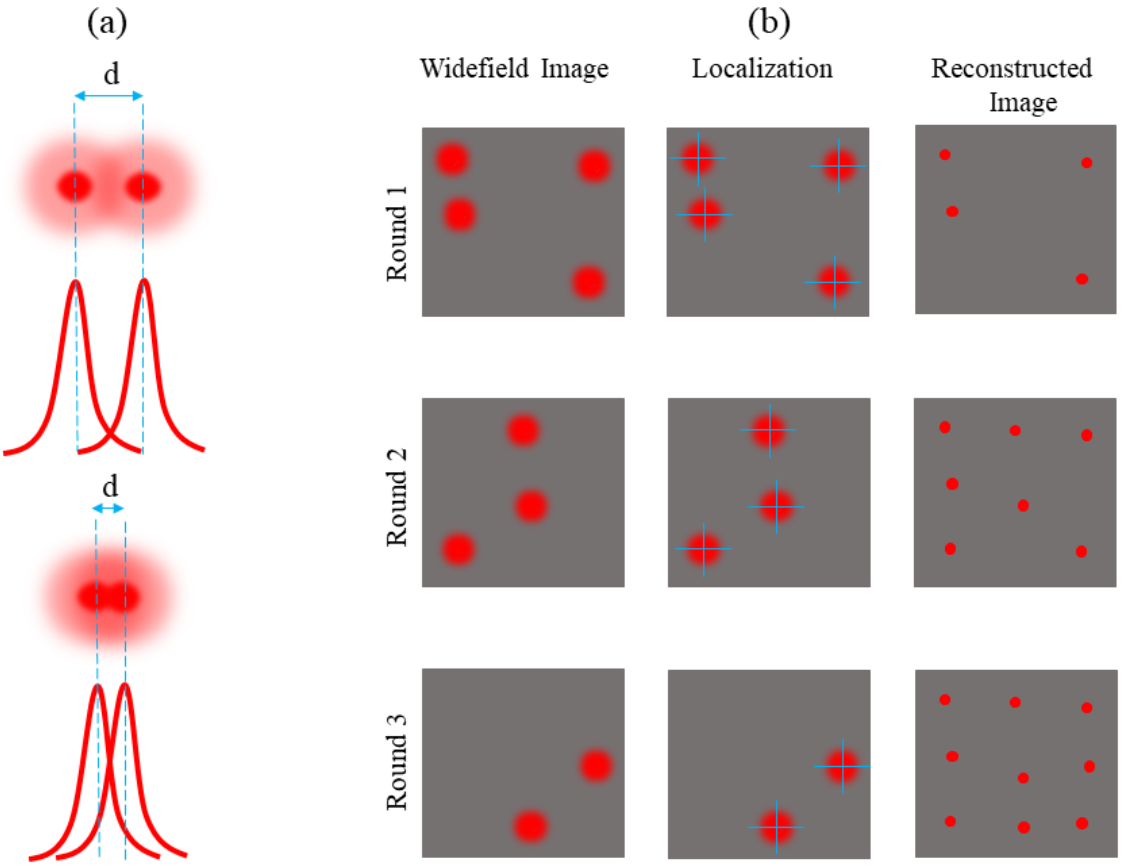

Figure 2.5: (a) Images of two point emitters with intensity line pot, at a distance d greater than the diffraction limit (seen in the upper row) and at a distance d smaller than the diffraction limit (seen in the lower row). (b) Non-overlapping PSFs are shown in widefield images (left), which are followed by the localization of each PSF (middle) and reconstructed super-resolved images (right). PSFs are localized and reconstructed in each round. Following the second and third rounds, the final super-resolved image is formed, which is displayed at the bottom (right corner).

emissions within the field of view (FOV) of a fluorescence microscope, ensuring that the PSFs captured by the camera are non-overlapping. The non-overlapping PSFs are then localized with a precision smaller than the diffraction limit by computationally identifying the center of each PSF, thereby enabling super-resolution through emitter localization. To ensure that emitting fluorophores are sparse enough not to overlap with one another, a scheme is employed to selectively "switch on" only a subset of the fluorophores tagged to specific molecules of the sample. Typically, this "switching" or "photoswitching" [35] occurs through stochastic interactions between the fluorophores and the excitation beam, which is elaborated below.

As shown in Figure 2.6, fluorophores can transition to long-lived triplet or dark

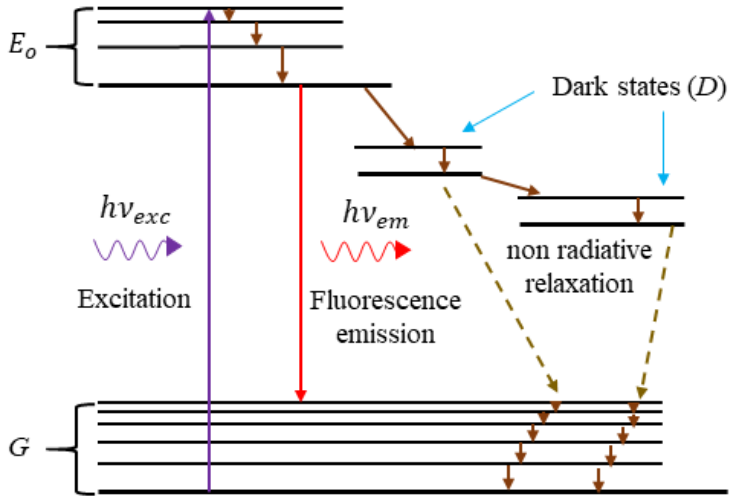

Figure 2.6: Energy level diagram of a molecule showing fluorescence emission, the molecule's transition to dark states (D) and the non-radiative relaxation from the dark state back to the ground state (G).

states (D) upon continuously being excited from the ground state (G) to the excited state (E_0). This is followed by the fluorescence emission and non-radiative transitions to the ground state. The fraction of fluorophores in state E_0 that emits fluorescence is limited by the chemical environment of the sample. This environment comprises certain chemical reagents to alter the fluorescence by producing the dark states through intersystem crossing. To make the fluorophores blink, they are first exposed to strong excitation light that pushes the majority of fluorophores labeling the sample into dark states that are inactive to fluorescence. The intensity is then reduced so that only a small portion of the fluorophores emit stochastically and return to the dark state. The stochastic emissions result in the typical "on and off" or "blinking" phenomenon [36] of the fluorophores, which must be a characteristic of the emitters during STORM imaging. The PSFs of the fluorescence emitters present in the targeted sites on the sample are then captured throughout several camera frames as they cycle between the fluorescent on and dark states under continuous excitation. As shown in Figure 2.7, thousands of image frames are needed to localize the fluorophores as the PSFs are fitted with 2D Gaussian functions to calculate the precise locations of the fluorophores with subpixel accuracy [37]. The resulting coordinates of the PSFs are then employed to reconstruct a super-resolved image of the sample.

Figure 2.5 (b) (column 1) shows three conventional widefield microscope images,

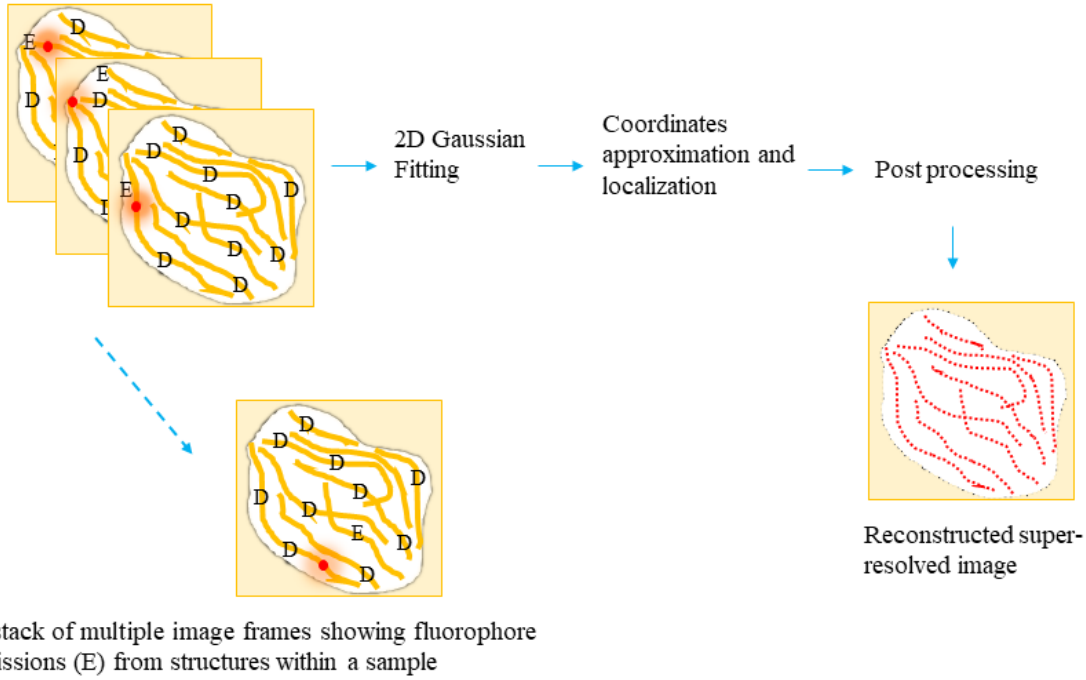

Figure 2.7: A schematic of the STORM reconstruction process: acquisition of thousands of image frames containing emitting fluorophores (E) from a sample, followed by PSF fitting, sub-pixel localization and approximation, post-processing and finally obtaining the reconstructed super-resolved image.

each featuring a few non-overlapping PSFs that can be localized and then mapped for reconstruction of a super-resolved image. Though only three rounds of localizations are shown here, producing a super-resolved image of an actual sample typically requires thousands of localization rounds, as already mentioned. The localization precision and, consequently, the resolution in the reconstructed image are influenced by the SNR of the acquired image data. The mathematical expression of localization precision in STORM [38] is given as,

$$d \approx \frac{\sigma}{\sqrt{N}} \tag{2.2}$$

where σ represents the standard deviation of the imaging system's spatial response function to a point source (i.e., the PSF) [27]. N is the number of photons collected during the blinking event of the molecule. Each emitter's position, ideally, can be recorded by a single fluorescence-switching cycle in STORM. However, numerous cycles of a single emitter are captured, and this may give rise to errors during localization if the sample drifts laterally over time throughout the switching cycles.

Hence, post processing is a must to rectify errors caused by lateral drift or any other artifacts.

2.4.1 Variants of STORM

In the initial STORM demonstrations [9, 39], fluorophores with an activator (A)-receptor (R) pairings that photo-switched between states with two distinct excitation wavelengths (λ_1 and λ_2, $\lambda_2 > \lambda_1$) enabled molecular photo-switching between fluorescence and dark states, as this pair was attached to each molecule (M) to be imaged. Under the condition that R is in proximity to A when A is illuminated with λ_1, R is sent to a dark state. Continuous excitation of R with λ_2 and activation with λ_1 keep the cycle on and off for R until it is photobleached permanently, as shown in Figure 2.8 (a). Many SMLM methods, however, simply call for labeling with a single fluorophore that can switch between dark and reversible fluorescent (F) active states on excitation with a single wavelength (λ), as shown in Figure 2.8 (b). This constitutes the dSTORM scheme[34, 40]. dSTORM was created to work with

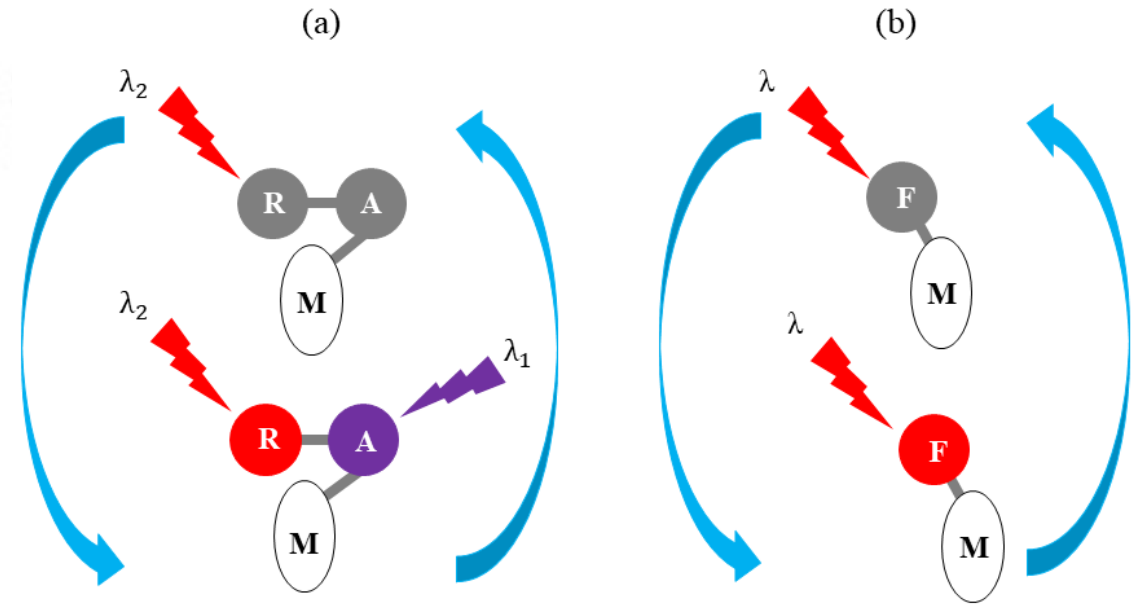

Figure 2.8: (a) Initial STORM scheme: Molecular photo-switching between fluorescence and dark states is made possible by fluorophores with activator (A)-receptor (R) pairings that photo-switch between states with two different excitation wavelengths (λ_1 and λ_2, $\lambda_2 > \lambda_1$), with the pair being attached to a molecule (M) in the sample. The cycle is maintained through constant excitation of R with λ_2 and activation with λ_1. (b) dSTORM: A single type of fluorophore (F) is attached to the molecule of interest (M), when excited with a single wavelength (λ), may transition between dark and reversible fluorescently active states.

common dye/fluorophores in the presence of specific chemical reagents to produce fluorescence active and dark states, as described earlier. A cost-effective implementation of dSTORM in a commercial microscope is referred to as easySTORM [20], which also employs simple sample preparation techniques. In this thesis, we have employed the easySTORM scheme.

2.5 Summary

The current Chapter has provided a brief historical insight into optical microscopy, followed by the resolution limit due to diffraction. The Chapter then discusses different optical microscopy techniques, such as confocal and array detection with image scanning microscopy, which can deliver resolution marginally breaking the diffraction barrier. This is followed by a brief introduction to some of the widely acknowledged optical super-resolution microscopy techniques like SIM, STED and STORM, that are able to deliver resolution around 100 nm and beyond. The Chapter concludes by outlining the motivation for choosing STORM in this work, along with its underlying principles and major variants.

* * *

Chapter 3

Implementation of an openFrame-based modular optical microscope

3.1 Introduction

Recent developments in light sources, detectors, and computational methods have significantly expanded the capabilities of optical microscopy, enabling advanced imaging for diverse applications [41, 42, 43, 44]. Yet, financial constraints prevent many organizations from acquiring commercial microscopes that incorporate the latest imaging modalities [14, 19], as already discussed in Chapter 1. While a large number of optical microscopes offer widefield epi-fluorescence imaging employing LED, halogen lamp, or laser sources for fluorescence excitation and scientific cameras for image capture, the majority of the optical microscopes come with trans-illumination mode for brightfield imaging. In addition, the commercial microscopes rely on proprietary hardware and software that make it difficult to upgrade the system for new or novel imaging applications. Nevertheless, by assembling off-the-shelf optical, mechanical, and electronic parts and adding open-source software, the potential of such commercial microscopes can, to a large extent, be realized at a reduced cost. For example, industry-grade diode lasers can be used in place of high-power solid-state lasers, and less expensive CMOS cameras can be used in place of scientific cameras such as EMCCD or sCMOS cameras. Additionally, expensive objective lenses can be replaced with low-cost ones with high numerical apertures. Finally, the image processing operations in the microscope can be executed with personal computers (PCs) typically designed for gaming applications. However, even with these substitutions, the body of the commercial microscope remains expensive, although one can build a complete microscope from standard optomechanical parts or

self-fabricated components, which usually requires technical skills that most users do not possess. In this Chapter, we utilize a modular microscope stand, named "openFrame" [19], to realize an affordable, research-grade optical microscope, based on the open-source microscopy concept, as mentioned in Chapter 1. Here, we demonstrate the overall configuration and working of this modular, self-assembled open microscope. We then consider applications of our microscope in research as well as clinical pathology and illustrate the performances in both trans-illumination and epi-fluorescence modes.

3.2 Experimental Arrangement

3.2.1 Key components and modules of the openFrame-based microscope

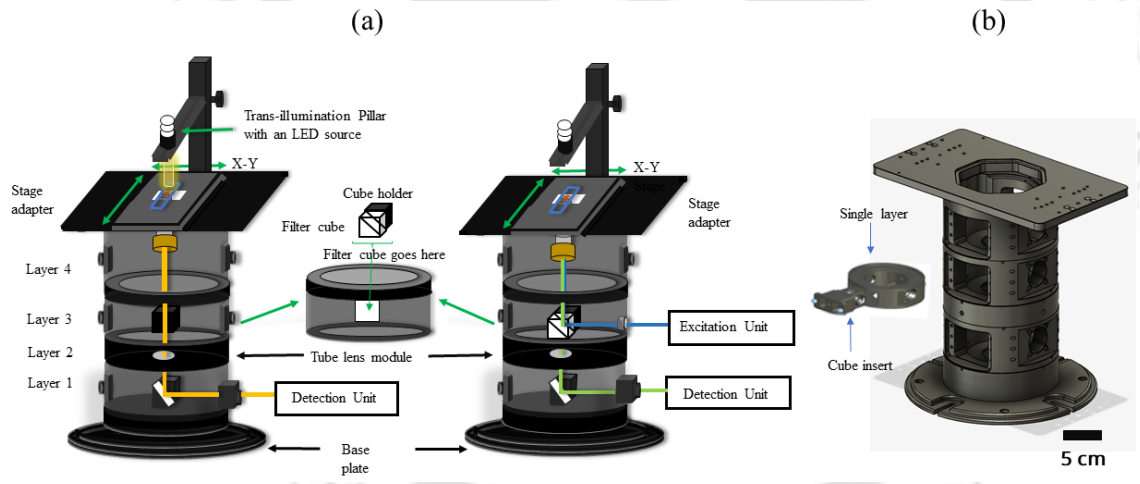

Figure 3.1: (a) Schematic of the openFrame-based modular microscope with its base plate, four layers, X-Y stage, trans-illumination pillar, excitation-detection units, and other hardware components. (b) A CAD rendering of the microscope stand with a single layer cube insert.

We first discuss the experimental arrangement and the implementation of the proposed modular microscope. The basic openFrame-based microscope, with a frame of anodized aluminum, comprises a base plate, a sample stage adapter, a trans-illumination pillar with an LED light source, and four modular layers, as shown in Figure 3.1 (a). The CAD illustration of the modular frame is shown in Figure 3.1 (b). The CAD files for the modules of the openFrame-based microscope

are freely accessible [19] and, therefore, the modules can either be purchased or fabricated in the mechanical workshops. Although the layers or modules in the frame are firmly fastened together, their orientation can be changed in 45° increments around the optical axis. Layer 1 of the modular microscope is used for detection, which features a 45° slanted mirror that reflects light coming from the sample onto a detection unit (camera) mounted at the side, located in the same layer. Layer 2 of the microscope has a tube lens, which is used to focus the light coming from the sample towards the camera. Layer 3 of the microscope has a filter cube. The filter cube reflects the excitation light towards the sample, allowing epi-fluorescence mode of imaging. Layer 4 of the microscope houses a piezoelectric stage into which an objective lens is fitted. The piezo stage controls the axial (Z) movement of the objective lens. On top of the Layer 4, a sample stage adapter is mounted. This sample stage adapter contains a motorized X-Y stage to move the sample in the lateral direction. Further, a trans-illumination pillar with an LED source is fastened to the edge of the stage adapter, which can be used for different illumination purposes. In our work, we use the combination of the trans-illumination pillar and the LED source for brightfield imaging. Overall, the microscope can function in both trans-illumination and epi-fluorescence modes. The basic applications of the microscope in the trans-illumination and fluorescence modes are discussed in the Results Section of this Chapter. Finally, to control the illumination, sample stage movement, objective lens movement, and detection of the microscope, the open-source software μManager [45] is utilized.

The upcoming Sections describe the individual building blocks of the openFrame-based modular microscope and their respective roles.

Brightfield imaging with trans-illumination

To enable brightfield imaging in the modular microscope, it has a dedicated trans-illumination pillar with an LED. Figure 3.1 (a) shows the trans-illumination pillar of the microscope. The pillar is an inverted L-shaped structure with a horizontal arm attached to the X-Y stage adapter. The arm consists of a combination of a condenser lens with an NA of 0.34 and an LED source (MONOLED, Cairn Research Ltd, UK). The combination of this condenser lens and the LED source produces an illumination spot on the sample plane of the microscope. The illumination spot on the sample can be adjusted by vertically shifting the horizontal arm on the pillar. During trans-

illumination mode of imaging, the light from the sample passes through layers 4 to 2 and is finally reflected by the 45° mirror in Layer 1 towards the detection unit. The detection unit or a camera is placed at the side port of Layer 1, facing the 45° mirror, as shown in Figure 3.1 (a).

X-Y stage for lateral movement of the sample

To enable precise lateral movement of the sample during imaging, we use the X–Y (sample) stage installed on a stage-adapter layer, fastened to Layer 4 of the modular microscope. The X-Y stage is motorized (ASR100B120B-E03T3A, Zaber, Canada). It also consists of a sample holder designed to accommodate samples prepared on slides of different dimensions, as well as various types of well plates for imaging. The X-Y stage is controlled via a PC, through hardware-software interaction (X-MCB2-KX14BG controller, Zaber Console software) (see Appendix A for the console software). Additionally, a joystick (X-JOY3-PTB2, Zaber) can be used to control the stage. The sample stage can be operated using the console software, the joystick, or the μManager software interface.

The objective lens

To focus the excitation beam onto the sample stage of the modular microscope, we use an objective lens. The objective lens is positioned on an L-bracket, which is parallel to the vertical optical axis of the microscope and is housed in Layer 4. The L-bracket is attached to a linear precision piezoelectric stage (Q-545.140, Physik Instrumente) equipped with an encoder delivering 1 nm resolution to facilitate precise movement of the objective. Before performing experiments, the piezo stage is programmed/referenced with the help of the stage controller (E-873 PI Shift Controller, Physik Instrumente) using the PI MikroMove software (see Appendix A for the software). Once the referencing is performed, the stage is ready to be controlled by the μManager. Initially, we use four objective lenses: PlanF 100× oil immersion 1.30 NA (AmScope), PlanF 40× 0.75 NA (AmScope), UPlanSApo 100x oil immersion 1.40 NA (Olympus), and PLN 20× 0.40 NA (Olympus) to illustrate the preliminary findings with our microscope. Further, the L-bracket is designed to allow for straightforward adaptation to a wide range of commercially available objective lenses. Additionally, the Layer 4 of the microscope can also house a dichroic beam splitter to provide an infrared laser beam for an optional autofocus module

[46].

Fluorescence excitation

To allow the microscope to perform fluorescence excitation of the sample, a dedicated fluorescence excitation module is required. In the modular microscope, the fluorescence excitation is introduced through Layer 3, which houses filter cubes and two side ports for mounting optical equipment that introduces excitation light for epi-fluorescence imaging. Two filter cubes, each comprising a dichroic beam splitter oriented toward their respective side ports, can be held in place by a mechanical slider. This arrangement allows two different types of excitations simultaneously. The dichroic beam splitter reflects the excitation light coming in from the side port up through the objective lens to the sample while letting the fluorescence emission of the sample go downward to Layer 1 and towards the camera. Here we use a customized multiline dichroic beam splitter (DBS) (ZT405/462/635/830rpc-UF2, [339553], Chroma Technology) of size 25.5 mm × 36 mm. Each cube also includes an excitation filter and an emission filter. In our implementation, we use an emission filter (ZET405/462/635/830m, [339636], Chroma Technology) and an excitation filter (ZET405/465/625/825x,[339819], Chroma Technology). During brightfield imaging, one position of the mechanical slider is kept vacant to enable the transmitted light to reach the camera directly. As an alternative, we can employ a single filter cube as shown in Figures 3.1 (a) and (b), which needs to be taken off during brightfield trans-illuminated imaging. However, throughout the thesis work, we have used the single filter cube only. The particular combination of the beam splitter and the filters used in our implementation is optimized for single or multiwavelength excitation at 405, 462, and 635 nm and transmission of emitted light within the bands 408–457, 472–627, and 645–820 nm. Further, the DBS can also be used with an optical autofocus system because it reflects wavelengths longer than 820 nm [46]. A plot of the transmission probability against the wavelength for the beam splitter and filters is available for reference in Appendix C. Alternatively, single bandpass filters can be employed in the filter cube, depending on the requirement of user.

Laser Bank

For fluorescence excitation of the sample, we need a laser source. Although a single wavelength laser is sufficient for excitation, multiwavelength laser sources are nec-

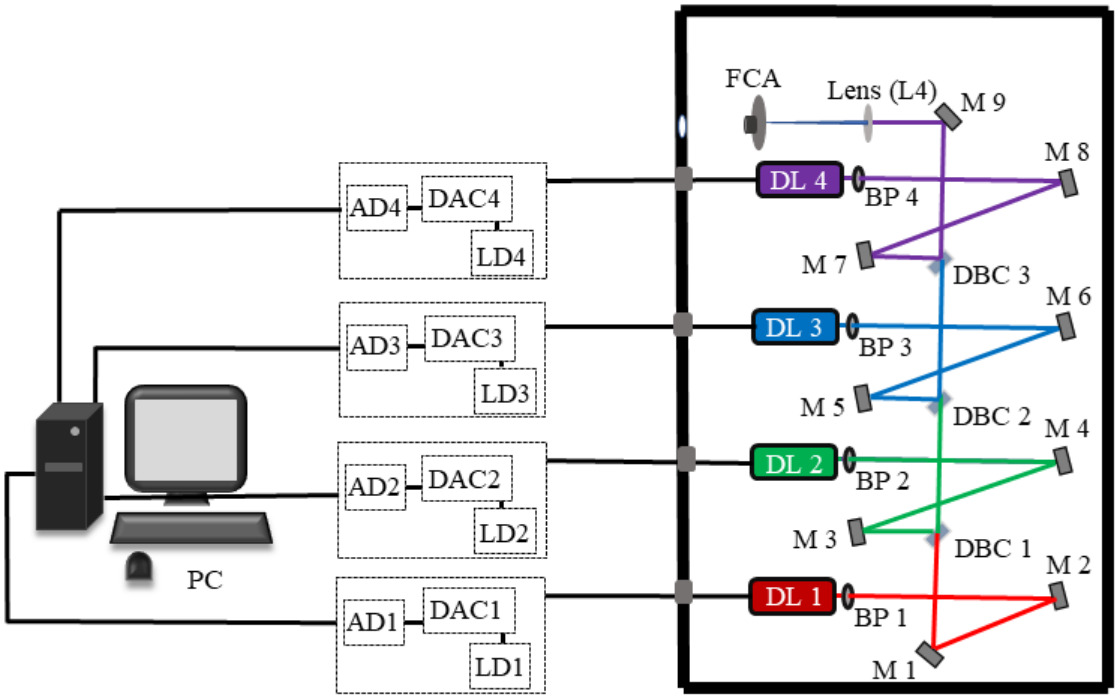

Figure 3.2: Schematic of the PC-controlled laser bank, incorporating lasers, optics, and electrical components as integral parts of the excitation unit.

essary to selectively excite different fluorophores with distinct absorption spectra, enabling multi-color imaging. To facilitate multiwavelength excitation, in our modular microscope, we assembled a computer-controlled laser bank, which contains four multimode diode lasers whose outputs can be optically combined to produce the excitation beam for fluorescence microscopy, as shown in Figure 3.2. The multimode diode laser modules used are, LDM-638-700-C, LDM-520-1000-C, LDM-462-1400-C and LDM-405-350-C (Make Lasertack GmbH), designated as DL1–DL4 in Figure 3.2. These diode modules generate continuous wave laser light at wavelengths of 638, 520, 462, and 405 nm, with maximum outputs of $\approx$ 700, $\approx$ 1000, $\approx$ 1400, and $\approx$ 350 mW, respectively. We place four bandpass (BP) filters (#65106, #65093, #39308, and #65072; Edmund Optics) in front of the outputs of the diode laser modules to achieve an excitation bandwidth (full width at half maximum) of 10 nm each. These filters are depicted as BP1–BP4 in Figure 3.2. They block the amplified spontaneous emission and ensure narrow-band excitation, e.g., for use with our multiline dichroic beam splitter and emission filter. Three dichroic beam combiners, DBC1, DBC2, and DBC3 (#86394, #86324, and #86389, Edmund Optics), as well as nine broadband dielectric mirrors, M1–M9 (BB05-E02, Thorlabs), all positioned

in kinematic mounts, combine the laser radiation from the four diode lasers. This arrangement makes the laser beams collinear to be incident at lens L4, which focuses the same into the Fibre Coupler Adapter (FCA) of a multimode optical fibre, ensuring delivery of the excitation light into the microscope. Additional excitation lasers can be incorporated into the laser bank, provided suitable combinations of dichroic beam combiners and filters are available in the excitation path to direct the corresponding excitation wavelengths towards the sample.

Laser power control

To control the excitation power/intensity of the four diode lasers on the sample plane of the modular microscope we design electrical circuits using four programmable Arduino microcontrollers (AD1–AD4), each equipped with a digital-to-analog converter (DAC1-DAC4), (DAC; TLV5618AI, Texas Instruments) and connected to the respective diode laser drivers (LD1–LD4; 2.5 A iLD driver, Lasertrack GmbH), as shown in Figure 3.2. With the above arrangement, the user can have linear control on laser power via the μManager software installed in the PC. The Arduino is to be configured to work with the μManager using the below steps,

1. Arduino Software IDE (see Appendix A for the software) is installed on the PC.
2. Arduino is connected to the PC with a USB 2.0 to serial adapter.
3. The Firmware source code is available here: https://micro-manager.org/Arduino. It is pasted into a blank sketch window of the Software IDE and uploaded to the Arduino microcontroller through this software.

The detailed procedure to add an Arduino in μManager is provided in Appendix B.

After configuring the Arduino, the appropriate electrical connections are made by assembling the Arduino, DAC, and the laser driver as shown in Figure 3.3. To assemble the DAC, a few additional components are required, such as a 100 nano-Farad (nF) ceramic capacitor and resistors for creating a voltage divider to power the DAC's reference point (6). Setting the reference voltage of the DAC to 2.04 Volt (V) between the terminals 5 and 6 is necessary (https://micro-manager.org/Arduino). To achieve this, we place a 20 k Ohm resistor (R1) between 5 and 6 and a 29 k Ohm resistor (R2) between 6 and 8. The analog outputs from the DAC are available at

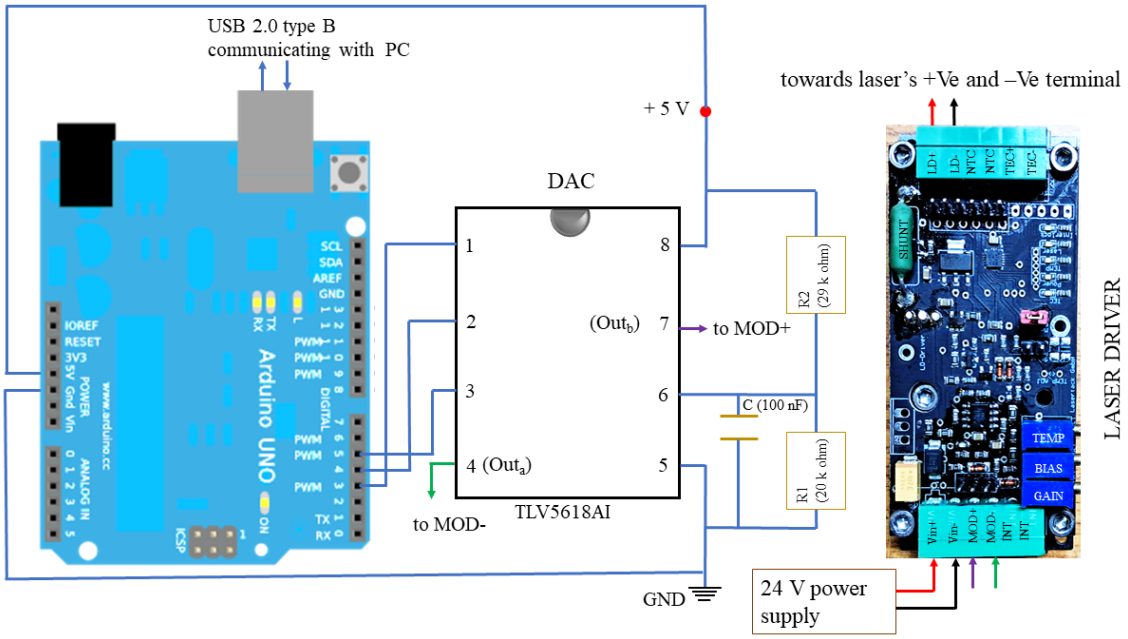

Figure 3.3: A schematic showing various components and electrical connections among an Arduino microcontroller, digital-to-analog converter (DAC), and a laser driver, necessary for laser voltage modulation.

terminals 4 (OUT_a) and 7 (OUT_b), which connect to the laser driver's MOD- and MOD+ leads, respectively. Further, the terminals at 8 and 5 (GND) of the DAC are connected to the Arduino's 5V and GND terminals. Temperature control is also included in each driver using an interlock mechanism (INT) and a thermoelectric cooler (TEC) driver. Further, the negative temperature coefficient (NTC) terminal on the laser driver connects to an NTC thermistor (NTCAFLEX05103HH, Vishay Beyschlag) on the laser diode.

After completing the necessary connections, the working temperature of the laser diode is set. This working temperature is normally the temperature of the laboratory or the environment in which the experiment is conducted. To set the working temperature of the diode laser, the power supply is disconnected, and then the resistance between the points TEMP ADJ in the laser driver is checked with a multimeter. Different resistance values correspond to different temperatures, which is easily known from the laser specifications. By adjusting the TEMP potentiometer screw in the laser driver, the resistance across the TEMP ADJ can be adjusted to the working temperature of the laser. Once the appropriate temperature is set, the power supply is connected again to the laser driver. Now, the laser diode is ready to be modulated between 0 and +5 volts, corresponding to the minimum and

the maximum laser powers. The laser voltage modulation using the laser driver potentiometers (BIAS and GAIN) is indicated below,

1. The potentiometers BIAS and GAIN are set by turning their screws counter-clockwise to zero ($\approx$ 25 turns, as given in the specifications).
2. The outputs from LD+ and LD- on the laser driver are connected to the Input terminals, Vin+ and Vin-, respectively, of the laser diode.
3. The supply voltage of the driver is set to 24 V DC.
4. The modulation source (outputs from terminals 7 and 4 in DAC) is connected to the input terminals, MOD+ and MOD-, of the laser driver.
5. Before the main supply voltage is turned on, it is ensured that the INT is closed by shorting the terminals.
6. The modulation voltage is set between 0.2 and 0.3 V DC using μManager.
7. The BIAS potentiometer is adjusted by turning its screw clockwise until the threshold voltage or current of the laser diode (as given in the laser specifications) is reached, and it starts to lase. The voltages can be measured across the shunt resistor (SHUNT) using a multimeter.
8. The modulation voltage is then set to 5 V DC on the μManager.
9. The maximum working voltage is then adjusted by turning the screw of the GAIN potentiometer clockwise until it is reached.
10. The modulation voltage is set again between 0.2 and 0.3 V DC, and the threshold voltage is checked across the SHUNT. If it has changed, the screw of the BIAS is turned counterclockwise to the value set in step 7.
11. The modulation voltage is set again to 5 V DC, and the maximum working voltage is checked. If it has changed, the screw of the GAIN is turned clockwise to the value set in step 9.

For proper functioning of the laser diode, it is always necessary to maintain the laser diode current between the threshold limit and the maximum permitted value. Hence, it is necessary to check the laser driver voltage across the SHUNT once in a

while, by performing the steps from 7-11. Further, in order to calculate the diode current, we convert the voltage measured across the SHUNT while the laser diode is connected. The ratio between the measured voltage (V) and current (Ampere (Amp)) varies by laser model or version, as given below:

1. 1.0 V/Amp or 1:1 for the 0.01-0.5 Amp version
2. 0.2 V/Amp or 1:5 for the 0.07-2.50 Amp version
3. 0.1 V/Amp or 1:10 for the 0.14-4.5 Amp version

For example, if the measured voltage across the SHUNT is 0.05 V, the current for different laser versions can be calculated using the appropriate ratio, as given below:

1. For the 0.01-0.5 Amp version: 0.05 V $\times$ 1 = 0.05 Amp
2. For the 0.07-2.5 Amp version: 0.05 V $\times$ 5 = 0.25 Amp
3. For the 0.14-4.5 Amp version: 0.05 V $\times$ 10 = 0.50 Amp

Tube lens layer

To focus the light from the sample collected by the objective lens onto the camera, we need a tube lens. In our modular microscope, Layer 2 contains the tube lens (#58-520, Nikon), whose focal length is 200 mm, although it can also accommodate a tube lens with various focal lengths.

Detection layer

In our modular microscope, the detection unit is located in Layer 1. It consists of a silver-coated right-angled mirror (#89-632, Edmund Optics) that reflects incoming light or emission to a camera, which is installed on the layer's side port. The detection layer of the microscope can house two of such mirrors via a mechanical slider, enabling the user to choose one of the two cameras positioned on opposite sides. In our work, we use two low-cost, fan-cooled CMOS cameras, one color CMOS camera (CellCam Rana 200CR, Cairn Research Ltd.) and a monochrome camera (CellCam Centro 200MR, Cairn Research Ltd.). Both cameras use the Sony IMX 183 CMOS sensor, which has a pixel resolution of 5440 $\times$ 3648 with each pixel of size

$\approx$ 2.4 μm. Although we show applications of the modular microscope using these two cameras only, the detection or the camera port of the microscope can easily accept different types of cameras.

Software control

To control all the components of the modular microscope, we use the μManager software (see Appendix A for the software). μManager is an open-source Java software program that can be controlled through a PC interface. μManager has a wide variety of device adapters that communicate with different hardware components and devices. In order to connect to the hardware, μManager, in addition to the device adapter, needs the respective Dynamic Link Library (DLL) file, which comes with the majority of the commercial hardware components and devices. In the absence of the DLL for a given hardware, a suitable DLL is to be generated to make the device adapter active. A list of various device adapters supported by the μManager can be found at https://micro-manager.org/Device_Support. Configuration of different hardware devices with the μManager can be found at https://micro-manager.org/Micro-Manager_Configuration_Guide. In our case, μManager is configured to control the four excitation lasers, to operate the piezoelectric stage driver and the X-Y stage, along with image capture by the two cameras. Although in our work we manually control the power of the LED source, the μManager offers device adapters for managing various LED sources too. The open-source software Fiji-ImageJ [47] (see Appendix A) is utilized for image analysis of the captured images. The μManager can also be used with the open-source program ImageJ [48], which provides additional functions.

3.2.2 List of the essential components for assembling the microscope

The essential components needed to assemble the openFrame-based modular microscope in an affordable manner are listed in Table 3.1. Although in this work, we are using the motorized X-Y stage or the joystick to control the lateral movement of the sample, one can replace them, with a manual X-Y stage, such as the Olympus CSS2001 (Thorlabs), whose price is $\approx$ 6 times less than the motorized stage and joystick combined. The tentative price of the majority of the components can be found here [19].

Components
1.30 NA oil immersion 100× objective
Despeckler and power supply trans-illumination pillar and LED source PI piezo stage with controller CellCam 200MR CellCam 200CR Zaber motorized X–Y stage with controller
openFrame modular stand
405 nm diode laser and driver 462 nm diode laser and driver 520 nm diode laser and driver 638 nm diode laser and driver
Arduinos, DACs, and other electronics for diode laser control, along with the metal enclosures for lasers Multimode fibre Copper plates as heat sinks Mirrors, DBC, DBS, and optical filters Mounts, posts, screws, and other components inside the laser bank

Table 3.1: List of the essential components in the openFrame-based modular microscope

3.2.3 Implementation of the Microscope

The schematic of the modular microscope in the epi-fluorescence mode is shown in Figure 3.4. The diagram illustrates how a multimode optical fibre (MMOF) (FG050UGA-CUSTOM, Thorlabs) cable carries light from the diode lasers inside the laser bank and delivers it to the excitation layer of the microscope via the optics in the excitation unit. Light emerging from the MMOF at the FCA is collimated and focused by the combination of lenses L1 and L2 via mirror M1, at the back focal plane (BFP) of the objective lens after reflection from the DBS cube inside the excitation layer. The light from the sample collected by the objective lens is transmitted through the DBS cube and focused by the Tube Lens L3 after being reflected from the Mirror M2 to form the image at the camera plane. To achieve uniform illumination on the sample plane, the MMOF is vibrated using a fibre vibrator or despeckler (DESPECKLER, Cairn Research Ltd.). The fibre vibrator mixes the spatial modes of the radiation and time-averages the speckle patterns that appear

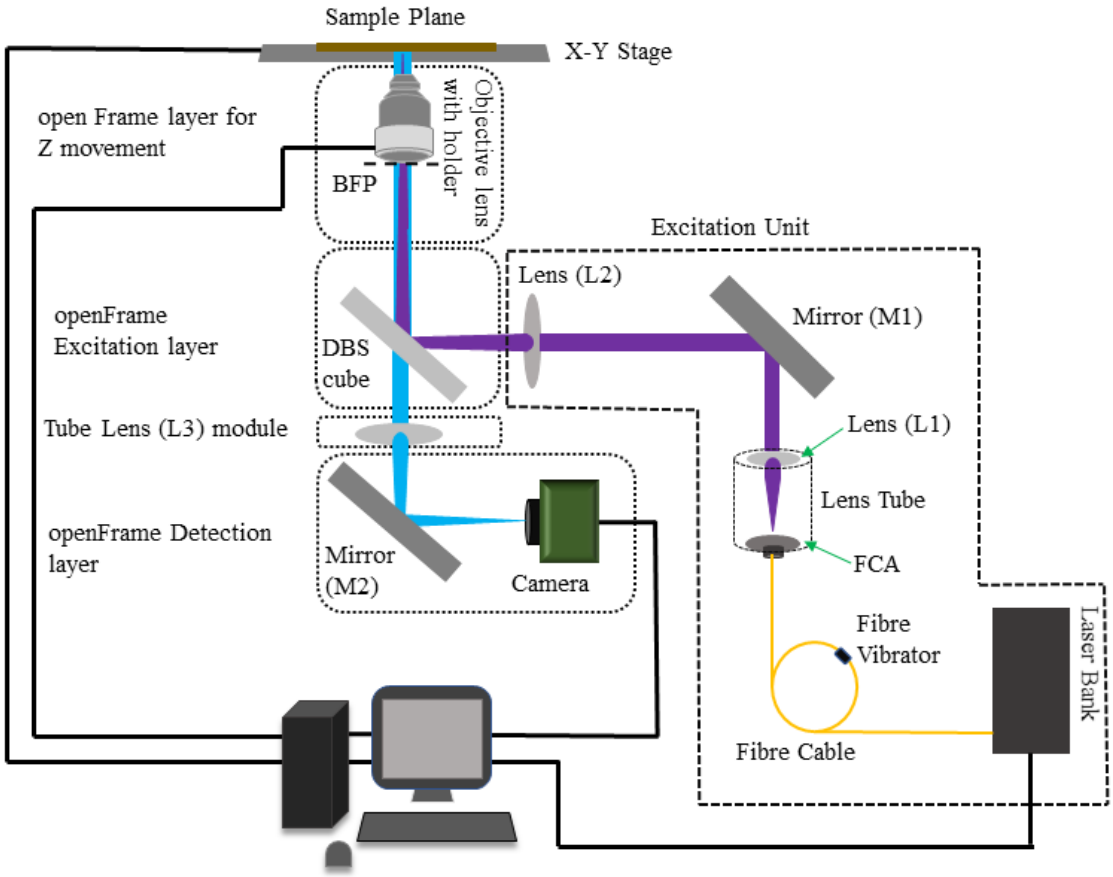

Figure 3.4: openFrame-based modular microscope implemented in the epi-fluorescence mode by assembling essential hardware, optical, optoelectronic and electronic components.

in the illuminated region of the sample. As shown in Figure 3.5 (b), when a fluorescent sample (92001 Autofluorescent Plastic Slides, Chroma Technology) on the X-Y stage is excited with the 462 nm laser beam, keeping the despeckler on, almost a smooth circular emission spot in the field of view (FOV) is observed. However, this is not the case when the despeckler is switched off, as shown in Figure 3.5 (a). Figure 3.5 (c) is a combined normalized intensity plot of the same regions marked as red and blue in Figures 3.5 (a) and (b). The excitation corresponding to this emission is accomplished over a FOV with a diameter of roughly 115 μm using the 100× objective lens, when imaged by the monochrome camera. For the 40× and 20× microscope objectives, a similar shape of the emission beam is observed in the FOV of the camera, but with diameters of $\approx$ 310 and 625 μm, respectively. The numerical aperture 0.22 of the MMOF with 50 μm core determines the illuminated area of the sample plane. With this arrangement, the back aperture of the objective can receive up to 90% of the laser power. The system produces beam spots of simi-

lar shape and dimensions on the fluorescent sample (92001 Autofluorescent Plastic Slides, Chroma Technology) in the sample plane, at the wavelengths 405 nm, 532 nm, and 638 nm.

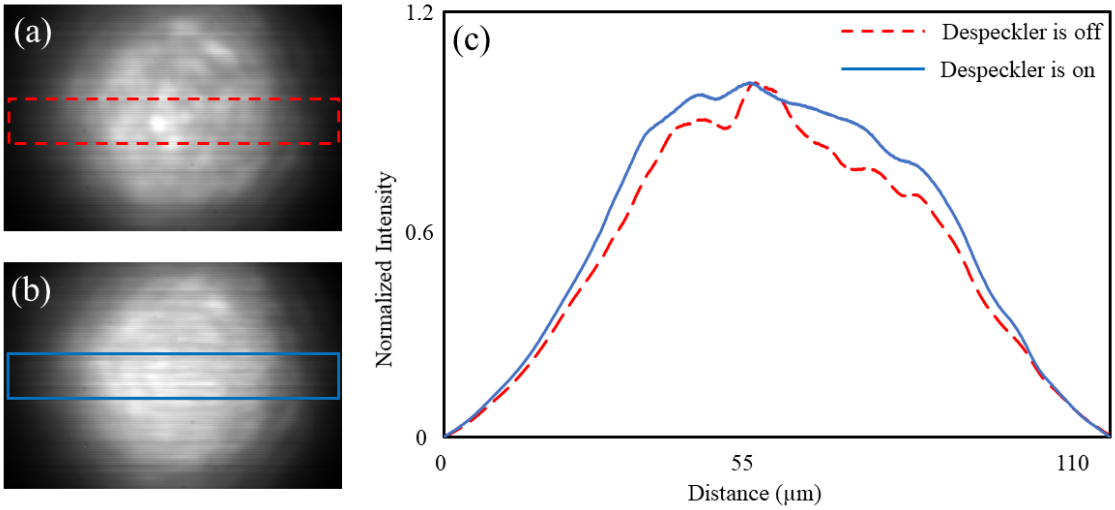

Figure 3.5: Emission spot from a fluorescence slide kept on the sample plane and excited with the 462 nm beam, as recorded in the monochrome camera when the despeckler is switched (a) off and (b) on. (c) is the combined normalized intensity plots through the regions shown in (a) and (b).

3.3 Results

3.3.1 Brightfield imaging utilizing transmitted light

To illustrate the brightfield imaging capability utilizing transmitted light in the modular microscope, we image a positive 1951 USAF test target (R3L3S1P, Thorlabs). For image acquisition, a monochrome camera and μManager are used, while Fiji is used to analyze the acquired images, as mentioned already. At first, an objective lens with 20× magnification is used to image the test target, and the captured image is seen in Figure 3.6 (a). This is followed by imaging of the same target with the oil immersion objective lens having 100× magnification, and the images are seen in Figures 3.6 (b) and (c). The target has several opaque/black strips or patterns on it, such as those for group 7, element 1 (G7E1) and element 6 (G7E6), indicated by yellow rectangles in Figures 3.6 (b) and (c), respectively. The full width at half maximum (FWHM) of the opaque and transparent strips within each region

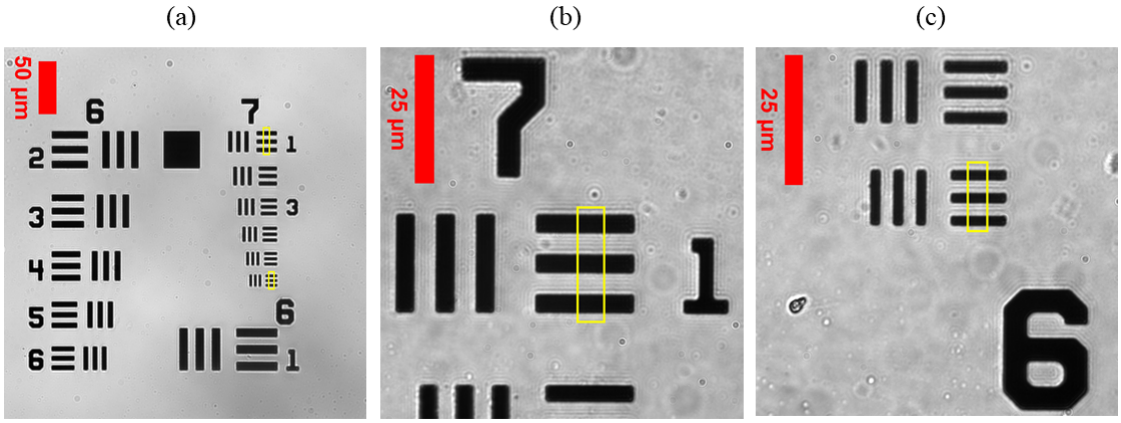

Figure 3.6: The trans-illumination images of (a) a portion of 1951 USAF test target using the 20× objective lens, (b) the element G7E1, and (c) the element G6E1, using the 100× objective lens, all using the monochrome camera. Yellow rectangles indicate the directions for line profiles used to measure the width of the respective black strips.

of interest (ROI) is estimated by plotting greyscale intensity profiles along a line perpendicular to the strips. The manufacturer specified widths are then compared with these measured values. The measured mean FWHM values closely match the specified values, as seen in Table 3.2, indicating that the camera and microscope system are configured correctly.

Pattern Number	**Width of a black strip according to the specs (μm)**	**Experimentally measured width of the black strip using two objective lenses (μm)**	
		20x 0.40 NA	**100x oil immersion 1.30 NA**
G7E1	3.91	3.99	3.92
G7E6	2.19	2.31	2.2

Table 3.2: Experimentally obtained widths of the black strips in the G7E1 and G7E6 patterns of the 1951 USAF resolution test chart utilizing various objective lenses in the trans-illumination mode.

3.3.2 Imaging in the epi-fluorescence mode with multiwavelength excitation

To perform imaging with multiwavelength excitation in the epi-fluorescence mode in our modular microscope, we image a mixture of crimson-red (F8806 FluoSpheres®

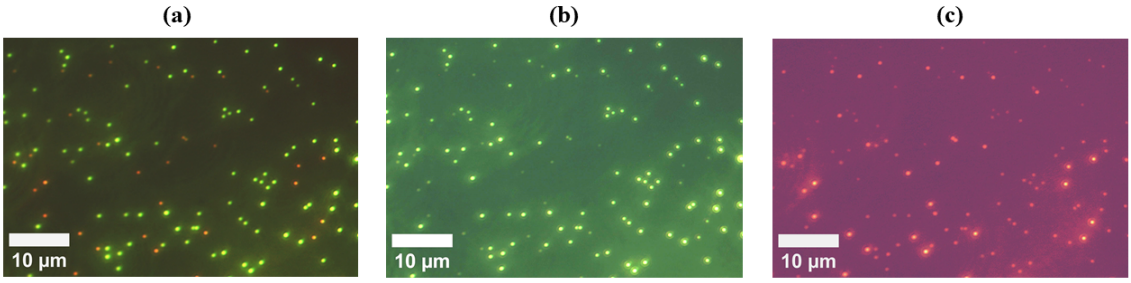

Figure 3.7: Epi-fluorescence images of a microscope sample slide containing a blend of crimson-red and orange-green fluorescent beads using the 100× objective lens on the color CMOS camera with (a) both the 462 nm and 638 nm lasers, (b) only the 462 nm laser, and (c) only the 638 nm laser.

carboxylate, Invitrogen™) and orange-green (F8809 FluoSpheres® carboxylate, Invitrogen™) fluorescence beads on the sample plane. To prepare the slides, both beads are first diluted separately in deionized water (at a ratio 1:2000 v/v), and then the dilutions are thoroughly mixed using a vortex mixer, followed by placing an $\approx 10\mu$L of the mixture between a cover glass and a microscope glass slide. The 638 nm and 462 nm lasers are used for exciting the crimson-red beads and the orange-green beads, respectively. At first, we capture an image of an area of the sample, as shown in Figure 3.7 (a), using the color CMOS camera and the 100× objective lens and the fluorescence filter cube in Layer 3. The sample is being excited simultaneously by the 638 nm and 462 nm diode lasers. The image shown in Figure 3.7 (b) is then captured using the 462 nm diode laser. Next, for the same region of the sample, we switch off the 462 nm laser and turn on the 638 nm diode laser to capture an image as displayed in Figure 3.7 (c). Figure 3.7 demonstrates the utilization of the multiwavelength excitation of the modular microscope in the epi-fluorescence mode.

3.3.3 Comparison of the openFrame with a standard commercial microscope in both epi-fluorescence and bright-field modes

To compare the performance of the openFrame-based microscope with a commercial microscope (IX51, Olympus), we image carboxyl quantum dot (Q21361MP, Invitrogen™, size $\approx$ 15-20 nm) and human glioblastoma cells (U87MG cells) in both microscopes. We first prepare quantum dot (QD) samples to compare the

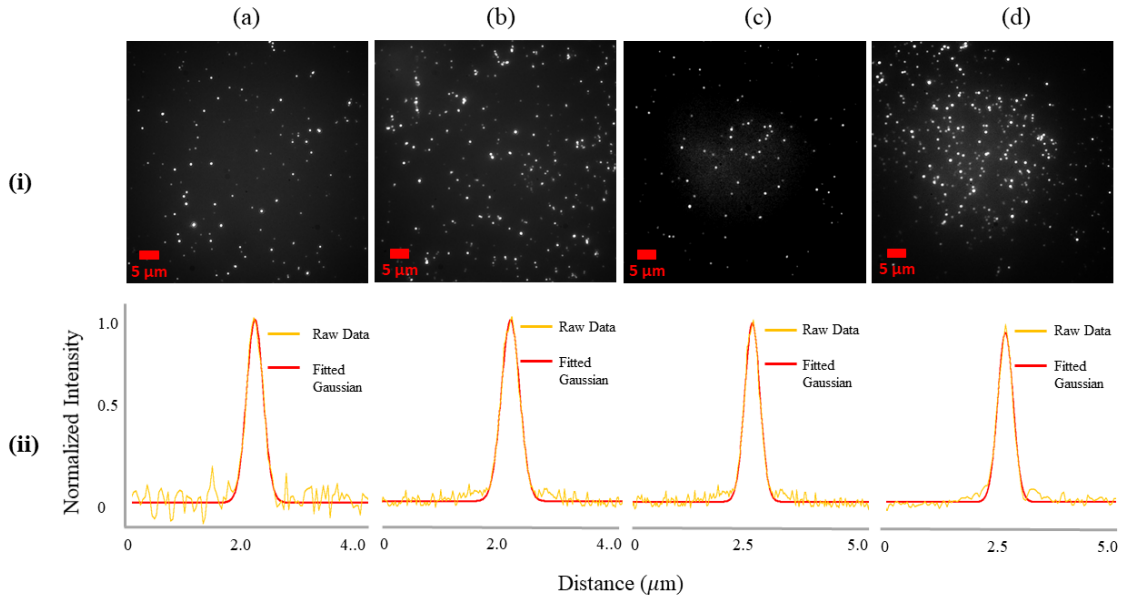

Figure 3.8: (i) Epi-fluorescence images of quantum dots (QDs) using a commercial Olympus IX51 fluorescence microscope with the (a) 100x 1.40 NA Olympus objective lens and (b) 100x 1.30 NA AmScope objective lens and using the openFrame-based modular microscope with the (c) 100x 1.40 NA Olympus objective lens and (d) 100x 1.30 NA AmScope objective lens, captured in the monochrome CMOS camera, with 462 nm excitation. (ii) (a-d) show the Gaussian fitted line plots in addition to the raw intensity plots for a randomly chosen isolated QD from images (i) (a-d).

performance of the modular microscope with the Olympus IX51 microscope in the epi-fluorescence mode. To prepare the QD samples, the stock solution of the QDs is diluted in deionized water (in a ratio 1:5000 v/v), followed by preparation of the sample slide by placing $\approx$ 10 μL of the dilution between a cover glass and a microscope slide. The 462 nm laser is used to excite the QDs in both microscopes, and fluorescence images are captured using the monochrome CMOS camera along with the same filter combination, as previously discussed. The QDs emit within a range of 650-850 nm wavelength as specified by the manufacturer. A measure of the lateral PSF of each microscope is given by the FWHM of the QD images since the QD diameters range from 15 to 20 nm, which is significantly smaller than the excitation or emission wavelengths [49]. First, we use the 1.40 NA objective lens on the Olympus IX51 microscope to image the QDs, and next, we use the 1.30 NA AmScope lens on the same microscope to view a separate region of the QD slide, as shown in Figures 3.8 (i) (a) and (b), respectively. Using the identical objective lenses on the openFrame-based microscope, we once again image the same QD sample, and are seen in Figures 3.8 (i) (c) and (d). The intensity versus position

across the center of isolated QDs selected from each of the images in Figures 3.8 (i) (a-d) are plotted. Figures 3.8 (ii) (a-d) show the raw and Gaussian-fitted intensity line plots for randomly isolated QDs. It is noted that the measured lateral FWHM from each plot provides the experimental width of the lateral PSF. The lateral FWHM of the diffraction limited PSF is determined according to the Abbe's limit as discussed in Chapter 2. Table 3.3 presents the mean lateral FWHM values determined experimentally for different isolated QDs chosen from each of the images, along with the theoretical estimates for the two objective lenses. The results show no discernible variation in the experimentally determined lateral PSF between the two microscopes. Theoretically, the lateral FWHM for the cheaper 1.30 NA AmScope objective lens should be 7.8% larger compared to 1.40 NA, yet the 1.30 NA AmScope lens only provided a resolution that was around 5% worse than the 1.40 NA Olympus lens. Table 3.3 demonstrates that the image quality produced by the openFrame-based modular microscope with the low-cost objective lens is similar to that of the commercial microscope. Additionally, when utilizing the Olympus 1.40 NA objective lens, the lateral FWHM values produced by both microscopes are comparable.

We then compare the performance of the openFrame-based modular microscope with the Olympus IX51 microscope while imaging microscope sample slides of unstained human glioblastoma (U87MG cells) in both microscopes, utilizing the brightfield and epi-fluorescence modes. We use the PlanF 40×, 0.75 NA objective lens (PF40X-INF, AmScope) in the openFrame-based microscope and a 40×, 0.60 NA objective lens (LUCPlanFLN, Olympus Optical) in the Olympus IX51 during imaging. Both microscopes use the same color CMOS camera and filter cube. However, for brightfield imaging, the filter cube is removed from both microscopes and is inserted back during the epi-fluorescence imaging. At first, brightfield images of two distinct regions on the sample are captured in the Olympus system and are displayed in Figures 3.9 (i) (a) and (c). Next, the same regions are imaged in the brightfield using the modular microscope and are displayed in Figures 3.9 (ii) (a) and (c). For the epi-fluorescence mode, we use the 462 nm laser. Figures 3.9 (i) (b) and (d) show the epi-fluorescence images captured with the Olympus microscope, while Figures 3.9 (ii) (b) and (d) are the acquired epi-fluorescence images of the same regions with the modular microscope. Under 462 nm laser excitation, the cells show light-yellowish autofluorescence in both microscopes. In both brightfield and epi-fluorescence imaging, the openFrame-based modular microscope produces sim-

Type of Quantum dot (QD)	Size of QD	FWHM of lateral PSF (theoretical) at $\lambda = 705$ nm using different NA 100x objective lenses		Mean FWHM of the lateral PSF measured with a CMOS camera (rendered at 21.6 nm in the sample plane)			
				Standard commercial microscope		openFrame-based microscope	
		1.40 NA	1.30 NA	1.40 NA 100× Olympus lens	1.30 NA 100× AmScope lens	1.40 NA 100× Olympus lens	1.30 NA 100× AmScope lens
Carboxyl QDs (emission peak at 705 nm)	15-20 nm	251 nm	271 nm	310±3 nm	321±2 nm	311±4 nm	324±3 nm

Table 3.3: Theoretical and experimental full width at half maximum (FWHM) of the lateral point spread function (PSF) for the standard optical microscope and the openFrame-based microscope, utilizing the same two objective lenses.

ilar quality images when compared to the Olympus IX51. It is observed that the epi-fluorescence mode images captured with the modular microscope appear fainter compared to the images of the same regions captured in the Olympus microscope. The reason behind this is the photobleaching of the fluorophores during the initial imaging with the Olympus microscope.

3.3.4 Application in histopathological examination

One of the primary objectives of the openFrame-based modular microscope is to facilitate its use in clinical examination and diagnostic applications. To demonstrate the clinical applications of the modular microscope, we image histopathology samples of human breast tissue slices stained with hematoxylin and eosin (H&E) to distinguish between normal and malignant regions. We at first compare the performance of the modular microscope with a commercial microscope (NIKON Eclipse

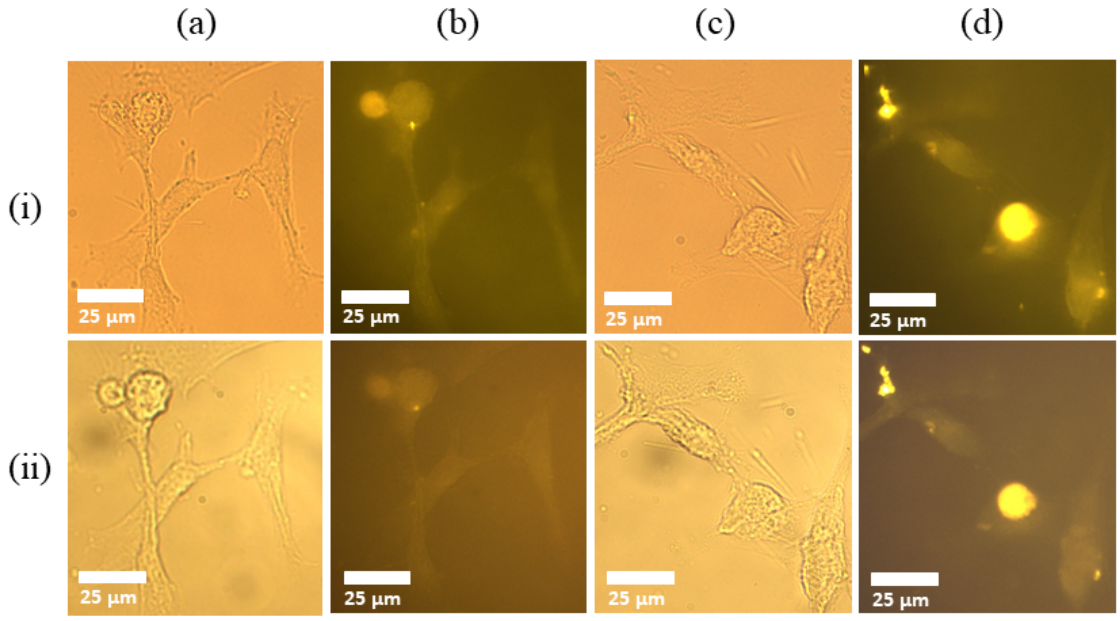

Figure 3.9: Brightfield images (i) (a,c) and fluorescence images (i) (b,d) of unstained human glioblastoma cells (U87MG) obtained from two areas on a sample slide using the Olympus IX51 microscope with a 40×, 0.60 NA objective lens (LUCPlanFLN, Olympus). The same areas are subsequently imaged in brightfield mode (ii) (a,c) and fluorescence mode (ii) (b,d) using the openFrame-based microscope with a low-cost 40× 0.75 NA objective lens (PF40X-INF, AmScope). The brightfield images are captured with the color CMOS camera, while the fluorescence images are obtained at 462 nm excitation using the same camera.

50i, 40× objective) in trans-illumination mode. Under the NIKON Eclipse 50i microscope, we image normal ducts from the human breast tissue as seen in Figure 3.10 (i) (a), while Figure 3.10 (i) (b) shows malignant ducts from a different slide imaged using the same microscope. We notice that the normal ducts in Figure 3.10 (i) (a) have elliptical rings of epithelial cells. While seen in Figure 3.10 (i) (b), the malignant ducts have invaded the neighboring ducts, resulting in deformed epithelial rings. The identical H&E-stained tissue slices are then imaged using a color CMOS camera (without the filter cube) of the modular microscope in the trans-illumination mode with the 20× objective lens (Olympus PLN 20X, 0.40 NA). Figure 3.10 (ii) (a) depicts a normal duct (circled) with a regular elliptical ring of epithelial cells and Figure 3.10 (ii) (b) depicts a malignant duct (circled) packed with tumor cells and devoid of the typical elliptical arrangement of the epithelial cells. Figures 3.10 (iii) (a) and (b), on the other hand, display the epi-fluorescence images corresponding to Figures 3.10 (ii) (a) and (b), respectively. These epi-fluorescence images are obtained using the 462 nm laser excitation. There is a noticeable contrast between

the duct boundary and the surrounding areas as the labeled cells in the cytoplasmic region and inside the ducts glow green, while the lumen does not. To be noted, hematoxylin exhibits considerable absorbance in the UV-Visible range with very little fluorescence, whereas eosin dye is known for its green emission [50, 51]. The irregular dark boundary in the epi-fluorescence image in Figure 3.10 (iii) (b) indicates the location of the cancerous duct.

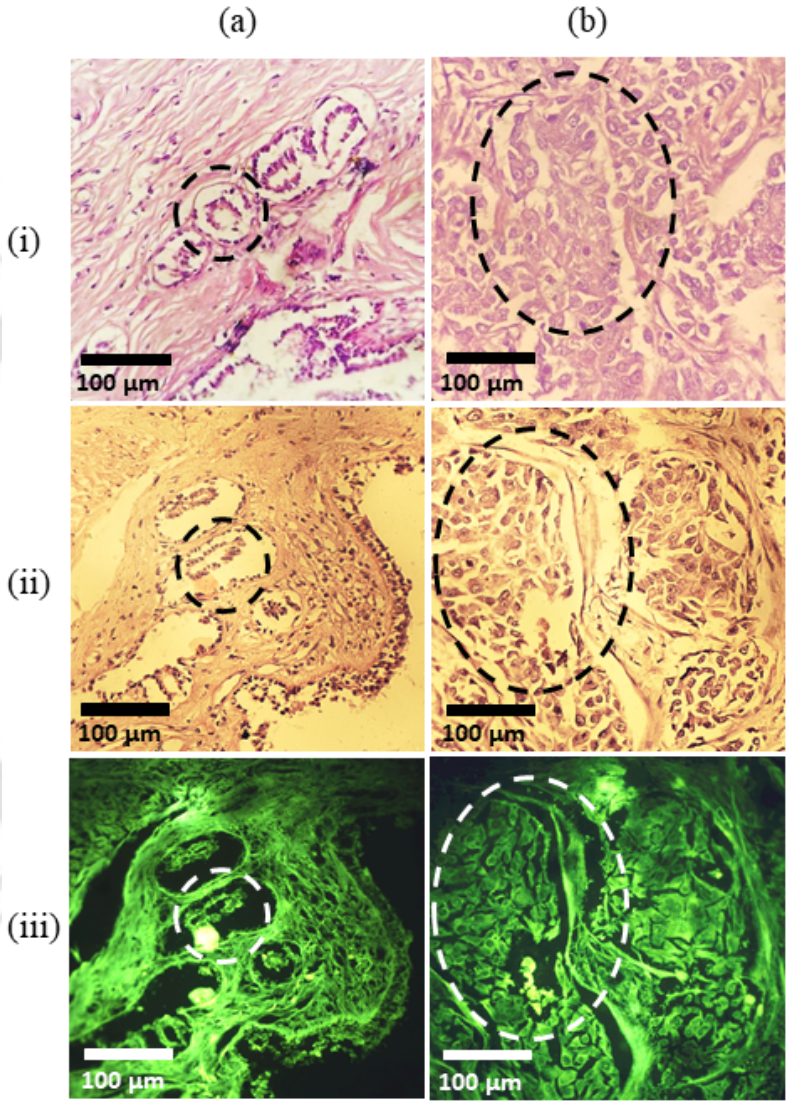

Figure 3.10: H&E-stained human breast tissue sections in (i) (a) normal and (i) (b) malignant, imaged in the brightfield trans-illumination mode using a Nikon Eclipse 50i microscope with a 40× objective lens and the CellCam Rana 200CR color CMOS camera. Brightfield images of (ii) (a) normal and (ii) (b) malignant breast tissue stained with H&E, (iii) (a) and (b) epi-fluorescence images with 462 nm excitation laser, of (ii) (a) and (b), respectively, using the openFrame-based modular microscope with a 20× objective lens.

3.4 Summary

We have presented the implementation of the affordable, modular, research-grade microscope developed based on the open-source microscopy concept. The modular microscope is built by assembling industry-grade optical, mechanical, and electronic parts. The affordability and modularity of the components, together with the usage of open-source software for hardware control and image analysis, make the system maintenance easier. This openFrame-based microscope is shown to function in both trans-illumination and epi-fluorescence modes. Our findings demonstrate the research-grade imaging capabilities of the basic widefield microscope as well as its potential for cancer research and clinical histopathology investigation, specifically when imaging human glioblastoma cells and sections of human breast tissue.

* * *

Chapter 4

Implementation of Stochastic Optical Reconstruction Microscopy (STORM)

4.1 Introduction

As discussed already, achieving spatial resolution below 200 nm in conventional optical microscopy is not possible due to diffraction. In recent times, advanced microscopy techniques have evolved to overcome this limitation, achieving super-resolution using visible light, known collectively as optical super-resolution microscopy (OSRM) techniques. OSRM has opened up new avenues for understanding biological and physical systems at a resolution $\leq$ 20 nm. Especially in cancer research, OSRM has made significant contributions [10, 11, 12, 44], which is otherwise not possible with conventional optical microscopes. Although indirect detection techniques [52, 53] for cancers are also available, these techniques cannot show structural alterations essential for early cancer detection, which is, however, only possible with OSRM. Despite these advantages, the widespread adoption of OSRM remains limited, particularly in the majority of hospitals, clinics, laboratories, and research institutes, especially in regions like Asia and the Indian subcontinent, where cancer related diseases are increasing at an alarming rate. A major barrier to the widespread adoption of OSRM is the high cost [54, 55]. However, as outlined in the Chapters 1 and 2, OSRM utilizing the stochastic optical reconstruction microscopy (STORM) technique can be implemented easily with minimal changes to a conventional widefield microscope, and by following the open-source approach, it can be made more affordable compared to the other available OSRM techniques. In addition to affordability, it is also important to consider the feasibility of the technique in hot and humid climates, typical of the Asian and the Indian subcontinent. Such

climatic conditions pose significant challenges to both sample preparation, preservation, and system performance, including the stability of optical and electronic components. Therefore, it is essential to evaluate how a low-cost STORM system performs under these challenges. In this chapter, we discuss the implementation of easySTORM in the openFrame-based modular optical microscope. The chapter comprises discussions on the image acquisition process, reconstruction process using the open-source ThunderSTORM plugin [56], image analysis in Fiji, and sample preparation techniques optimized for STORM. In addition, we discuss the challenges faced during the initial implementation of STORM and the resolution to overcome them. Finally, the performance of the openFrame-based easySTORM system is demonstrated by imaging quantum dots and then analyzing human cytoskeletal structures with single-color and multi-color excitations.

4.2 Materials and methods

4.2.1 Experimental arrangement

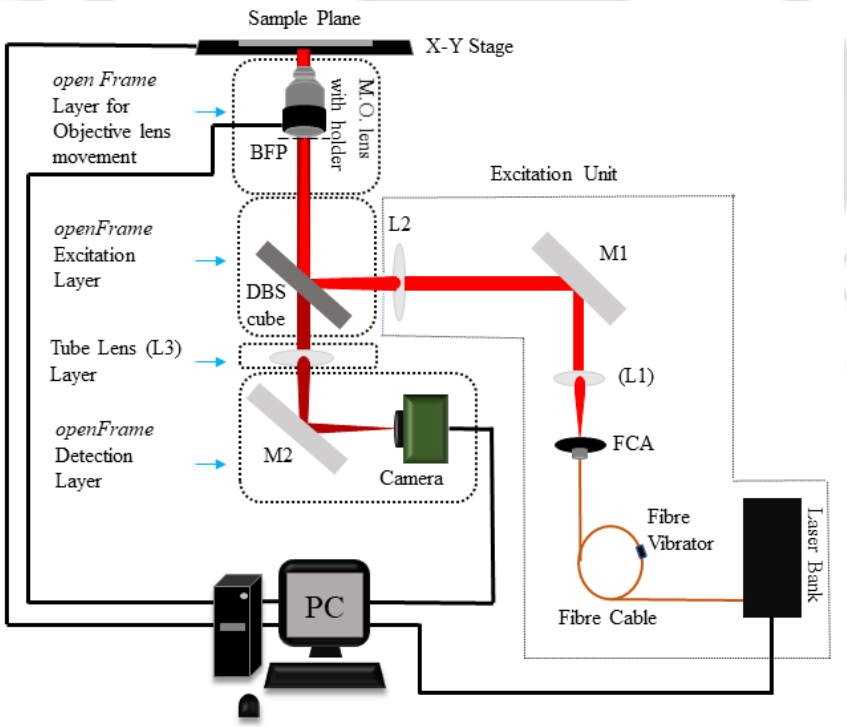

Figure 4.1: A schematic of the openFrame-based modular microscope working as easySTORM.

To realize easySTORM, we use the openFrame-based modular microscope in the widefield epi-fluorescence mode, as shown in Figure 4.1. The experiments demonstrated here utilize the 405 nm, 462 nm, and 638 nm multimode diode lasers from the microscope laser bank and the 1.3 NA objective lens (Plan Fluor 100×, Amscope). The combination of the lenses L1, L2, and the objective lens creates a uniform illumination on the sample plane. Fluorescence emission from the sample is collected by the objective lens and is transmitted through the DBS cube towards the tube lens L3, which focuses the emission onto the camera (CellCam Centro 200MR) after reflection from mirror M2. The combination of the tube lens (focal length of 200 nm) and the objective lens (focal length of 1.8 mm) results in a (1/111) times demagnification of a camera pixel on the sample plane so that the camera pixel size reduces to ≈ 21.6 nm.

4.2.2 Acquisition of Images

As mentioned earlier, STORM requires the acquisition of thousands of widefield fluorescence images at a high excitation intensity. This high intensity laser illumination drives the larger fraction of the excited fluorophores into the dark state and initiates the blinking, which is essential for localization in STORM. Before proceeding with the easySTORM image acquisition, the widefield fluorescence image of the sample is first captured using the excitation intensity at the lowest available range (≈ 0.02 kW/cm^2). Then the intensity of the laser is raised to its maximum (≈ 1.5 kW/cm^2 for 638 nm excitation and ≈ 1.25 kW/cm^2 for 462 nm excitation on the sample plane for biological samples) to initiate blinking. As soon as the blinking becomes sparse (typically after 10 seconds of continuous excitation), the laser intensity is reduced to ≤ 0.75 kW/cm^2 for 638 nm and ≤ 0.7 kW/cm^2 for 462 nm, and image frames for STORM are acquired at about 33 fps with an exposure time of 30 ms per frame. For reconstructing one super-resolved image, more than 10,000 image frames need to be acquired.

4.2.3 Image reconstruction and processing

After acquiring the widefield images of the sample, the images are loaded into the Fiji-ImageJ software. To do this, we go to the Bio-Formats → Bio-Formats Importer → of the plugin and choose the stack of widefield images (acquired in the format .ome or .tiff). Once the stack of images is chosen, the Bio-Formats Import Options

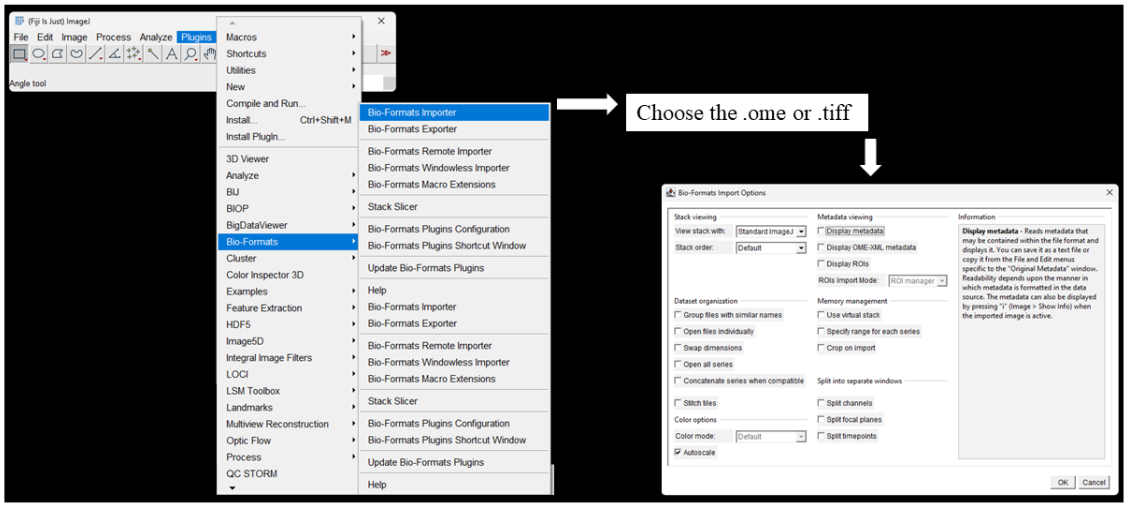

Figure 4.2: A screenshot showing the Bio-Formats Plugin in the Fiji-ImageJ software to load the stack of widefield images acquired during STORM image acquisition.

pop up, where the View stack option is kept as Standard ImageJ and the Stack order is left in the default state, as shown in Figure 4.2. Finally, the stack of images gets loaded into Fiji-ImageJ and is ready for image reconstruction and further processing.

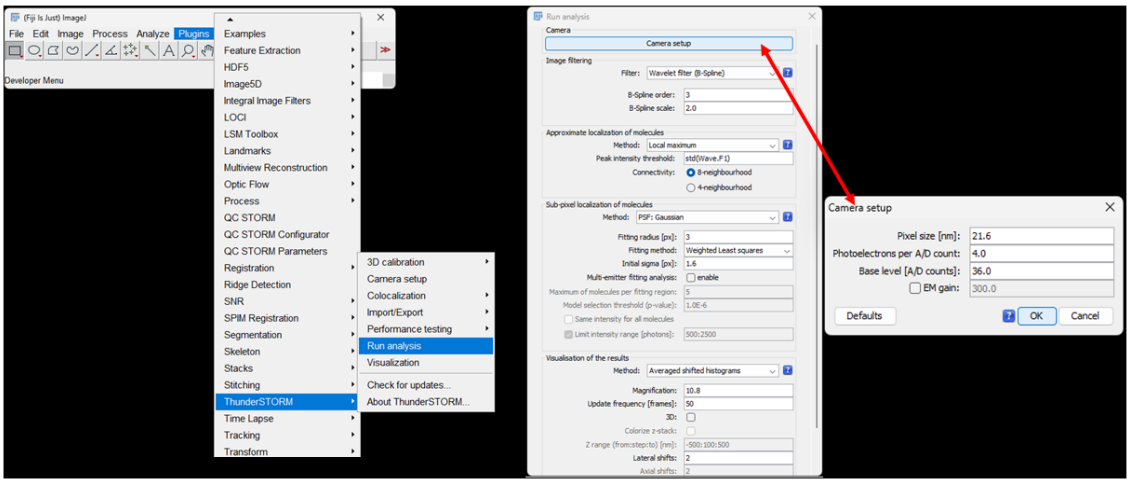

Figure 4.3: A screenshot showing the camera setup and the localization parameters inside the Run analysis option in ThunderSTORM before running the reconstruction process.

For reconstruction of the super-resolved image from the loaded image stack, we access the ThunderSTORM plugin from the Plugins list and select the Run analysis option. The Run analysis allows setting of the camera parameters, localization and fitting algorithms, filtering models, and display parameters required for reconstruction. This includes setting the camera pixel size in the sample plane, analog-to-digital (ADU) unit conversion, and background offset (base level), as shown in

Figure 4.3. As mentioned earlier, for our camera, the pixel size in the sample plane is 21.6 nm, the ADU conversion ratio is 3.6 (from the camera specifications), and the background offset is determined from the lowest greyscale intensity value in the widefield fluorescence image. Other options, such as localization and fitting algorithms, filtering, and visualization, are then set. These include Gaussian fitting of the PSF using maximum likelihood estimation [57], wavelet-based image filtering [58], and Average Shifted Histogram [59] for visualization.

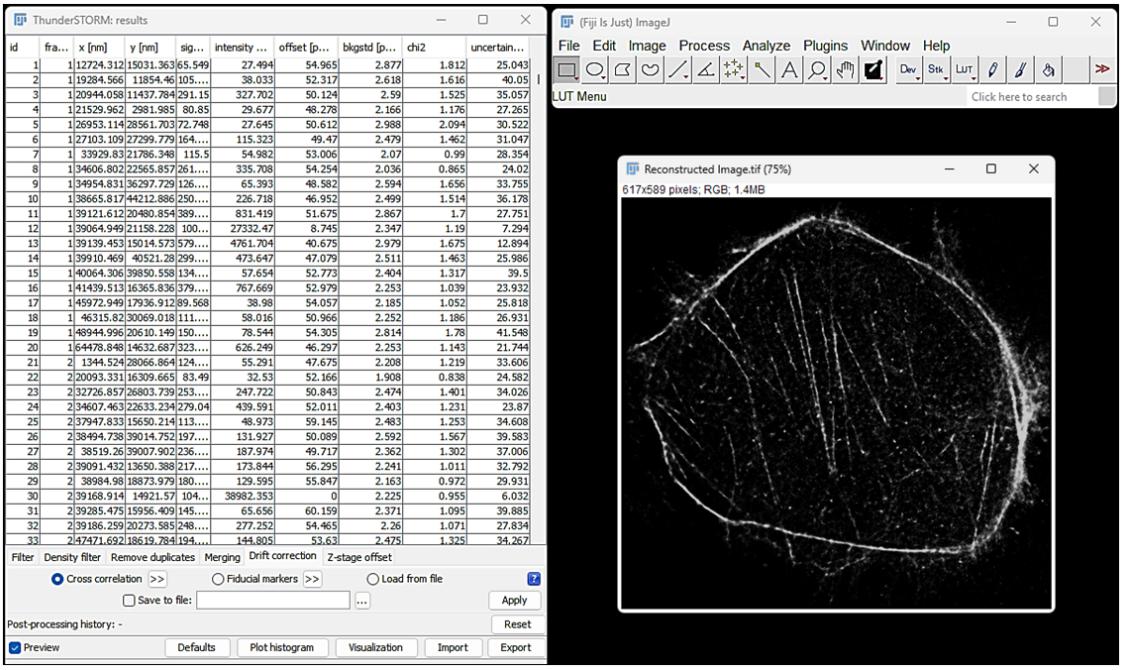

Figure 4.4: A screenshot of the reconstruction results in the ThunderSTORM presented in a tabular format, along with a reconstructed image. Additional options, such as drift correction, filtering and duplicate removal, can be applied at this stage before generating the reconstructed image.

After setting the parameters in Run analysis, the image analysis tool is next selected to display the reconstruction results in a tabular format, along with the image, as shown in Figure 4.4. Once these results are displayed, the image is further processed for the drift correction, using ThunderSTORM's built-in drift correction tool [57], before displaying the drift corrected reconstructed image. Additionally, at this stage, if required, additional post-processing, such as duplicates removal and filtering, can be applied to the reconstructed image using the appropriate options already available in ThunderSTORM. Further processing and analysis of the reconstructed image, such as pixel number to pixel distance calibration, ROI selection, intensity line plots, pseudo-coloring, and combination of multi-channel images, are

all performed in Fiji-ImageJ. The experimental arrangement includes a PC with sufficient storage, RAM, and processing speed for STORM image reconstruction, as STORM involves analyzing thousands of images. Here, we use a Dell OptiPlex 5080 equipped with 64 GB of RAM and a 2.90 GHz Intel® Core™ i7-10700 processor.

4.2.4 Preparation of samples

To demonstrate the easySTORM imaging with the modular microscope, we prepare samples of carboxyl quantum dots (QDs), human bone marrow-derived mesenchymal stem cells (MSCs), and human glioblastoma cells (U87MG cancer cells). In the following, we provide a detailed description of the sample preparation steps.

Sample preparation for MSCs for single-color easySTORM (638 nm excitation)

- Direct immunostaining of actin:
  To prepare samples of fluorescently labeled actin in mesenchymal stem cells (MSCs), we first acquire unutilized bone marrow aspirates from Guwahati Medical College Hospital, India [55]. MSCs are extracted from these aspirates following an identical process as previously reported [60]. MSCs are seeded at a density of 5000 cells/cm^2 on glass coverslips coated with bovine-plasma fibronectin (10 ng/cm^2, Sigma Aldrich), and then they are left to adhere and proliferate for 24 hours in a humidified CO_2 incubator. Afterwards, the cells are fixed with 4% formaldehyde in PBS for 20 minutes at room temperature after being cleaned with phosphate-buffered saline (PBS) that has been preheated to 37°C. After fixation, the cells undergo two PBS washes, permeabilization with 0.1% Triton X-100 (Merck) in PBS for 15 minutes, and again three washes with PBS. This is followed by blocking of the cells with 5% bovine serum albumin (BSA; Hi-Media) in PBS [61] and then incubation at 4°C overnight. For staining the actin filaments, Phalloidin-Alexa Fluor (AF) 647 (Invitrogen) is used [62]. To proceed with the staining, the incubated blocked cells are treated in a 1:1000 dilution of Phalloidin-AF 647 in 5% BSA-PBS solution for an entire night at 4°C [61]. This process is referred to as direct immunostaining [63]. The cells then undergo three washes with 2% BSA in PBS, followed by storing in PBS before mounting. For STORM imaging, coverslips are placed on the glass slides using a buffer containing

Mowiol based on PVA (MOWIOL 4-88 Reagent, 475904, Calbiochem) and 1% β-mercaptoethanol (β-ME) (Himedia) as a blinking reagent [64]. The slides are then incubated in an oven at 37°C for 24 hours and sealed with transparent nail varnish before proceeding for single-color STORM. As we will see later, in Section 4.3, this incubation step is very useful in preserving the sample for long term imaging.

Sample preparation for U87MG cells for single-color easySTORM (638 nm excitation)

- Direct immunostaining of actin:
  To prepare sample slides of fluorescently labeled actin in U87MG cells, the U87MG cell line is bought from the National Centre for Cell Science (Pune, India). The cells are kept in a humidified CO_2 incubator in high-glucose Dulbecco's Modified Eagle's Medium with an addition of 10% fetal bovine serum (FBS) to the medium. For staining purposes, cells are seeded at a density of 2000 cells/cm^2 on sterile glass coverslips and then cultured for 24 hours. Unlike MSCs, which use 5% BSA-PBS during immunostaining, actin of U87MG cells is directly immunostained with Phalloidin-AF 647 diluted in a 1:1000 ratio in a 2% FBS-PBS solution (v/v). The post-staining steps are performed following the same protocol as described earlier for MSCs.

- Indirect immunostaining of tubulin:
  To perform indirect immunostaining [63] of tubulin, U87MG cells are kept under incubation for 24 hours at 4°C with a primary antibody (rabbit anti-α-tubulin, Invitrogen) at a 1:750 dilution in 2% FBS-PBS. After washing the cells twice with the blocking solution, fluorescently tagged secondary antibody (donkey anti-rabbit IgG Alexa Fluor 647, Invitrogen) diluted at a 1:1000 in the blocking solution is dropped onto the coverslips containing the cells and allowed to incubate for the entire night at 4°C. The post-staining steps are similar to those described earlier for MSCs.

Sample preparation for U87MG cells for multi-color easySTORM and dual-color imaging in easySTORM-widefield (638 nm, 462 nm, and 405 nm excitations)

- Staining of actin-tubulin for 462 nm and 638 nm excitations:

To perform multi-color easySTORM in actin-tubulin of U87MG cells, first, the tubulin of the U87MG cells is incubated with the primary antibodies as discussed previously. After the primary antibody incubation stage, a 1:1 combination of Phalloidin-AF 488 (for direct immunostaining of actin) and AF 647-conjugated secondary antibody (for indirect immunostaining of tubulin) prepared in the blocking solution is dropped onto the coverslips and allowed to incubate overnight at 4°C. The combination of the AF 488 and AF 647 fluorophores helps visualize both tubulin and actin within the sample. The post-staining steps are similar to those discussed above. It should be noted that a 1:1 volumetric ratio of the fluorophores helps maintain comparable labeling densities of actin (Phalloidin–AF 488) and tubulin (AF 647-secondary antibody) and is not a strict physical requirement.

- Staining of actin-nucleus for 638 nm and 405 nm excitations:
  To perform dual-color imaging in easySTORM-widefield, we stain actin of U87MG cells with Phalloidin-AF 647 for STORM and then stain the nucleus of these cells with DAPI for widefield imaging. Following an overnight incubation with Phalloidin-AF 647 and two washes with 2% FBS-PBS, cells are incubated for five minutes at room temperature with DAPI, prepared in a 1:2000 dilution in 2% FBS-PBS. Finally, two washes with 2% FBS-PBS and two washes with PBS are performed before proceeding with the post-staining steps.

4.3 Initial challenges and their resolution

During the implementation of STORM, we encountered several practical challenges, particularly in the initial stages of its implementation. This Section discusses the key challenges faced and how they are eventually resolved.

4.3.1 Effect of sample mounting time on photobleaching of the sample

Initially, we implement easySTORM to image sample slides of AF 647 stained actin in MSCs. We notice that, on excitation with the 638 nm laser, the fluorophores in the sample get photobleached quickly, surviving less than a minute. For example, we show in Figures 4.5 (i) and (ii) (a), the widefield fluorescence images of actin from

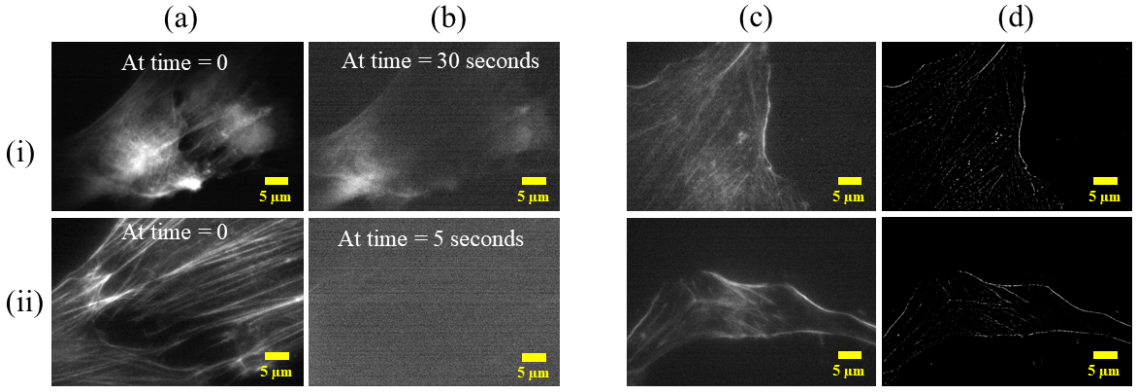

Figure 4.5: Widefield fluorescence images of two separate regions of actin stained with Phalloidin-AF 647 in the MSCs sample, captured at time = 0 in (i) (a) when excited with $\approx$ 0.2 kW/cm^2 and (ii) (a) when excited with $\approx$ 1.5 kW/cm^2 using 638 nm wavelength. (i) and (ii) (b) are the widefield images corresponding to (i) and (ii) (a) after 30 seconds and 5 seconds, respectively. (i) and (ii) (c) are widefield fluorescence images of two regions of Phalloidin-AF 647 labeled actin from sample slides of U87MG cells when excited with $\approx$ 0.2 kW/cm^2 intensity using 638 nm wavelength. (i) and (ii) (d) are the corresponding easySTORM images reconstructed from images acquired for 50 seconds.

two separate regions on the same sample slide when the intensity on the sample plane is $\approx$ 0.2 kW/cm^2 and $\approx$ 1.5 kW/cm^2, respectively. These two regions get photobleached within 30 seconds and 5 seconds, as shown in their respective widefield images in Figures 4.5 (i) and (ii) (b). The number of frames acquired for that much time is insufficient to reconstruct a super-resolved image in STORM. Additionally, we utilize STORM to image sample slides of AF 647 stained actin in the U87MG cells using 638 nm excitation. In Figures 4.5 (i) and (ii) (c), two widefield images are shown corresponding to two separate regions from the same sample slide of the U87MG sample, when excited with a sample plane intensity $\approx$ 0.2 kW/cm^2. The regions get photobleached after 50 seconds, and the number of imaging frames acquired for this period is not sufficient to reconstruct a super-resolved image, as shown in the Figures 4.5 (i) and (ii) (d) corresponding to Figures 4.5 (i) and (ii) (c), respectively. Although we follow standard immunostaining and sample preservation protocols as reported previously [44, 61], these do not help to reduce the fluorophore photobleaching in Mowiol supplemented with β-ME, as evident in Figure 4.5. Later, we find that the mounting time plays a pivotal role in keeping the sample preserved for a longer duration of imaging. Initially, the samples are brought for STORM imaging just after mounting the coverslips on the glass slides. However, as outlined in the Section 4.2.4, we later leave the coverslips to dry at 37°C for 24-48 hours

after mounting. Additionally, the coverslips, after getting sealed with nail varnish, are kept at 4°C for 24-48 hours before imaging. Over the course of the STORM experiments, we observe that these two steps reduce the photobleaching and preserve the sample for an extended duration of image acquisition, for samples mounted in Mowiol with β-ME.

4.3.2 Effect of temperature and humidity

Implementing STORM in high temperature and humid environments poses challenges to both technical procedures and the processes of sample preparation and preservation. Higher temperatures cause thermal drift, accelerate buffer evaporation, and promote microbial growth in the sample, while high humidity can lead to condensation on optical components and degrade the performance of sensitive electronics, like those in cameras and lasers. To ensure stable conditions during the STORM experiments, we maintain the imaging laboratory at 23°C with relative humidity set between 35-45%. Additionally, the laser working temperature is routinely monitored and matched to the laboratory temperature as outlined in Chapter 3. Moreover, the process of sample preparation and preservation is carried out following the appropriate protocols as described in Section 4.2.4.

4.3.3 Effect of camera exposure time

For recording a sufficient number of fluorophore blinking events during STORM image acquisition, the exposure time of the camera is crucial. Without an appropriate exposure time, the camera fails to record enough blinking, and thus, the resolution in the reconstructed image is poor. We find that the exposure time of the camera should be between 20-100 ms to acquire a sufficient number of blinking events for both AF 647 and AF 488 in Mowiol with β-ME. We therefore keep the exposure time at 30 ms for optimum performance during the entire work.

4.4 Results

After resolving the initial challenges as discussed in the Section 4.3, we conduct several experiments to demonstrate the performance of our openFrame-based modular easySTORM system.

4.4.1 easySTORM imaging of QDs

We first chose to perform easySTORM in the modular microscope by imaging the QD slide. A stack of widefield images of a region from the QD sample is acquired on the camera by exciting with 462 nm laser beam, keeping the intensity 0.5 kW/cm^2 on the sample plane. Figure 4.6 (i) displays the widefield fluorescence image of the QDs in (a) and the reconstructed super-resolved image of the same region in (b). The reconstructed images in Figure 4.6 (i) (c) highlight two magnified regions,

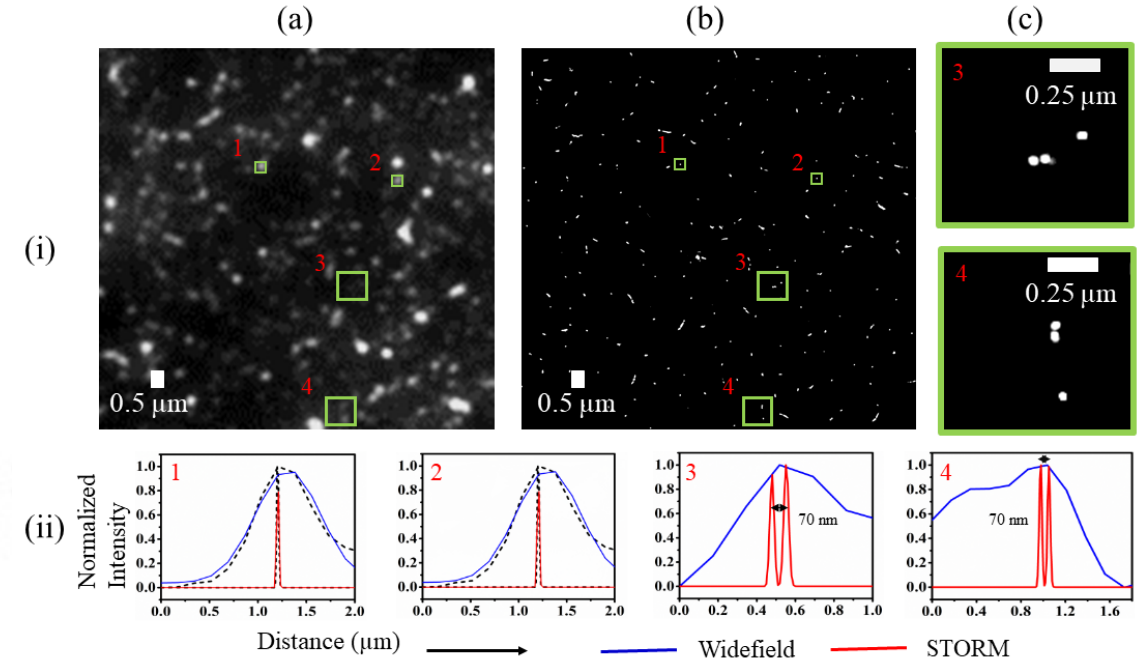

Figure 4.6: A widefield fluorescence image of a selected region on the QD sample slide (i) (a), as recorded on the camera, under 462 nm excitation and (i)(b) its corresponding easySTORM image. Regions 3 and 4 from (i) (b) are magnified and shown in (i) (c). (ii) Presents normalized intensity profiles across the PSFs in regions 1, 2, 3, and 4 from images (i) (a) and (b).

denoted as 3 and 4 in Figure 4.6 (i) (b). In Figure 4.6 (ii) (1,2), the normalized intensity plots of the raw data corresponding to the ROIs 1 and 2 in the widefield fluorescence and their respective super-resolved images are shown. The average FWHM measured from intensity line plots across isolated QDs in Figure 4.6 (i) (b) is $\approx 24.67 \pm 0.55$ nm. Figures 4.6 (ii) (3,4) display line plots of ROIs 3 and 4 in Figure 4.6 (i) (b) through the centers of two neighboring QDs. We see that two QDs, 70 nm apart, are getting resolved in our implementation of the easySTORM microscope. Additionally, we evaluate the localization precision of the QDs, defined as $\sigma/\sqrt{N}$

(mentioned in Chapter 2), where N denotes the number of photons detected per emitter estimated from the camera image and σ represents the standard deviation of the fitted Gaussian PSF [38]. The mean localization precision, averaged over all frames of the reconstructed image, is found to be $\approx$ 10 nm, based on the results given using ThunderSTORM.

4.4.2 Single-color easySTORM imaging of actin in human bone marrow-derived MSCs

To show the utility of our easySTORM system in biomedical applications, we first perform single-color easySTORM to visualize actin in MSCs tagged with Phalloidin-AF 647, under 638 nm excitation. The excitation intensities on the sample plane required for widefield imaging, blinking activation, and image acquisition are as already outlined in the Section 4.2.2. Figure 4.7 (i) (a) is the widefield image of

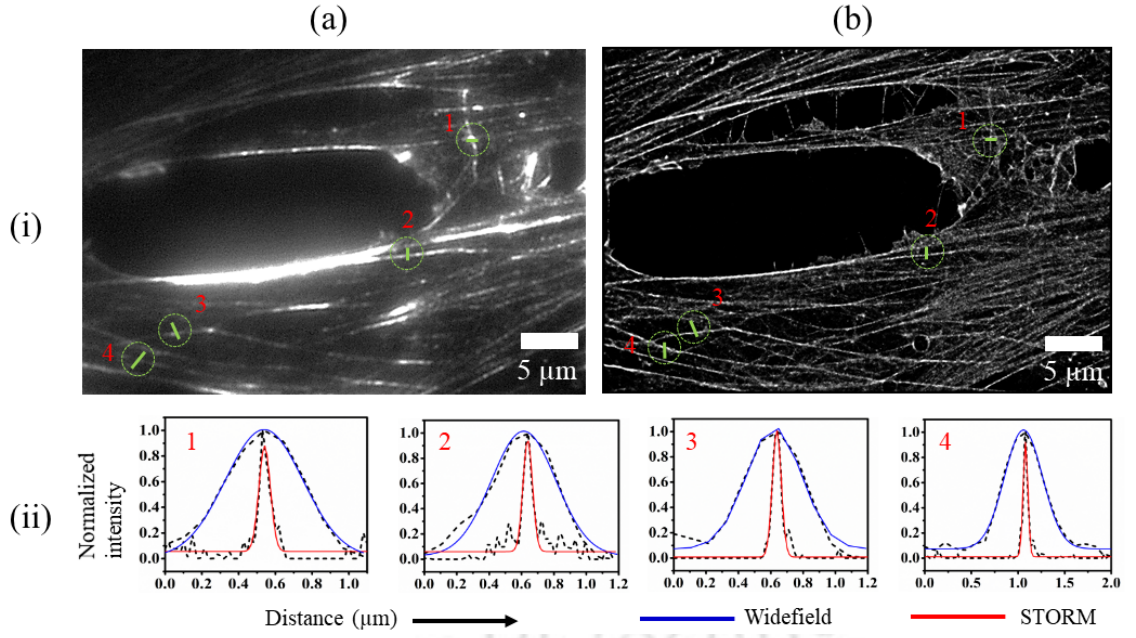

Figure 4.7: Actin in MSCs labeled with Phalloidin-AF 647 is excited with 638 nm wavelength, and the camera captures (i) (a) the widefield fluorescence image, while (b) is the corresponding easySTORM image. (ii) Gaussian-fitted normalized line profiles across actin in regions designated 1, 2, 3, and 4 in (i) (a) and (b). The intensity profiles from the widefield images have FWHMs ranging from 400 nm to 496 nm, whereas the super-resolved images have FWHMs between 55 nm to 77 nm.

an area on the sample slide, and its corresponding easySTORM image is seen in Figure 4.7 (i) (b). Normalized intensity line profiles labeled as 1, 2, 3, and 4 from

the widefield and super-resolved images are shown in Figure 4.7 (ii). The FWHMs of these line profiles fall between 400 to 496 nm in the widefield image and between 55 and 77 nm in the super-resolved image.

4.4.3 Single-color easySTORM imaging of actin and tubulin in U87MG cells

To show the utility of our easySTORM microscope in cancer research, we perform single-color easySTORM imaging of actin and tubulin in U87MG cells. First, we image Phalloidin-AF 647 labeled actin in U87MG cells by exciting with 638 nm laser. We keep the same excitation intensities on the sample plane, as outlined in the Section 4.2.2. Figures 4.8 (i) (a) and (b) display the widefield fluorescence image of

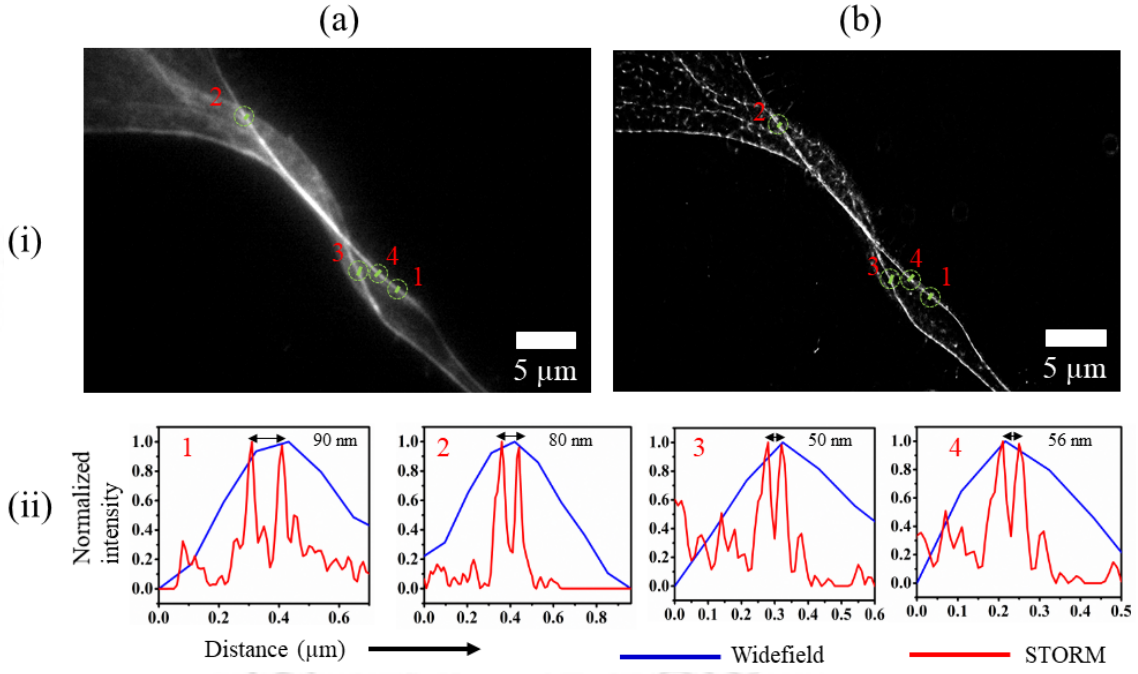

Figure 4.8: (i) (a) The widefield fluorescence image, and (i) (b) the corresponding easySTORM image of actin in U87MG cells labeled with Phalloidin-AF 647 when excited with 638 nm wavelength. (ii) Normalized line profiles across actin along regions designated as 1, 2, 3, and 4 in the widefield fluorescence and super-resolved images.

an FOV on the sample and its reconstructed super-resolved image, respectively. For the regions labeled as 1, 2, 3, and 4 in Figures 4.8 (i) (a) and the same regions in (i) (b), the intensity line plots are presented in Figure 4.8 (ii). These line plots show that the widefield fluorescence image lacks finer details compared to the super-resolved

image. The distance between two closely spaced actin in easySTORM images ranges from 50 to 90 nm, which agrees well with previously reported data [40].

Next, we perform easySTORM on sample slides of tubulin stained with AF 647-conjugated secondary antibody in U87MG cells by exciting at 638 nm. Figures 4.9 (i) and (ii) (b) show the reconstructed images of two distinct FOVs, and their respective widefield fluorescence images are seen in Figures 4.9 (i) and (ii) (a). Figures 4.9 (i) and (ii) (c) show two ROIs labeled as 1 and 2, from each of these widefield and reconstructed images. Figures 4.9 (i) and (ii) (d) show the respective intensity line plots through the ROIs in Figures 4.9 (i) and (ii) (c). Line plots between two tubulin structures in the reconstructed images show separations of 120 nm and 150 nm, respectively, revealing tiny structures not resolvable in the widefield images.

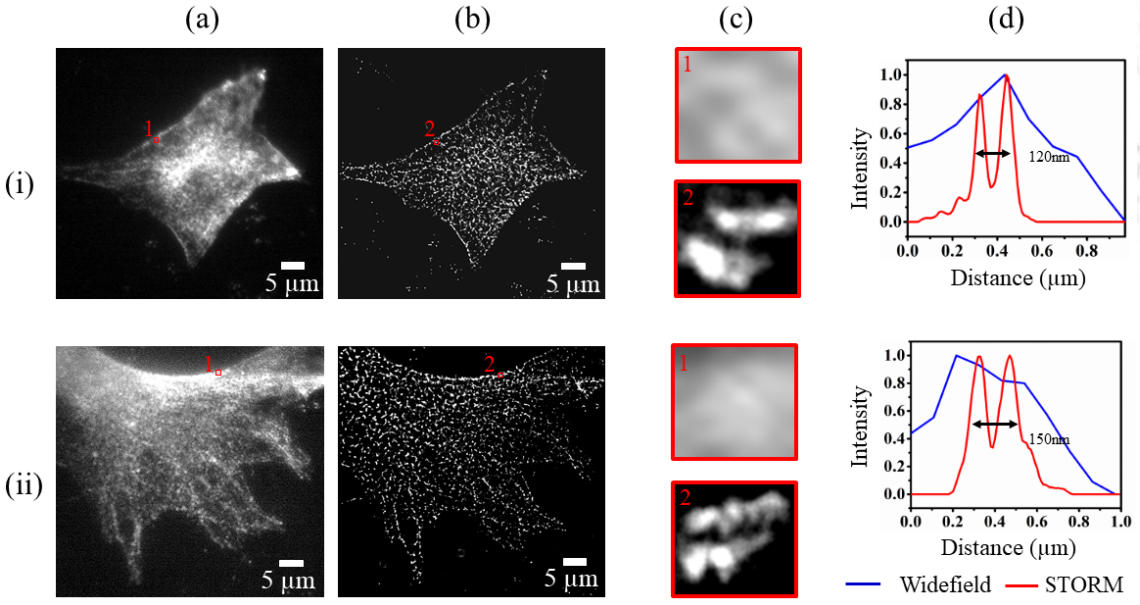

Figure 4.9: Widefield fluorescence images of tubulin in U87MG cells tagged with AF 647 are displayed in (i) and (ii) (a), using a 638 nm excitation laser. (i) and (ii) (b) display the corresponding reconstructed super-resolved images of these regions. (i) (c) shows the magnified images of regions 1 and 2 from (i) (a) and (b), while (ii) (c) shows the magnified views of regions 1 and 2 from (ii) (a) and (b). (i) and (ii) (d) show the normalized intensity line profiles across the regions from (i) (c) and (ii) (c), respectively.

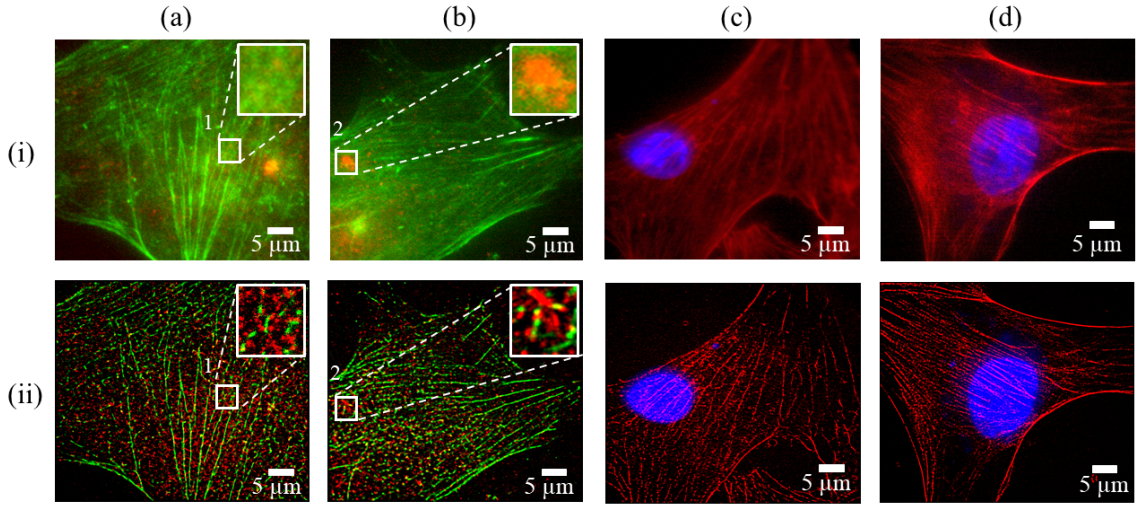

Figure 4.10: Widefield fluorescence images of (i)(a) Phalloidin-AF 488 labeled actin in U87MG cells (pseudo-colored green), excited with 462 nm wavelength and (i)(b) secondary-AF 647 tagged tubulin (pseudo-colored red), excited with 638 nm wavelength. (ii) (a) and (b) show the respective ThunderSTORM reconstructed multi-color super-resolution images. (i) (c) and (d) display the widefield images of Phalloidin-AF 647 tagged actin (pseudo-colored red) superimposed on DAPI stained nucleus (pseudo-colored blue), (ii) (c) and (d) represent the respective reconstructed easySTORM images of actin superimposed with the respective widefield image of the nucleus from (i) (c) and (d). Actin is excited at 638 nm, and the nucleus is excited at 405 nm in (i), (c), and (d).

4.4.4 Multi-color easySTORM of actin-tubulin and dual-color visualization in easySTORM-widefield of actin-nucleus in U87MG cells

To illustrate our system's multi-color OSRM capability utilizing easySTORM, we image fluorescently tagged actin-tubulin in U87MG cells. Actin is labeled using Phalloidin-AF 488 and excited with 462 nm laser, while tubulin is labeled using AF 647-conjugated secondary antibody and excited with 638 nm laser. During imaging, we set the excitation intensities for AF 488 and AF 647 in the desired range, as mentioned in the Section 4.2.2. Figures 4.10 (i) (a) and (b) show widefield fluorescence images of tubulin and actin structures, with tubulin pseudo-colored in red and actin pseudo-colored green. Figures 4.10 (ii) (a) and (b) show the respective reconstructed images. Figure 4.10 (i) (a) and Figure 4.10 (ii) (a) show, in the insets, the ROIs in the widefield and their corresponding easySTORM images, respectively. It has been observed from the STORM image that tubulin fine structures coexist with actin, which is otherwise not easily observed in the widefield image, where most

of the image is primarily in green, indicating only the presence of actin. Similarly, a different ROI in Figure 4.10 (ii) (b) indicates the presence of actin and tubulin fine structures, which are not visible in the widefield image of Figure 4.10 (i) (b).

Additionally, we perform dual-color visualization of actin-nucleus in U87MG cells with easySTORM-widefield imaging. Actin (pseudo-colored in red) is stained with Phalloidin-AF 647 and excited using 638 nm laser, nucleus (pseudo-colored in blue) is labeled with DAPI and excited using 405 nm laser. The excitation intensities for imaging AF 647 during STORM acquisition remain the same as described earlier, while the widefield fluorescence images of the DAPI stained nucleus are captured employing 405 nm with an intensity ≈ 0.05 kW/cm^2 on the sample plane. Widefield images of the two-color labeled actin-nucleus from two different regions are shown in Figures 4.10 (i) (c) and (d). Figures 4.10 (ii) (c) and (d) display the respective easySTORM reconstructed images of actin merged with the widefield images of the respective nucleus.

4.5 Summary

In this Chapter, we have presented the implementation of easySTORM-based OSRM, using the openFrame-based modular microscope. The Chapter describes image acquisition, reconstruction, and analysis workflows, along with sample preparation protocols optimized for STORM. It also outlines the key challenges encountered initially during STORM implementation and the resolutions to overcome them. To validate the capabilities of the modular easySTORM system, we have performed single-color imaging of QDs, fluorescently tagged actin, and tubulin in normal human cells and brain cancer cells. Further, the potential of our system has been demonstrated in multi-color STORM imaging of actin-tubulin and two-color visualization of actin-nucleus in brain cancer cells using STORM-widefield. The findings presented in this Chapter indicate that the openFrame-based easySTORM microscope is an affordable yet effective OSRM system that can work in hot, humid environments of tropical climatic regions like the Indian and Asian subcontinent.

* * *

Chapter 5

Effect of excitation and photoinduced recovery intensity for resolution enhancement in STORM

5.1 Introduction

As discussed earlier, STORM imaging relies on a specialized environment (imaging buffer) composed of chemical reagents that induce controlled fluorophore blinking or photoswitching through redox chemistry [65, 66]. However, chemical interactions among the reagents leading to buffer acidification, as well as high excitation intensities, can degrade fluorophores, limiting blinking duration and reducing the number of localizations and eventually degrading the resolution in STORM [67, 68]. Maintaining stability during imaging, therefore, requires suitable buffers and optimized illumination schemes. Semisolid antifading media composed of glycerol-based Mowiol, supplemented with a thiol-based blinking reagent such as β-ME (beta-mercaptoethanol), provide improved fluorophore stability, enable longer acquisitions, and allow sample preservation for extended periods, as mentioned in Chapter 4. Despite this, prolonged excitation eventually drives fluorophores into long-lived dark states, fundamentally limiting acquisition time and achievable resolution in STORM [61, 69, 70]. To restore sustainable fluorescence and blinking in STORM, external strategies can be utilized, among which the photoinduced recovery technique is widely used. This technique employs ultraviolet (UV) or violet illumination to reverse long-lived dark states and restore the photophysical activity of fluorophores, enabling them to take part in fluorescence and blinking [21, 35]. While photoinduced recovery has been extensively studied in aqueous imaging buffers [71, 72, 73], its effectiveness in semisolid media such as Mowiol remains largely unexplored [74]. Here, using the openFrame-based modular easyS-

TORM system, we study the influence of excitation (at 638 nm) and photoinduced recovery (using 405 nm and UV) beam intensities on the blinking duration of AF 647 labeled biological samples mounted in Mowiol with β-ME. From these experiments, we identify the optimized illumination intensity conditions in STORM that help to sustain the blinking for extended durations, thereby enhancing the resolution in the reconstructed images. Finally, we utilize these optimized illumination conditions in STORM to compare the widths of cytoskeletal structures in human stem cells and cancer cells.

5.2 Theory

5.2.1 Photoinduced recovery mechanism

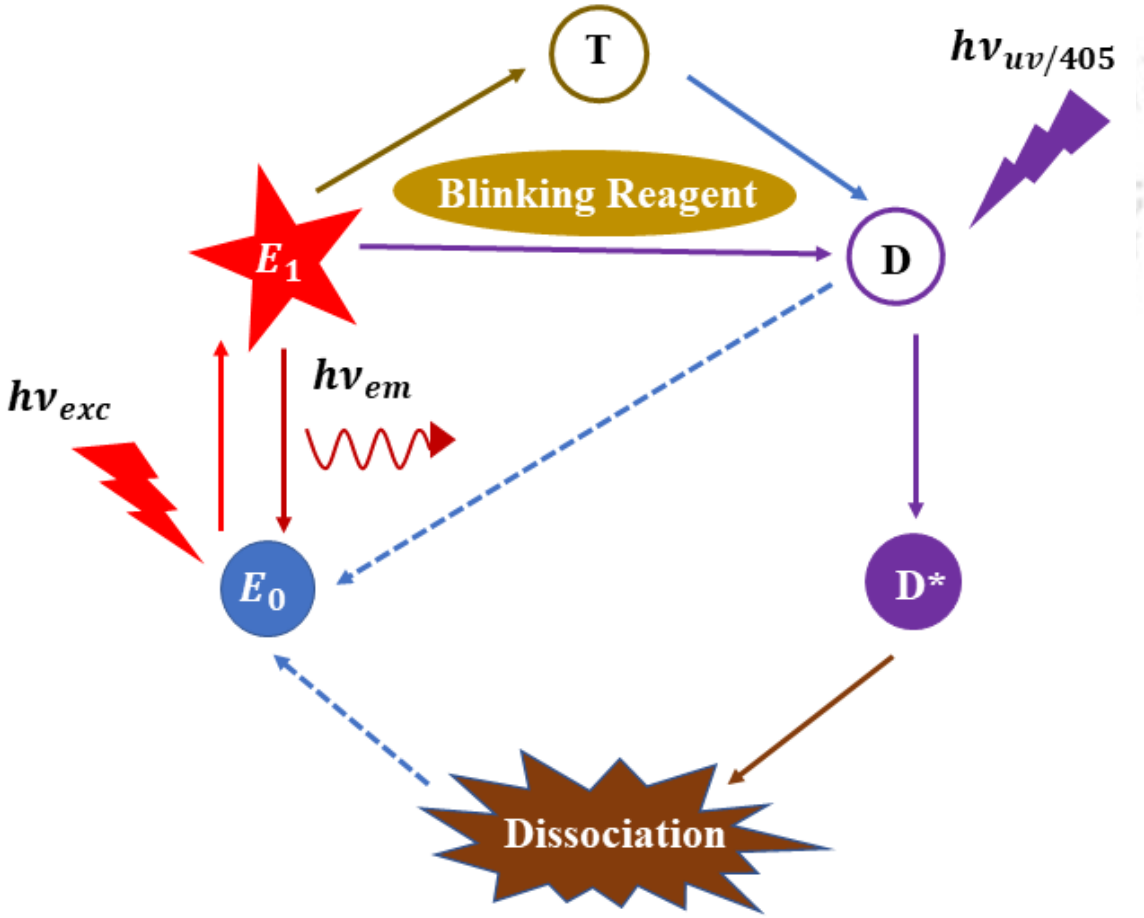

Figure 5.1: Illustration of fluorescence recovery cycle utilizing the photoinduced recovery mechanism.

As mentioned earlier, stochastic blinking of fluorophores in STORM requires the excited fluorophores to enter a dark state. However, the dark state fluorophores are long-lived, and when all the fluorophores enter this state, the fluorescence is eventually lost. In order to drive the fluorophores for continuous participation in the fluorescence and blinking cycle, a recovery mechanism using external means is needed. Photoinduced fluorescence recovery is such a mechanism in which illumination with specific wavelengths triggers the dark state fluorophores to recover their fluorescence state [75, 76].

In Figure 5.1, a schematic of the photoinduced recovery process of a fluorophore or a fluorescent molecule from its dark state in the presence of a photoinduced recovery beam is shown. The molecule in its singlet ground state (E_o) transits to an excited singlet state (E_1) by absorbing a photon from the excitation beam ($h\nu_{exc}$), from where it emits fluorescence ($h\nu_{em}$) (at an interval of the order of nanoseconds). There is a possibility that a few fluorophores may undergo an intersystem crossing from E_1 to a triplet state (T) and then non-radiatively return to E_o within microseconds interval [77]. In the presence of a blinking reagent, like β-ME, which is normally a reducing agent, some fluorophores enter into the long-lived dark state (D) via T. There is also a certain probability that the excited fluorophores may enter into the D state directly, in the presence of the blinking reagent. Once a molecule reaches the dark state, it can take time from milliseconds to minutes to even hours for this molecule to undergo non-radiative relaxation back to E_o [78], interrupting the continuous fluorescence emission. During the $E_o \rightarrow E_1 \rightarrow T \rightarrow D \rightarrow E_o$ cycle, fluorophores display random fluorescence blinking events [36, 79]. Any research-grade camera tuned to capture images with millisecond exposure mostly detects continuous fluorescence emission and seldom detects fluorescence blinking at low excitation intensities [80, 81]. It is necessary to increase the excitation intensity to produce noticeable blinking [74]. However, under strong excitation, over time, the fluorophores accumulate significantly in the D state and eventually the $E_o \rightarrow E_1 \rightarrow T \rightarrow D \rightarrow E_o$ cycle stops [82]. To restore this cycle immediately and to sustain the blinking process during excitation, the photoinduced recovery beam at 405 nm or UV wavelengths needs to be employed. In our work, it is observed that continuous excitation of AF 647 at 638 nm leads to a reduction in the fluorescence intensity as the AF 647 moves into the dark state (D). When exposed to $h\nu_{uv/405}$, the molecules in D state transition into an excited reduced dark state (D$*$). They then return to the fluorescence emission cycle $E_o \rightarrow E_1 \rightarrow T \rightarrow D \rightarrow D* \rightarrow E_o$ after

non-radiatively relaxing from D∗ and continue blinking [83] within the fluorophores' photobleaching threshold [76], before experiencing permanent photodamage [84, 85].

5.3 Materials and methods

5.3.1 Experimental Arrangement

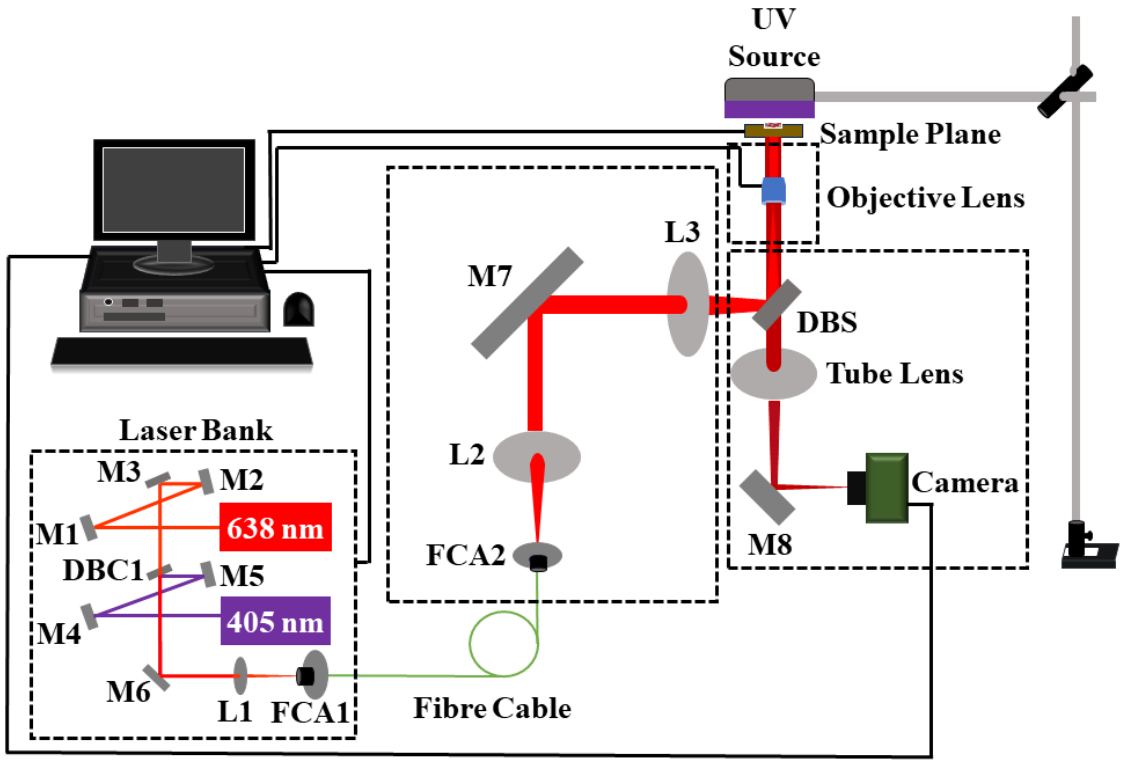

Figure 5.2: A schematic of the experimental setup showing the optical elements, illumination sources, sample plane, and detector.

To demonstrate experimentally, we use our openFrame-based modular microscope in the widefield epi-fluorescence mode, as shown in Figure 5.2. Here, we use the 638 nm and the 405 nm lasers from the laser bank. The DBS, the camera (monochrome), the tube lens, and the objective lens remain the same as mentioned in Chapters 3 and 4. Additionally, we utilize an external, low-cost broadband UV lamp (350-380 nm) (108879, Farnell InOne) and position it above the sample plane to realize a flexible configuration for microscopes that lack a 405 nm laser or specialized optics for the same. Power densities on the sample plane range from 0.02 to 0.8 kW/cm^2 for the 405 nm laser and 0.2 to 1.3 kW/cm^2 for the 638 nm laser.

In contrast, the external UV lamp provides a stable intensity of ≈ 0.10 mW/cm^2 on the sample plane. To acquire the widefield images, the camera exposure period is kept at 30 ms, while reconstruction of the acquired images is performed, utilizing ThunderSTORM, with similar reconstruction parameters, as outlined in Chapter 4.

5.3.2 Sample preparation

Sample preparation to study resolution enhancement in STORM utilizing photoinduced recovery

To demonstrate the resolution enhancement in STORM utilizing the photoinduced recovery technique, we prepare microscope sample slides of U87MG cells by following a similar sample preparation procedure as mentioned in Chapter 4. The sample preparation mainly involves direct immunostaining of actin in U87MG cells with Phalloidin-AF 647 fluorophores and mounting in Mowiol supplemented with β-ME.

Sample preparation for comparing widths of cytoskeletal elements in MSCs, U87MG cells, and MDA MB 231 cells

To compare the widths of cytoskeletal structures (i.e., actin), we prepare separate samples of directly immunostained actin with AF 647 in three types of biological cells, MSCs, U87MG cells, and MDA MB 231 cells (breast cancer) [86]. A similar sample preparation process is followed for these cells, as outlined in Chapter 4.

5.4 Illumination schemes for photoinduced recovery

To observe resolution enhancement in STORM utilizing photoinduced recovery beams, four distinct illumination schemes are employed.

Scheme-A

The 638 nm beam is used to excite the sample, and the resultant fluorescence is recorded on the camera till the fluorescence intensity matches the background.

Scheme-B

After turning on the 638 nm laser, the sample's fluorescence is recorded until it decays and matches the background level. At this point, the fluorescence is revived by switching on the recovery beam, and the fluorescence is recorded until it reaches the background again.

Scheme-C

The 638 nm excitation and the photoinduced recovery beams are switched on simultaneously, and the fluorescence is recorded until it drops to the background level.

Scheme-D

After turning on the 638 nm excitation, fluorescence is recorded until it drops to the background. At first, the recovery beam is switched on for about a second, and the fluorescence is collected until it reaches the background once again. As soon as it drops to the background, the recovery beam is switched on again (for one second). The cycle is continued until the fluorescence emission fades away completely.

5.5 Results and discussion

5.5.1 Detection of background fluorescence without photoinduced recovery

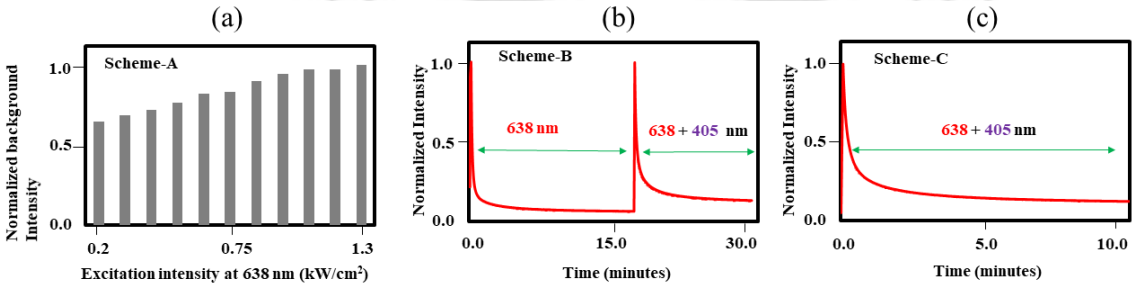

Figure 5.3: (a) The variation in the mean normalized background signal under Scheme-A illumination, as the excitation intensity increases. Using a 405 nm recovery beam, the variation of the normalized fluorescence signal with time under (b) Scheme-B illumination and (c) Scheme-C illumination.

Before employing the photoinduced recovery, it is important to quantify the background signal arising from the sample at different excitation intensities, so that its contribution can be appropriately accounted for during the experiments. Accordingly, a sample slide of Phalloidin-AF 647 stained actin in U87MG cells is illuminated under Scheme-A, and fluorescence emission of the sample is recorded. We then search for a region on the slide where there is no fluorescence emission from AF 647 dyes, but there are only redundant emissions, recorded as the background fluorescence. The intensity of the 638 nm excitation beam in the sample plane is varied from $\approx$ 0.2-1.3 kW/cm^2 and the changes in the background fluorescence signal at different excitation intensities are recorded. It is observed that the intensity of the background fluorescence increases almost linearly with the increase in the excitation beam intensity, as seen in Figure 5.3 (a). This observation implies that at any given power of the excitation beam, the sample without the AF 647 dyes generates a background fluorescence.

5.5.2 Photoinduced recovery with 405 nm

After measuring the background emission, we employ the illumination Schemes B and C with 638 nm as the excitation wavelength and 405 nm as the recovery beam by choosing an area on the same sample slide where we observe fluorescence. For Scheme-B, the fluorescence signal first increases before rapidly decaying to the background. At this point, the 405 nm recovery beam is turned on, due to which the fluorescence recovers and it rises momentarily, as shown in Figure 5.3 (b), before decaying back to the background level. For Scheme-C, both lasers are simultaneously switched on as shown in Figure 5.3 (c), causing an initial rise in the fluorescence that decays quickly to background.

The effects of the excitation and recovery beam intensities on the fluorescence duration utilizing Scheme-B are then systematically examined. We change the intensity of the 405 nm recovery beam from 0.04 kW/cm^2 to 0.8 kW/cm^2 and maintain the 638 nm excitation at a constant value. For each measurement, a fresh region on the sample is selected, and the experiments are repeated at excitation intensity values of 0.5, 0.75, 1, and 1.3 kW/cm^2, to record the fluorescence duration for each intensity. According to the bar plot in Figure 5.4 (a), the fluorescence blinking duration is the longest when the 405 nm beam intensity is between 0.04 and 0.1 kW/cm^2, with an ideal excitation intensity of $\approx$ 0.5 kW/cm^2 from the 638 nm laser.

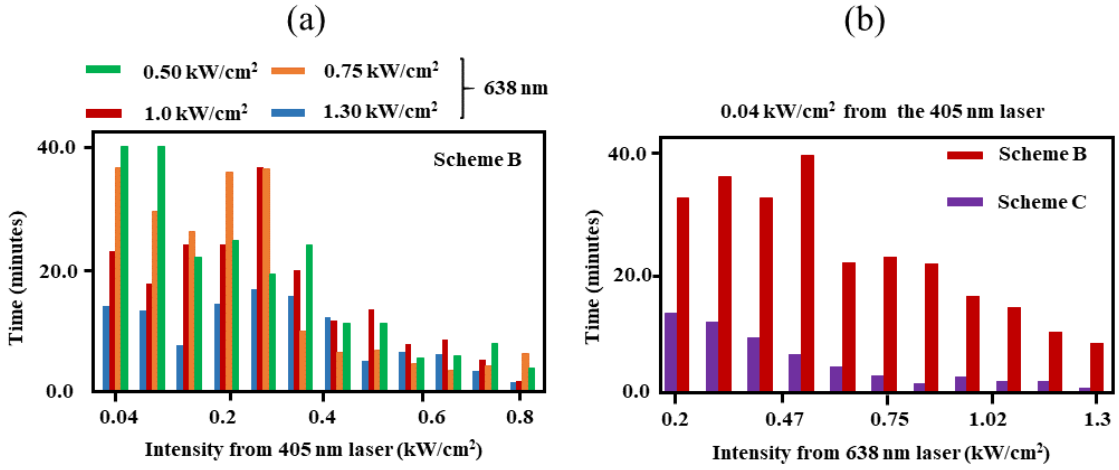

Figure 5.4: (a) Bar plots, depicting the time of the total fluorescence signal due to four intensity levels of the 638 nm laser under Scheme-B illumination, when the 405 nm recovery beam intensity is increased from 0.04 kW/cm^2 to 0.8 kW/cm^2. (b) Bar plots for the total fluorescence signal duration, under both Scheme-B and Scheme-C illumination, when the 405 nm recovery beam is kept at 0.04 kW/cm^2, and the intensity of the 638 nm laser is increased from 0.2 kW/cm^2 to 1.3 kW/cm^2. The position of the blue bar in (a) indicates the 405 nm intensity, while the violet bar in (b) denotes the 638 nm intensity for each bar group.

Subsequently, the fluorescence blinking times for Schemes B and C are evaluated by varying the 638 nm excitation beam from 0.2 to 1.3 kW/cm^2, keeping the 405 nm recovery beam at 0.04 kW/cm^2. Analysis of the fluorescence signal periods from the experiments reveals that Scheme-B offers a longer blinking duration than Scheme-C. As seen in the bar plot of Figure 5.4 (b), the ideal intensity level of the 638 nm laser is $\approx$ 0.5 kW/cm^2 (indicated by red color bars). Scheme-D is then employed to further investigate the fluorescence recovery while varying the 638 nm excitation intensities on the sample plane. For each excitation intensity at 638 nm, as soon as the fluorescence decays to the background level, the 405 nm beam is briefly activated ($\approx$ 1 second), producing a sudden spike in the fluorescence, which eventually fades. The brief activation of the 405 nm is repeated as soon as the fluorescence fades away. This momentary activation of the 405 nm at brief intervals is continued until there is no further fluorescence detected on the camera. In Figure 5.5, we show the variation of the normalized fluorescence intensity with time, for a range of excitation intensities and for different photoinduced intensity levels. The inset of each plot shows the fluorescence spikes at 2 minute intervals. It is observed from a series of experiments using Scheme-D that the frequency of the spikes rises as the strength of the excitation increases. The number of frames acquired through Scheme-D is

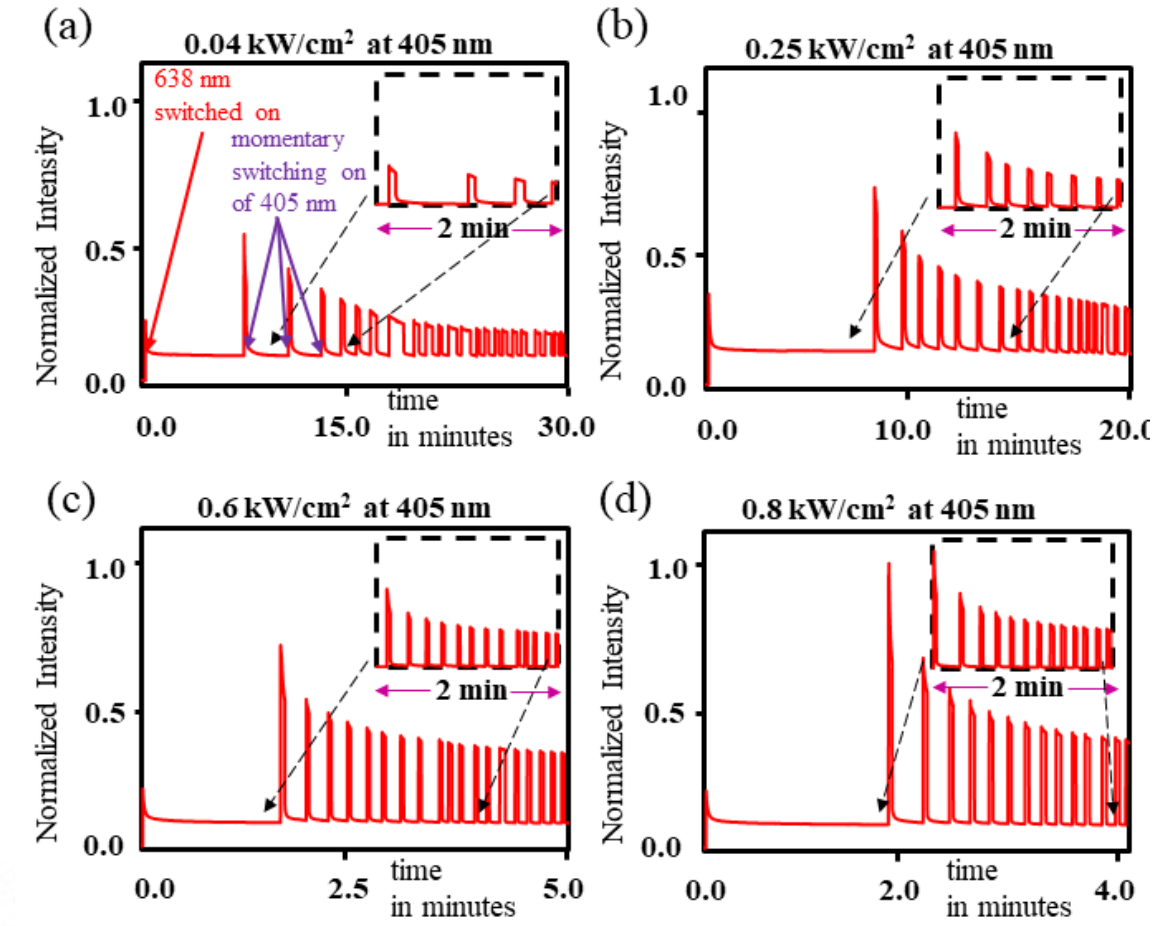

Figure 5.5: With the 405 nm laser intensity in the sample plane set to (a) 0.04 kW/cm^2, (b) 0.25 kW/cm^2, (c) 0.6 kW/cm^2 and (d) 0.8 kW/cm^2, the net fluorescence intensity variation over time under Scheme-D illumination.

similar to that of Scheme-B. However, Scheme-B is more useful and effective than Scheme-D for extending fluorescence blinking duration, as Scheme-D requires the camera to be activated at the exact instant of peak fluorescence emission, which is more complicated to achieve. Further switching the recovery beam on and off at quick intervals, as shown in Scheme-D, requires additional arrangement. Thus, it can be concluded that Scheme-B is the most efficient illumination scheme, with 0.5 kW/cm^2 as the excitation intensity on the sample plane at 638 nm while keeping 405 nm recovery intensity at 0.04 kW/cm^2.

For the experimental demonstration, we perform easySTORM imaging of AF 647 labeled actin in U87MG samples. The experiments are performed utilizing Schemes A and B, with the 638 nm intensity at 0.5 kW/cm^2 and 405 nm recovery at 0.04 kW/cm^2 on the sample plane. At first, a widefield fluorescence image (pseudo-

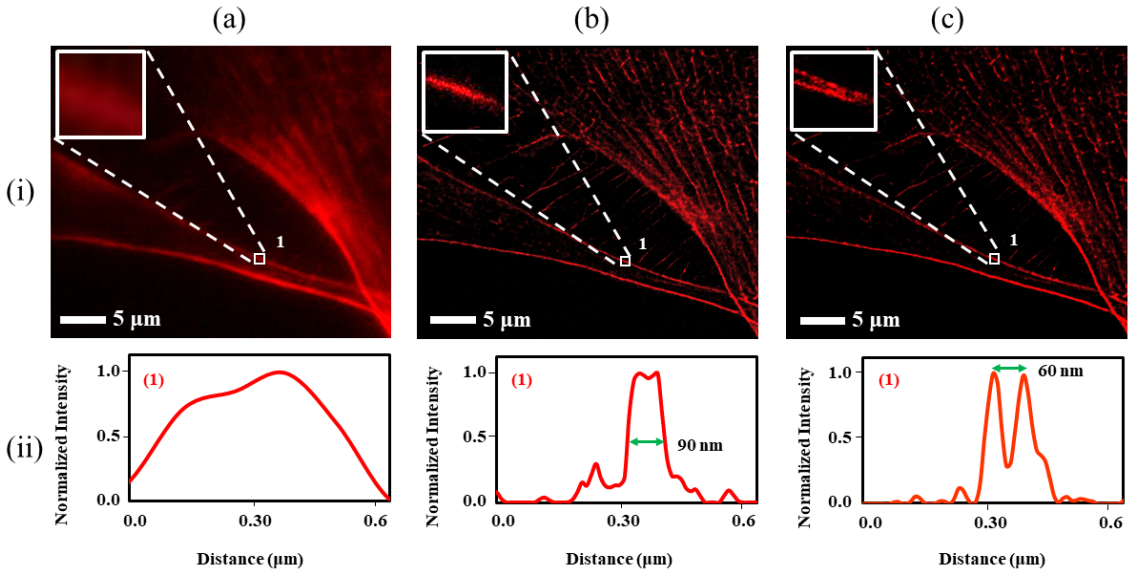

Figure 5.6: (i) (a) The conventional widefield fluorescence image, (b) the corresponding super-resolved image reconstructed with Scheme-A illumination, and (c) a super-resolved image reconstructed with Scheme-B illumination of Phalloidin-AF 647 labeled actin in U87MG cells, excited at 638 nm. (ii) (a-c) are the line plots for the regions designated as 1 in (i) (a-c).

colored in red) of an area on the sample is captured and is seen in Figure 5.6 (i) (a). This is followed by capturing 8000 frames containing blinking events using Scheme-A and then capturing an additional 12,000 frames after fluorescence recovery using Scheme-B for the same area. Overall, the number of imaging frames increases by 2.5 times due to the application of Scheme-B, compared to Scheme-A. Figures 5.6 (i) (b) and (c) display the super-resolved STORM images (pseudo-colored in red) from the original 8000 frames and from the overall 20,000 frames, respectively. It is seen in the inset images that actin, which is indistinct in the widefield image and barely gets resolved in Scheme-A, is well resolved after the use of Scheme-B. In Figure 5.6 (ii) (a-c), line plots of normalized intensity across closely spaced actin (ROI 1 in each image) show that fluorescence recovery has improved resolution, enabling the detection of filaments at 60 nm apart.

5.5.3 Photoinduced recovery with UV

We then perform photoinduced recovery using the external UV source. To proceed with the experiments, a sample slide of AF 647 labeled actin in U87MG cells is placed on the sample plane. Using the 638 nm laser as the excitation beam, we first

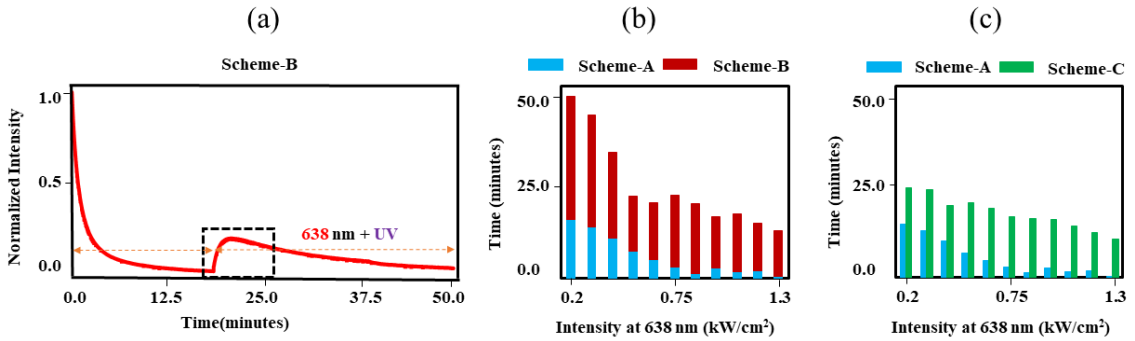

Figure 5.7: (a) The normalized fluorescence signal change over time under Scheme-B irradiation with a UV recovery beam. Bar plots illustration showing the time of the entire fluorescence signal as the 638 nm laser intensity rises from 0.2 kW/cm^2 to 1.3 kW/cm^2 under (b) Schemes A and B illumination and (c) Schemes A and C illumination, while utilizing the UV recovery beam.

implement the illumination Scheme-B and measure the period of the fluorescence signal. As displayed in Figure 5.7 (a), the switching of the 638 nm laser causes the fluorescence signal to spike first before progressively decaying to the background level. At this moment, the UV source is switched on to recover the fluorescence, which eventually fades into the background. We also measure the duration of the observed fluorescence blinking on the camera for each excitation intensity as it increases from 0.2 kW/cm^2 to 1.3 kW/cm ^{2} under Schemes A and B. According to the bar plot in Figure 5.7 (b), the duration of fluorescence blinking under Scheme-B (red color) is the longest at an excitation intensity of $\approx$ 0.2 kW / cm ^{2}. Additionally, we measure the total observed fluorescence time under Scheme-C (green color) at different levels of excitation intensity and compare them with Scheme-A (sky blue color), as shown in the bar diagram of Figure 5.7 (c). It is evident from Figures 5.7 (b) and (c) that the use of the UV recovery source yields similar results to those obtained with the 405 nm beam and Scheme B, thereby providing the maximum fluorescence duration. We then perform easySTORM imaging of a sample slide of AF 647 tagged actin in U87MG cells using the optimized scheme for fluorescence recovery. At first, an area of the sample slide is excited under Scheme-A and captures 5,800 image frames with noticeable blinking. The same area is subsequently illuminated with the optimized Scheme-B, resulting in the acquisition of a total of 17,000 imaging frames. Figures 5.8 (a) and (d) show the reconstructed super-resolved images (pseudo-colored in red) of the same sample area from these 5,800 and 17,000 frames, respectively. We then compare the resolution of the reconstructed images in

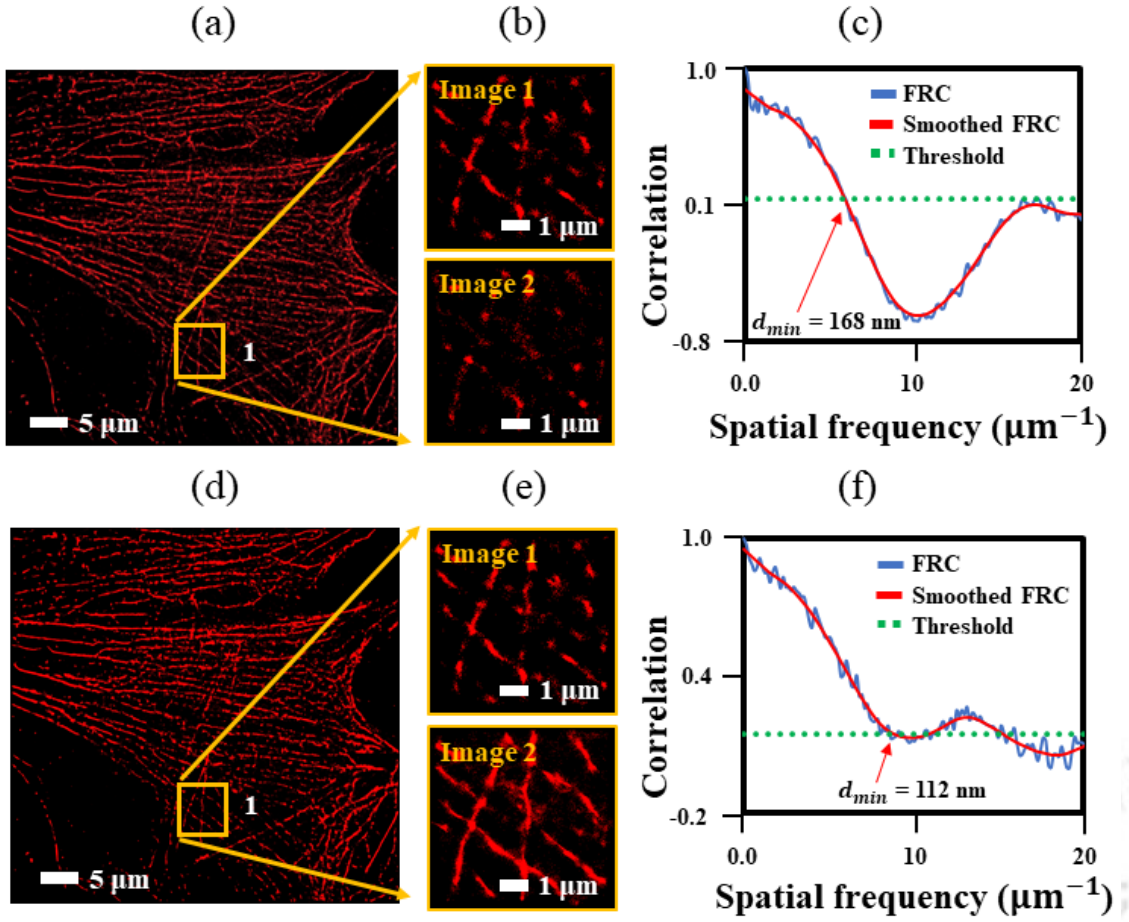

Figure 5.8: easySTORM reconstructed image of AF 647 labeled actin in U87MG cells (a) under Scheme-A illumination and (d) under Scheme-B illumination with an external UV source. Two super-resolved images, Image 1 and Image 2, are shown in (b) and (e). Each of these two is reconstructed by extracting separate image stacks for the regions designated as 1 in (a) and (d), respectively. The Fourier Ring Correlation method is used to determine image resolution for region 1 in (b) and (e) using correlation vs spatial frequency plots in (c) and (f), respectively.

Figures 5.8 (a) and (d), using the Fourier Ring Correlation (FRC) approach [87, 88]. As a requirement of the FRC analysis, at first, two distinct super-resolved images of region 1 in Figure 5.8 (a) are reconstructed by dividing the 5,800 image frames into two random stacks. The reconstructed images are shown as Image 1 and Image 2 in Figure 5.8 (b). By plotting correlation versus spatial frequency using the FRC plugin in Fiji-ImageJ (https://imagej.net/plugins/fourier-ring-correlation), the resolution at the cutoff spatial frequency is determined as shown in Figure 5.8 (c). The resolution is measured as the inverse of the cutoff frequency, where the FRC plot intersects the threshold line (1/7 of the correlation peak) [89]. A resolution of

d_{min} = 168 nm is obtained. We also reconstruct another two super-resolved images, shown as Image 1 and Image 2 in Figure 5.8 (e), from the same region 1 in Figure 5.8 (d), following the same steps and then repeating the FRC analysis. The plot in Figure 5.8 (f) indicates d_{min} = 112 nm, suggesting an improvement of 56 nm with Scheme-B. These results confirm that photoinduced fluorescence recovery of AF 647 fluorophores in Mowiol with β-ME can also be accomplished with an external UV source without the need for a separate laser and specialized optics required to deliver the recovery beam.

5.5.4 Spectroscopic studies to confirm photoinduced recovery effect

In Section 5.2.1, we discussed about excited fluorophores entering a dark state in the presence of a blinking reagent. To verify the dark state formation for AF 647 fluorophores in the presence of β-ME only, we carry out additional experiments. First, a specimen slide of Phalloidin-AF 647 in β-ME only is considered on the sample plane of the microscope. Utilizing the 405 nm recovery beam and the optimized settings for Scheme-B, the sample slide is illuminated. As seen from the plot in Figure 5.9 (a) of net fluorescence intensity (along with blinking) as a function of time, after $\approx$ 5 minutes of 638 nm excitation of the sample, the fluorescence signal drops to the background level. However, upon application of the 405 nm recovery beam, the blinking duration increases by an extra 5 minutes. Another specimen slide that has Phalloidin-AF 647 in β-ME alone is also illuminated under Scheme-B using the UV source. As seen in Figure 5.9 (b), switching the UV lamp on after the fluorescence decays on 638 nm excitation causes the fluorescence blinking to recover and lasts for $\approx$ 12 minutes, which is limited to $\approx$ 5 minutes without the UV beam.

For the second experiment, we prepare another slide containing Phalloidin-AF 647 in β-ME only and record the absorption spectra using a UV-VIS-NIR spectrophotometer (Lambda 950, Perkin Elmer). The recorded absorption spectrum against wavelength is shown in Figure 5.9 (c). After irradiating the same slide with the 638 nm laser at 0.5 kW/cm^2 for roughly 5 minutes, we again record the absorption spectrum (i.e., the red curve). Following irradiation with 638 nm, it is noticed that the absorption peak at 638 nm falls and a new peak appears at around 400 nm. This observation is in line with the previous reports observed with AF 488 and the cyanine dyes [21, 34, 35]. Our spectroscopic analysis hints at the formation of the

dark state of AF 647 in β-ME under 638 nm excitation. It also indicates that the enhancement in the photoswitching of AF 647 is due to the dye itself in presence of the blinking reagent as the molecule undergoes the $E_o \rightarrow E_1 \rightarrow T \rightarrow D \rightarrow D* \rightarrow E_o$ cycle, as discussed in Section 5.2.1 and is independent of the buffer medium or biological structure.

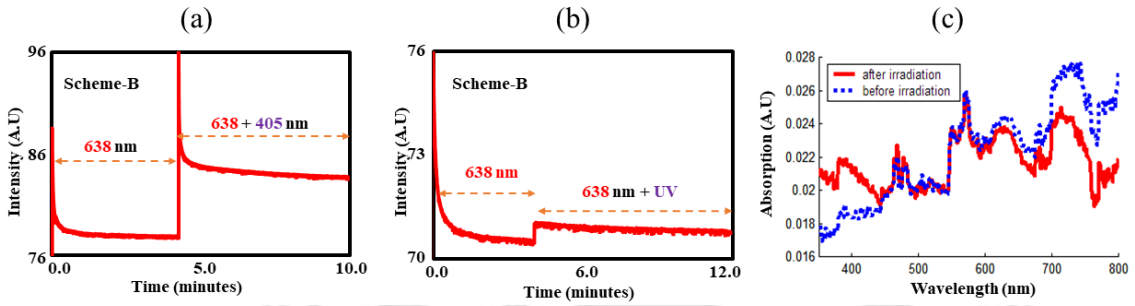

Figure 5.9: Plots of fluorescence emission during blinking of Phalloidin conjugated-AF 647 dye in β-ME alone, from a microscope slide, with optimized parameters using (a) Scheme-B with a recovery beam at 405 nm and (b) Scheme-B with a recovery beam from an external UV lamp. (c) Phalloidin-AF 647 dye absorption spectra in β-ME alone, both before and after 638 nm laser irradiation.

5.5.5 Comparing cytoskeletal structures in human stem and cancer cells utilizing easySTORM

Following the optimization of photoinduced recovery and excitation intensities, the optimized parameters (Scheme-B) are subsequently applied to image cytoskeletal structures for comparison of their widths in human stem and cancer cells.

Comparison of actin widths in MSCs, U87MG cells and MDA MB 231 cells

In the first experiment, we compare the width of actin present in specimen slides of MSCs, U87MG, and MDA MB 231 cells. Figures 5.10 (i) (a-c) show the wide-field fluorescence images (pseudo-colored in red hot) of actin from different FOVs corresponding to specimen slides of MSCs, U87MG cells, and MDA MB 231 cells, respectively. Figures 5.10 (ii) (a-c) display the respective STORM images (pseudo-colored in red hot). The intensity line plots across the ROIs 1, 2, and 3 in the widefield and their corresponding reconstructed images are shown in the Figures 5.10 (iii) (a-c), respectively. The FWHM measurements obtained from these line

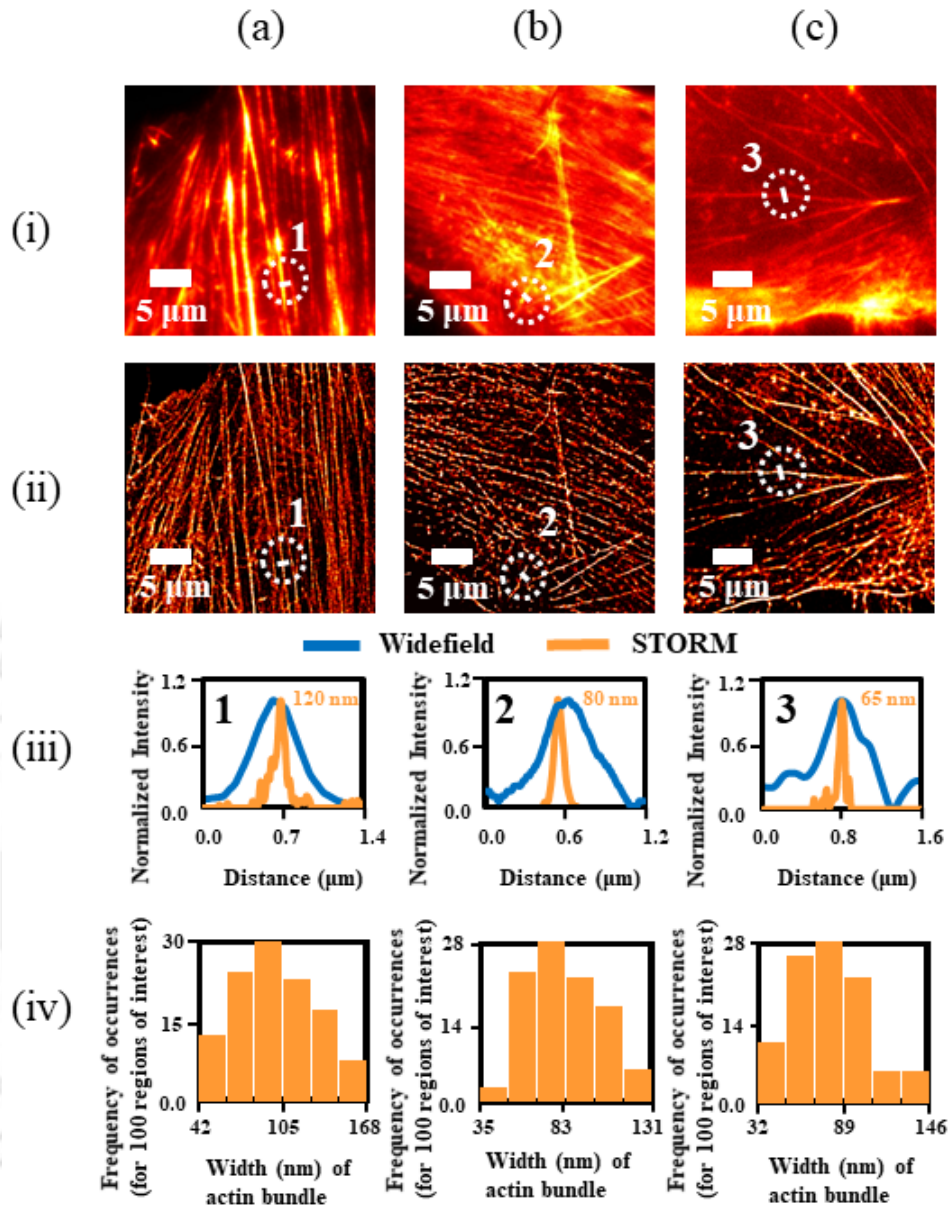

Figure 5.10: Results for actin in MSCs, U87MG, and MDA MB 231 cells are shown in columns (a), (b), and (c), respectively. The widefield images are displayed in (i), while the associated super-resolved images obtained using easySTORM are shown in (ii). The combined intensity line plots from regions of interest 1, 2, and 3 chosen from both widefield and STORM images of actin are shown in (iii), where the orange plot denotes STORM and the blue plot denotes widefield. (iv) displays histogram plots that show the frequency distribution of actin widths in each easySTORM image, based on 100 selected regions per image. Measured values are in mean±SD. SD corresponds to standard deviation.

plots indicate that the ROIs 1, 2, and 3 in the STORM images exhibit widths of 120 nm, 80 nm, and 65 nm, respectively. In contrast, the actin is not distinctly resolved

in the corresponding widefield images. To gain further insights, 100 randomly selected ROIs from Figures 5.10 (i) (a-c) are analyzed. Based on the FWHM data, the average actin width in these ROIs is found to vary between 300 and 700 nm. Analysis of the corresponding ROIs in their respective STORM images in Figures 5.10 (ii) (a-c), reveals a substantial improvement in resolution, with average actin widths estimated to be 101±30 nm for MSCs, 81±20 nm for U87MG cells, and 77±23 nm for MDA MB 231 cells. The width distributions obtained from the STORM measurements are presented as histograms in Figures 5.10 (iv) (a-c), revealing the frequency of occurrences as a function of the widths. For MSCs, U87MG and MDA MB 231 cells, the frequently occurring actin widths are between 84-105 nm, 67-83 nm, and 70-89 nm, respectively. These results suggest that the actin in MSCs is significantly thicker than that of the U87MG and MDA MB 231 cells. From the FWHM study, the minimum actin widths for MSCs, U87MG, and MDA MB 231 cells are found to be approximately 42 nm, 35 nm, and 32 nm, respectively. Additionally, we observe that actin width does not significantly differ across individual cells of the same kind, as per STORM measurements taken across 5–10 cells per cell type. This implies that there is low structural heterogeneity within each cell type, while clear differences are evident between cell types. Besides, it has already been demonstrated with electron microscopy that actin filaments aggregate using special binding proteins, with each aggregation or group containing anywhere from a few to thousands of filaments within a cell [90]. Studies with electron microscopy have also revealed that the cross-sectional diameter of a single actin filament is approximately 7 nm [91]. Our results using easySTORM imaging indicate that the different groups of actin filaments are likely to be accountable for the varying width of actin (actin bundles) as seen in MSCs, U87MG, and MDA MB 231 cells. Moreover, cryo-electron microscopy has shown that, depending on the kind of binding protein and the filament structural organization, the distance between two parallel actin filaments can vary from 11 to 36 nm [90]. By utilizing these interspacing data and width estimations from our easySTORM, we find that each actin bundle in MSCs has roughly 3-6 filaments. In contrast, bundles in U87MG and MDA MB 231 cells have approximately 2–5 filaments. These measurements highlight the variability in actin organization in terms of the thicknesses among the above cell types as observed in STORM imaging.

5.6 Summary

We present a comprehensive experimental investigation of the photoinduced recovery mechanism in fluorescence and blinking behavior of excited AF 647 fluorophores during their dark state formation in Mowiol with β-mercaptoethanol, utilizing the modular easySTORM microscope. The experiments involve the use of different illumination schemes, utilizing a 638 nm laser excitation and a 405 nm laser or a UV source as the recovery beam. It has been observed that, using the optimized illumination parameters, significant extension in fluorescence duration and blinking can be achieved, resulting in a higher number of imaging frames and subsequent increase in single molecule localization accuracy. This improvement significantly enhances the resolution, enabling the observation of closely spaced actin filaments in brain cancer cells (U87MG) that are otherwise indistinguishable using conventional illumination in STORM. Further, we observe that utilizing the low-cost handheld UV source as the recovery beam reduces the system complexity and cost, while maintaining comparable performance to a 405 nm laser.

* * *

Chapter 6

Dynamic modulation of illumination in STORM and Combining STORM with beam scanning microscopes

6.1 Introduction

In STORM, the beam optics determines the extent of the illumination, which typically follows a Gaussian intensity profile. This limits precise control and modification of the spatial extent of excitation in the sample plane. As a result, regions outside the intended region of interest (ROI) may get illuminated. Since STORM requires high excitation intensities and prolonged illumination, any unintentionally exposed regions outside the user-defined ROI will not be available for future STORM imaging due to photobleaching of the fluorophores. Existing approaches, such as placing apertures conjugate to the sample plane, can restrict the illumination area but are limited to fixed profiles and lack the flexibility to generate arbitrary or user-defined dynamically modulated patterns [92]. Moreover, the existing illumination approach in STORM prevents differential intensity control across multiple regions, within a field of view (FOV), with varying fluorophore densities, resulting in fast photobleaching of sparsely labeled areas compared to the dense areas. As mentioned earlier, STORM imaging is associated with the blinking behavior of fluorophores, which must be adequate to reconstruct the super-resolved image. Failure to meet this condition will result in only a widefield fluorescence image. For such a sample, it may be possible to acquire a high-resolution image using beam scanning techniques such as confocal or image scanning microscopy (ISM); however, ensuring exactly the same ROI is not possible, unless the STORM setup and the scanning microscope share the same sample stage and objective lens. Spatially modulated light has

been used in multiple microscopy techniques [7, 93, 94, 95], although its integration with widefield single molecule localization microscopy, like STORM, remains unexplored. In this Chapter, we introduce a novel programmable illumination method to control the spatial extent and intensity of the illumination area in the sample plane by employing a liquid crystal spatial light modulator (LCSLM) based assembly in the excitation beam path. This enables spatial modulation of light [92], thus controlling the position, shape, and intensity of the illumination patch. We name the new STORM imaging scheme as piSTORM (i.e. programmable illumination in STORM) [81]. In this Chapter, we also demonstrate another novel imaging approach that combines excitation beams from STORM and beam scanning techniques and is directed towards a single objective lens and sample stage.

6.2 Programmable control of the illumination beam profile

To create programmable illumination patterns on the sample plane of the microscope, we holographically modulate the complex amplitude of the light beam on the hologram plane in the excitation path, which is made optically conjugate to the sample plane of the microscope. Below, we first describe the theory behind programmable illumination control and its implementation in the openFrame-based modular microscope.

6.2.1 Holographic modulation of the light beam

Let $A_n(x,y)e^{i\alpha(x,y)}$, where (x,y) denote the transverse coordinates in the hologram plane, be the complex amplitude profile of the illumination beam to be generated. Here, $A_n(x,y)$ takes values in the range [0,1] and $\alpha(x,y)$ represents the overall phase. We utilize a computer generated holography technique [92, 96] to achieve the generation of a user-defined complex amplitude profile. The transmittance (or reflectance) value of the binary hologram ($T_h(x,y)$) can be obtained as,

$$T_h(x,y) = \begin{cases} 1, & \text{if } \alpha(x,y) < \frac{\pi}{2} \text{ and } r_n(x,y) < A_n(x,y) \\ 0, & \text{if } \alpha(x,y) \geq \frac{\pi}{2} \end{cases} \tag{6.1}$$

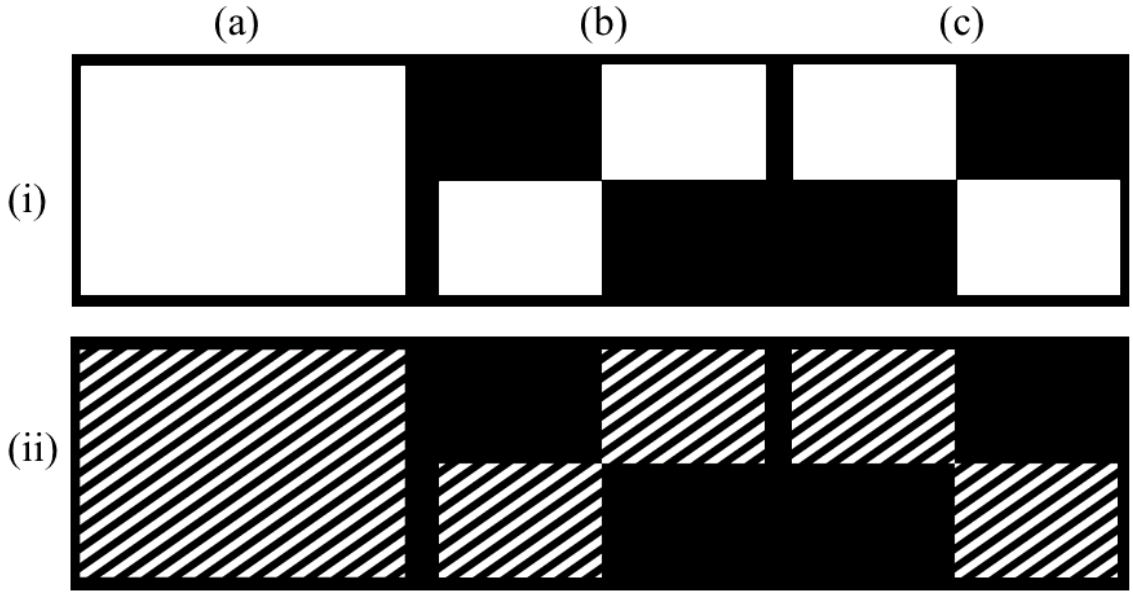

Figure 6.1: (i) (a-c) display the expected illumination patterns and (ii) shows the typical binary holograms corresponding to (i) (a-c), which, on illumination with a laser beam, should give rise to diffracted orders carrying the information of the illumination patterns (i) (a-c).

In the above, $r_n(x, y)$ represents a uniform random number with values in the range [0,1], which is generated independently at each coordinate (x, y) of the hologram plane. The phase term is defined as $\alpha(x, y) = m_x x + m_y y$, with (m_x, m_y) representing X and Y tilts of the generated beam. The binary hologram T_h thus computed can be sent to the LCSLM display panel. When the LCSLM displaying the binary hologram is illuminated with a collimated laser beam, (+1, 0 and -1) diffraction orders are produced. The angular position of the +1 diffraction order depends on the values (m_x, m_y) that can be adjusted in real time using the computer interface, allowing dynamic beam steering. By selecting appropriate values of (m_x, m_y), the +1 order beam can be focused at the center of an iris diaphragm, which blocks the other two orders, thereby isolating the one order beam. The +1 order beam, representing the illumination beam, is then relayed on to the sample plane of the microscope to result in an intensity profile, $I_n(\zeta, \eta) = |A_n(\zeta, \eta)|^2$, where $(\zeta, \eta) = (Mx, My)$ and M is the demagnification factor between the LCSLM plane and the sample plane.

We demonstrate the computation of user-defined binary holograms, to generate three different illumination beam patterns, as shown in Figures 6.1 (i) (a-c), where the white portion has $I_n = 1$, and the dark portion has $I_n = 0$. The typical binary holograms to create such illumination beam patterns are shown in Figures 6.1 (ii)

(a-c).

6.2.2 Experimental arrangement

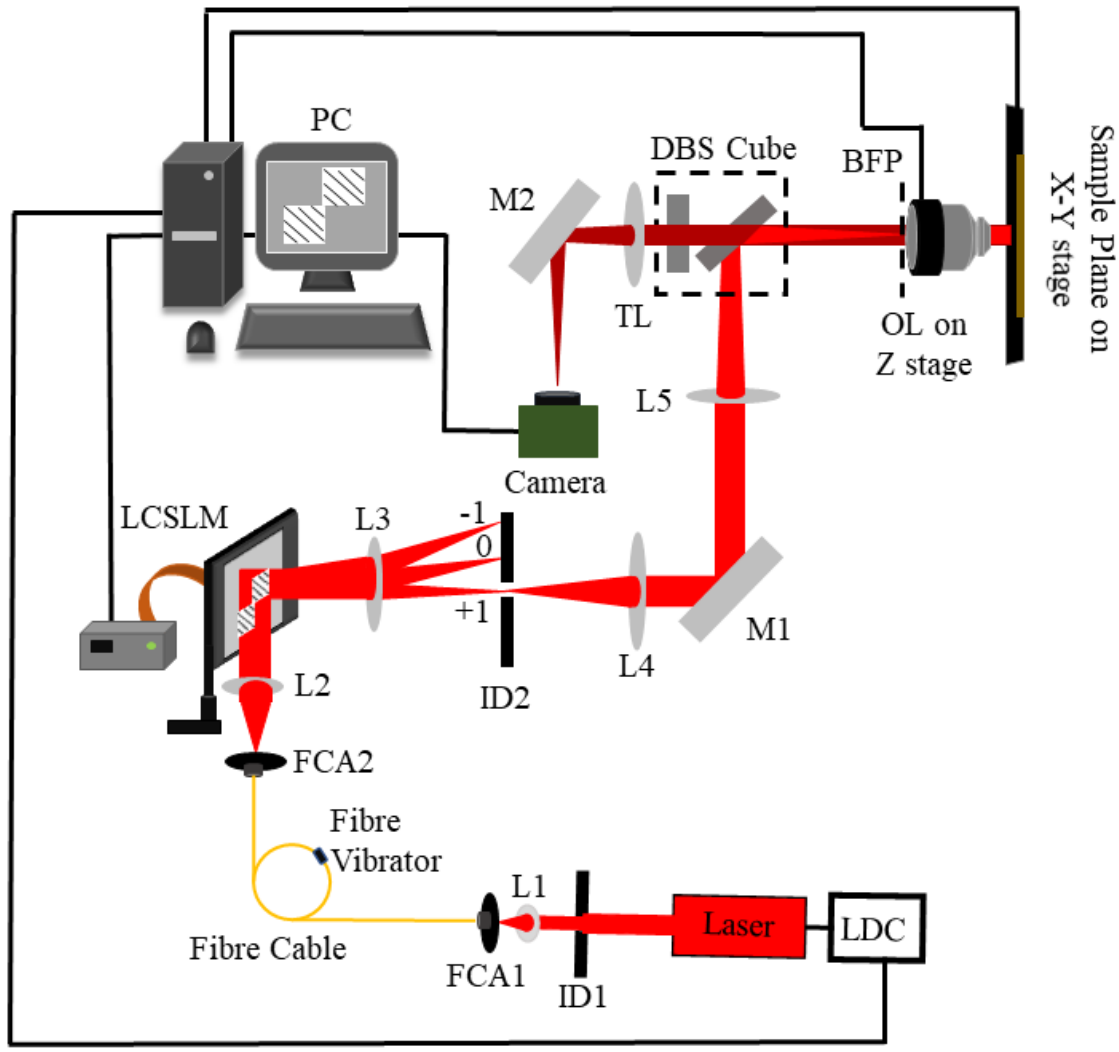

Figure 6.2: Schematic of the experimental setup. The hologram displayed on the LCSLM panel diffracts the excitation beam in different orders, of which the +1 order is isolated and relayed to the sample plane. The +1 order beam carries information on the user-specified illumination pattern.

The schematic of the experimental arrangement is shown in Figure 6.2. To excite the sample, the 638 nm multimode diode laser is used. The lens L2 collimates the emergent beam from the fibre coupler adapter FCA2 to be incident on an LCSLM (LC-R 720, HOLOEYE) display consisting of 1280×768 pixels. The LCSLM is connected to a PC, where the binary hologram is computed. After being incident

on the hologram, the beam diffracts into 0, -1, and +1 orders. Lens L3 focuses these diffraction orders onto the iris diaphragm, ID2, which allows only the +1 order beam to pass through, towards lens L4 to be incident on the microscope objective lens (OL) (UPlanSApo, 1.40 NA, 100x oil immersion, Olympus). Lens pairs (L3, L4) and (L5, OL) are arranged in such a way as to make the LCSLM and sample planes optically conjugate. The imaging part of the microscope remains unchanged and the same as earlier Chapters. We observe that the excitation intensity in our arrangement has been reduced to ≈ 6 % after the LCSLM assembly, primarily due to the overall effects of limited diffraction efficiency of the binary hologram and optical losses. One can instead use a blazed grating hologram to raise efficiency $\geq$ 10 times. Additionally, there are low-cost high power (≈ 8 W) compact diode lasers available or fluorophores such as iFluor 647 that require very low excitation power [44], and can be used to compensate for these losses. To be noted, the LCSLM display supports real-time update of the hologram at a rate of at least 30 fps. The hologram display can be synchronized with the camera acquisition to enable real-time hologram updates or toggling between multiple illumination patterns during image capture.

6.2.3 Image acquisition and reconstruction

To record widefield fluorescence images, illumination intensities in the range 1–5 W/cm^2 at 638 nm are maintained on the sample plane. For STORM image acquisition of the same regions, the excitation intensity is subsequently increased to activate fluorophore blinking and is maintained in the range of 150–200 W/cm^2 on the sample plane. For super-resolved image reconstruction, approximately 20,000 image frames are acquired using the camera at a rate of 30 fps for each region under an illumination pattern. The image reconstruction and analysis are performed, following the same reconstruction parameters and procedures described in Chapter 4.

6.2.4 Sample preparation for programmable illumination

At first, we utilize a fluorescent slide (92001, autofluorescent plastic slide, Chroma technology) as the sample for the proof of concept programmable illumination. To demonstrate piSTORM, we prepare samples of carboxyl QDs and AF 647 labeled actin and tubulin of U87MG cells, following similar protocols, as in Chapter 4.

6.3 Results and discussions

6.3.1 Programmable illumination in autofluorescent glass slide

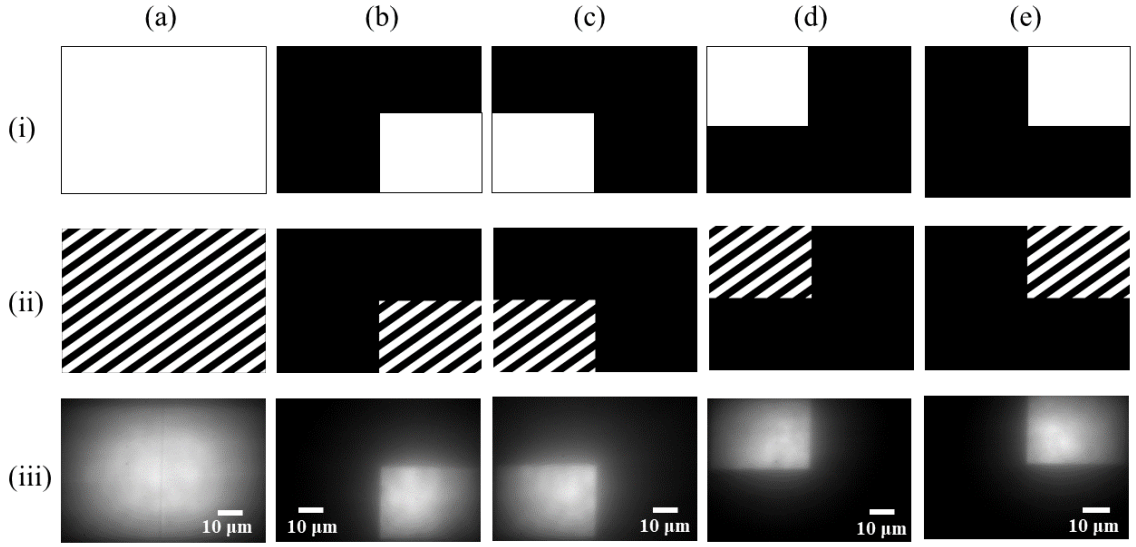

Figure 6.3: (i) (a-e) display the expected or ideal illumination patterns to illuminate the sample plane and (ii) (a-e) show the typical binary holograms that are utilized to create these patterns on the sample plane. (iii) (a-e) are the fluorescence images captured on the camera, due to the illumination of a fluorescent slide on the sample plane, using the patterns (i) (a-e), respectively.

For programmable illumination in the sample plane of the microscope, we first generate five user-defined illumination patterns. The intended patterns are seen in Figures 6.3 (i) (a-e), while Figures 6.3 (ii) (a-e) show the typical binary holograms that generate these patterns. Figures 6.3 (iii) (a-e) show the observed fluorescence emitted from an area on the autofluorescent slide on the sample plane, when illuminated with the patterns. The results demonstrate that we are able to generate a dynamic and user-specified illumination pattern in the sample plane of the openFrame modular microscope.

6.3.2 piSTORM of QDs

To demonstrate piSTORM with user-defined illumination patterns, we consider the specimen slide of QDs on the sample plane of the microscope. We employ two distinct illumination patterns (comprising diagonally opposite quadrants) on a specific

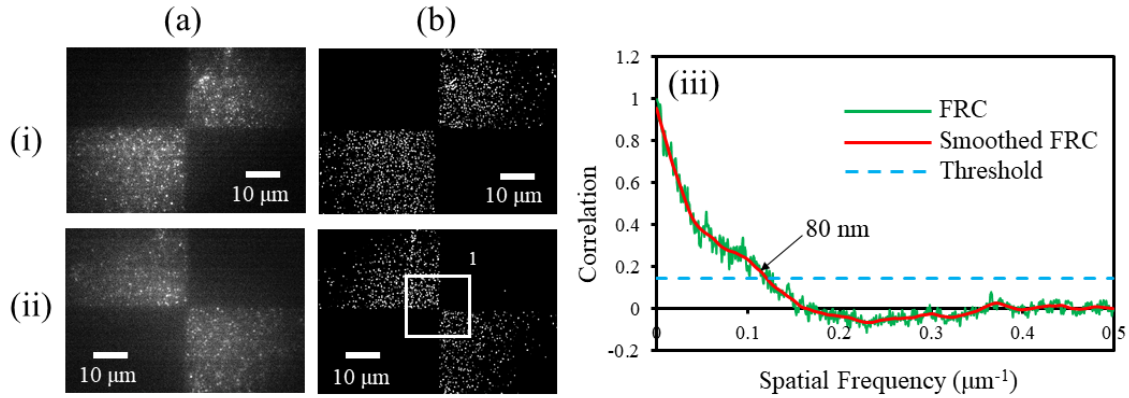

Figure 6.4: (i) and (ii) (a) are widefield images of quantum dots using two user-defined illumination patterns at two different instants. The corresponding reconstructed STORM images are shown in (i) and (ii) (b). (iii) denotes the correlation against the spatial frequency plot to estimate the resolution using the FRC method in region 1 of (ii) (b).

FOV on the sample plane. Initially, we capture a widefield image as shown in Figure 6.4 (i) (a) with one illumination pattern, followed by acquisition of image frames for STORM. The reconstructed super-resolved image is shown in Figure 6.4 (i) (b). After the imaging with the first illumination pattern is completed, the second illumination pattern is employed as shown in Figure 6.4 (ii) (a), and STORM acquisition is carried out to reconstruct the super-resolved image as shown in Figure 6.4 (ii) (b). Subsequently, the resolution of region 1 in Figure 6.4 (ii) (b) is quantified by employing the Fourier Ring Correlation (FRC) approach as described in Chapter 5. The corresponding correlation versus spatial frequency plot, shown in Figure 6.4 (iii), yields a resolution of $\approx$ 80 nm. We also estimate the mean localization precision to be around 7 nm, following the procedure as mentioned in the Chapter 4.

6.3.3 piSTORM of actin in U87MG cells

As an additional proof of concept, we perform programmable illumination in STORM to image Phalloidin-AF 647 labeled actin in U87MG cells. First, a particular FOV is chosen containing actin, and similar illumination patterns are employed as used for the quantum dots in Section 6.3.2. Figures 6.5 (i) and (ii) (a) show the widefield images (pseudo-colored in red) of actin for each illumination pattern, while Figures 6.5 (i) and (ii) (b) display the corresponding super-resolved images (pseudo-colored in red) using STORM. From Figures 6.5 (i) (a) and (b), we consider region 1 and

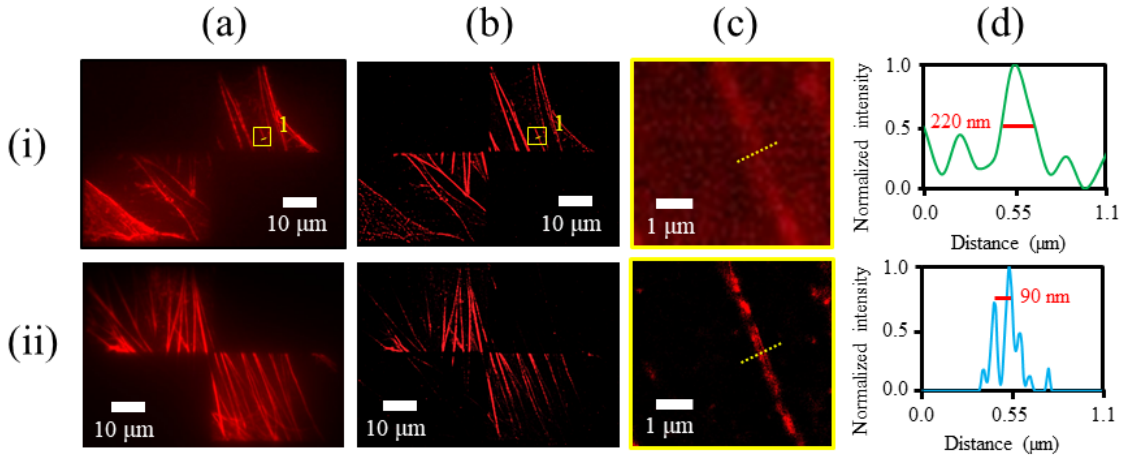

Figure 6.5: (i) and (ii) (a) are two widefield images from a field of view on a microscope slide, containing AF 647 labeled actin in U87MG cells, illuminated with two opposite quadrant patterns, and (i) and (ii) (b) are the respective super-resolved reconstructed images. (i) and (ii) (c) are the magnified views of region 1 in (i) (a) and (b), respectively. (i) and (ii) (d) are the intensity line plots of region 1 chosen in (i) and (ii) (c), respectively.

display its magnified views in Figures 6.5 (i) and (ii) (c), respectively. Figures 6.5 (i) and (ii) (d) show the intensity line plots across the regions marked in yellow in Figures 6.5 (i) and (ii) (c), respectively. The line plots show that the structures are getting resolved with a separation of about 90 nm in the super-resolved image, which remain unresolved in the widefield image. The single molecule localization precision is found to be $\approx$ 5 nm.

6.3.4 piSTORM to image random actin structures in U87MG cells

One key objective of piSTORM is to have STORM imaging with random illumination patterns. To realize this, we consider a sample slide of AF 647 labeled actin in U87MG cells. As seen in Figure 6.6 (a), first, a widefield image (pseudo-colored in red) of the full FOV is captured on the camera. The arbitrary illumination beam profile I_n is first computed, based on the widefield image pixel value distribution. Specifically, $I_n(\zeta, \eta)$=1 if the location (ζ, η) in the widefield image has a pixel value greater than a threshold and $I_n(\zeta, \eta)$=0 otherwise. The computed illumination pattern is seen in Figure 6.6 (b). Following the generation of the thresholded pattern, the binary hologram is calculated and loaded onto the LCSLM. A typical binary hologram of that pattern is shown in Figure 6.6 (c). The illumination pattern now

ensures that only the designated ROIs on the sample will be excited, excluding other regions, as seen in the widefield image in the Figure 6.6 (d). The image acquisition for STORM is carried out in the same ROI using the same illumination pattern. The corresponding super-resolved image (pseudo-colored in red) is seen in Figure 6.6 (e). Figure 6.6 (f) presents the intensity line plots through the ROI 1 chosen in the widefield and respective reconstructed images. As observed in these line plots, the super-resolved image helps to visualize two closely spaced actin separated by $\approx$ 68 nm, which is not getting resolved in the widefield image. We compute the localization precision in the reconstructed image as $\approx$ 5 nm. The experiments presented so far show that dynamic, programmable illumination enables selective STORM imaging of different regions within the same field of view at different times. This approach offers improved control over excitation, minimizes unnecessary photobleaching, and enhances fluorophore localization during super-resolution imaging.

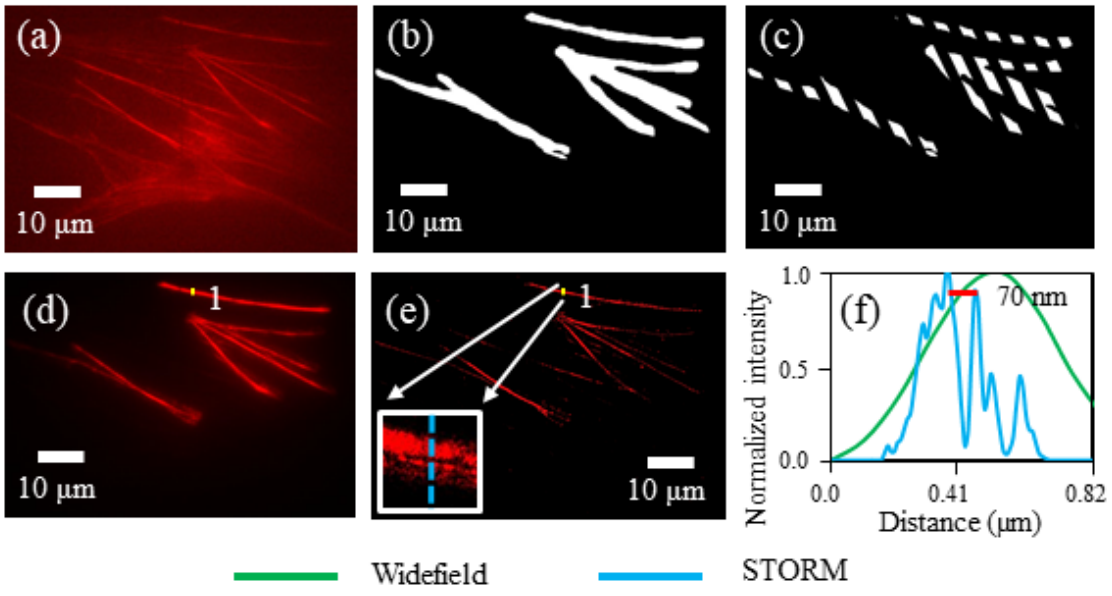

Figure 6.6: (a) Widefield image of Phalloidin-AF 647 labeled actin in U87MG cells under full-field illumination. The intended illumination pattern obtained by thresholding the image (a) is displayed in (b). A typical binary hologram that can generate the pattern (b) is shown in (c). (d) is the widefield image of the same sample area after excitation with the illumination pattern (b), and (e) is the respective reconstructed super-resolved image. Intensity line plots of the same region of interest 1 chosen in (d) and (e) are shown in (f). Inset in (e) shows the magnified view of the region of interest 1.

6.3.5 piSTORM with differential illumination intensity to image tubulin of U87MG cells

To demonstrate differential or variable intensity illumination utilizing programmable illumination in STORM, AF 647 immunolabeled tubulin in U87MG cells is imaged. We follow the same procedure as described earlier for generating the selective illu-

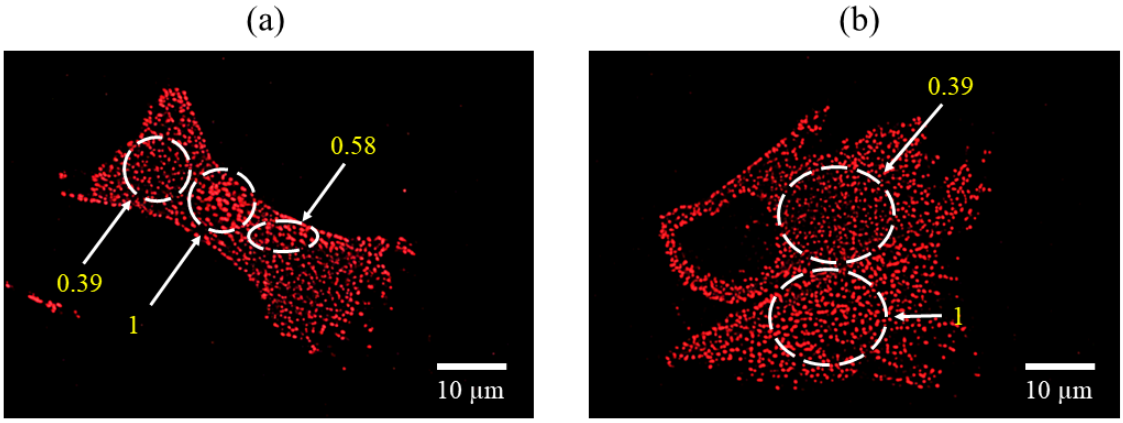

Figure 6.7: (a) and (b) are two different fields of view (FOVs) showing the STORM images of AF 647 labeled tubulin from a sample slide of U87MG cells, reconstructed from $\approx$ 20,000 images acquired separately for each FOV, under simultaneous excitation with multiple intensities in each FOV. The real numbers 0.39, 0.58, and 1, inside the designated white-dotted regions in (a) and (b), denote the normalized pixel values, corresponding to different levels of intensity in the illumination beam.

mination patterns, except for the thresholding step. Here, the illumination beam profile I_n is computed based on a widefield image such that $0 \leq I_n(\zeta, \eta) \leq 1$. The reconstructed images (pseudo-colored in red) are seen in Figures 6.7 (a) and (b). The white-circled regions in the images, indicated by real numbers 0.39, 0.58, and 1, denote the normalized pixel values that correspond to different excitation levels within the illumination beam, with a larger pixel value indicating a higher excitation intensity. Thus, the variable intensity illumination allows simultaneous excitation of different regions, with different intensity levels.

6.4 Combining STORM and beam scanning microscopy

To obtain super-resolved as well as high-resolution images of the same sample region, we combine the illumination beams for STORM and the beam scanning microscope

(confocal and ISM) in the excitation path of a single optical microscope (IX51, Olympus), as shown in Figure 6.8. For illumination in STORM and beam scanning microscope, we utilize the 638 nm laser and the 462 nm laser, respectively. The emergent beam from the FCA output is collimated by the lens L1, towards the dichroic beam splitter DBS1. The DBS1 is a long pass dichroic that reflects wavelengths below 532 nm and transmits above this wavelength. Hence, the 462 nm beam (shown in blue) is reflected by the DBS1, while the 638 nm wavelength (shown in red) passes through it.

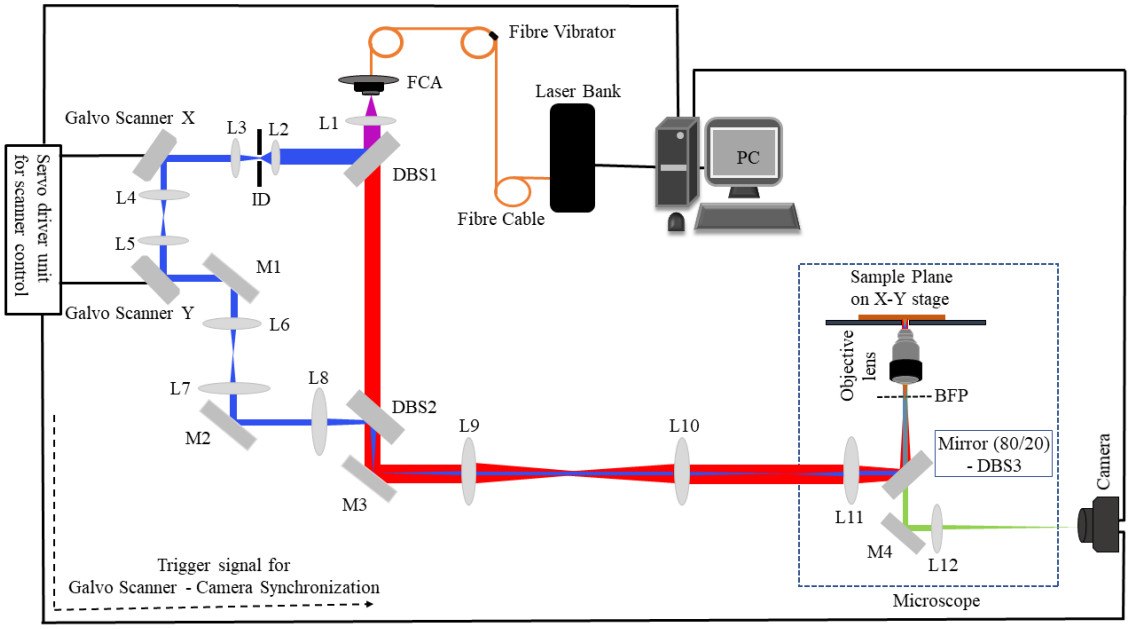

Figure 6.8: A schematic of the experimental setup to combine the illumination beam paths of STORM and beam scanning (confocal and image scanning) microscopes in a single microscope stage. Red and Blue indicate the path of illumination for STORM and beam scanning, respectively.

6.4.1 Implementation of beam scanning

At first, we implement the beam scanning technique by switching on the 462 nm laser. As shown in Figure 6.8, the 462 nm beam after being reflected by the DBS1 is focused by the lens L2 onto the iris diaphragm (ID), which is at the focus of another lens L3. L3 hence collimates the beam towards the beam scanning unit, which comprises the Galvo Scanner X (6231H, Cambridge Technology), lens pairs (L4, L5), and the Galvo Scanner Y (6231H, Cambridge Technology). The beam after the Scanner Y travels towards the lens L8, after passing through the combination of

mirror M1, lens pairs (L6, L7), and mirror M2. L8 focuses the 462 nm beam towards the mirror M3, after reflection at the DBS2, which has the same specification as DBS1. M1, M2, and M3 are kinematic mirrors that allow precise X-Y control of the beam on the sample stage of the microscope. The combination of the lenses L9-L11 and the Mirror (80/20) produces a uniform illumination at the back focal plane (BFP) of the microscope. The Mirror (80/20) reflects 80% of the illumination beam towards the sample plane and transmits 20% through it. The beam at BFP is focused by the objective lens (UPlanSApo, 1.40 NA, 100x oil immersion, Olympus) to create an illumination spot on the sample plane. For a reflecting sample, such as the 1951 USAF test resolution target, the reflected signal from the sample is collected by the objective and transmitted through the Mirror (80/20) towards another mirror M4. M4 reflects the beam towards the lens L12, which then focuses the light onto the camera. For the fluorescent sample, the Mirror (80/20) is replaced by the dichroic DBS3, which is the same DBS cube as mentioned in Chapter 3. The Mirror (80/20) and DBS3 are held in a rotating turret, making it easy to switch their positions.

For image capture in both reflection and fluorescence modes, we use a USB 3.0 CMOS Camera (DCC3240C, Thorlabs) with a sensor area of 1280×1024 pixels and each camera pixel having a size $\approx$ 5.3 μm. The rotations of the X and Y Galvo Scanners are controlled by the servo driver unit via a program written in LabVIEW on the PC. The same LabVIEW program also controls the image capture by the camera. An appropriate trigger signal derived from the servo driver unit is used to synchronize the Scanner's movement with the camera image capture. The trigger signal ensures that once the program is instructed to run, for each scanned position of the beam over the sample, the camera captures an image of that position only. Thus, if the beam scans an area over M×N positions of the sample plane, then the camera captures M×N images of the beam corresponding to those positions.

6.4.2 Reconstruction of images in the beam scanning microscopy

Figure 6.9 (a) shows one out of the M×N images of the beam on the camera. To implement confocal microscopy, we use a suitable algorithm to select a window of P×Q pixels centered around the beam in the image, as shown in Figure 6.9 (b), and the sum of the total of the image pixels is stored. The window thus plays the role of the physical pin hole in front of the detector, as present in a conventional confocal

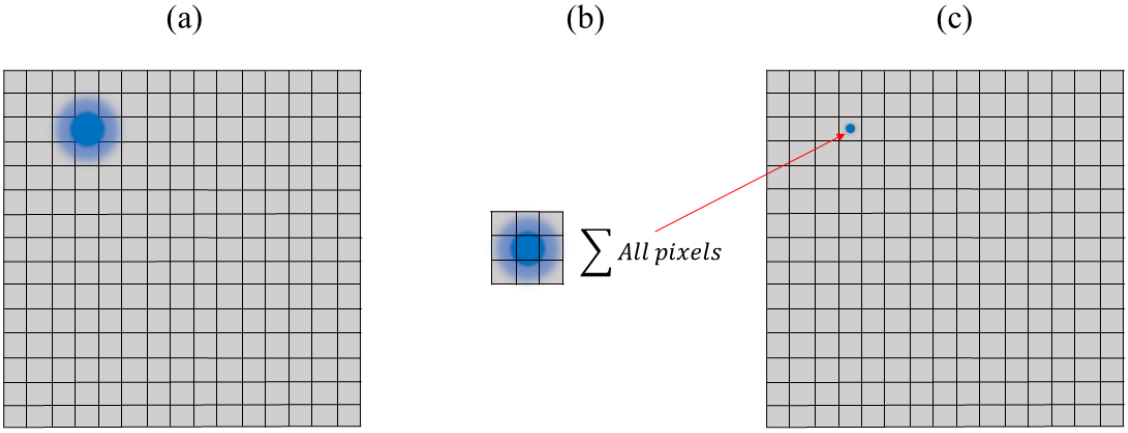

Figure 6.9: Schematic in (a) is the image of the illumination spot corresponding to a given scan position of the beam on the sample plane. (b) A small window of P×Q pixels surrounding the beam centre is extracted from (a). The summation of the pixel values in the window gives the confocal signal for the respective scan position and is accordingly assigned to the reconstructed image array as seen in (c).

microscope. The process is repeated for each scan position, and at the end of the scanning, the stored values over an array of M×N pixels are used to reconstruct the confocal image as shown in Figure 6.9 (c). To reconstruct the ISM image from the same M×N images as in Figure 6.9 (a), we perform pixel binning and a reassignment procedure for each scan position, as discussed in Chapter 2.

6.4.3 Implementation of the combined STORM-beam scanning microscope

To demonstrate STORM and beam scanning together, we enable the fluorescence mode with the DBS3. First, the beam scanning is performed on a region of a fluorescent sample using the 462 nm beam. Once the beam scanning is over, the 462 nm is switched off, and the 638 nm laser is switched on for widefield and STORM. The collimated 638 nm beam after L1 passes through the DBS1 and reaches the DBS2. The beam after DBS2 is reflected by M3 and focused onto the BFP of the objective lens after passing through the combination of lenses L9-L11 and being reflected by DBS3. This combination produces a uniform illumination on the sample plane after the beam passes through the objective lens. The emission from the sample is then collected by the objective, and after traveling through the combination of DBS3, M4, and lens L12 gets focused on the camera. The widefield image of an area on the sample is acquired with an intensity ≈ 0.03 kW/cm^2 on the sample plane, while

the intensity is increased to ≈ 0.5 kW/cm^2 during image acquisition for STORM.

6.4.4 Sample preparation for combined STORM-beam scanning

For beam scanning microscopy in the reflection mode, we use the 1951 USAF test resolution target as the sample. To realize the combined STORM and beam scanning microscopy in the fluorescence mode, we prepare microscope sample slides of carboxyl QDs obtained by diluting the stock solution in deionized water in the ratio of 1:12000 v/v.

6.4.5 Results

Beam Scanning in reflection mode

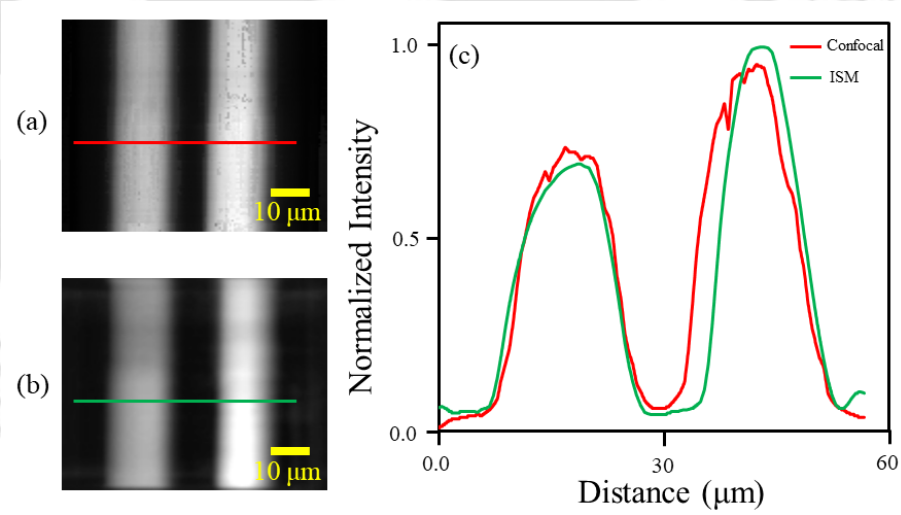

Figure 6.10: (a) and (b) are the confocal and image scanning microscopy (ISM) images, respectively, from a portion of the G5E2 strips in the 1951 USAF resolution test target on the sample plane, imaged in the reflection mode with the 462 nm beam. (c) The intensity line plots across the region marked as red and green in (a) and (b), respectively. The images are reconstructed from 100×128 scanned positions.

We use beam scanning microscopy in the reflection mode to image a portion of the group 5, element 2 (G5E2) strips of the 1951 USAF resolution test target kept on the sample plane. Scanning is performed over 100×128 positions. The confocal and ISM images are accordingly constructed and shown in Figures 6.10 (a) and (b),

respectively. The intensity line plots across the regions marked in red and yellow in Figure 6.10 (a) and (b), respectively, are shown in Figure 6.10 (c).

Combined STORM-Beam Scanning microscopy in the fluorescence mode

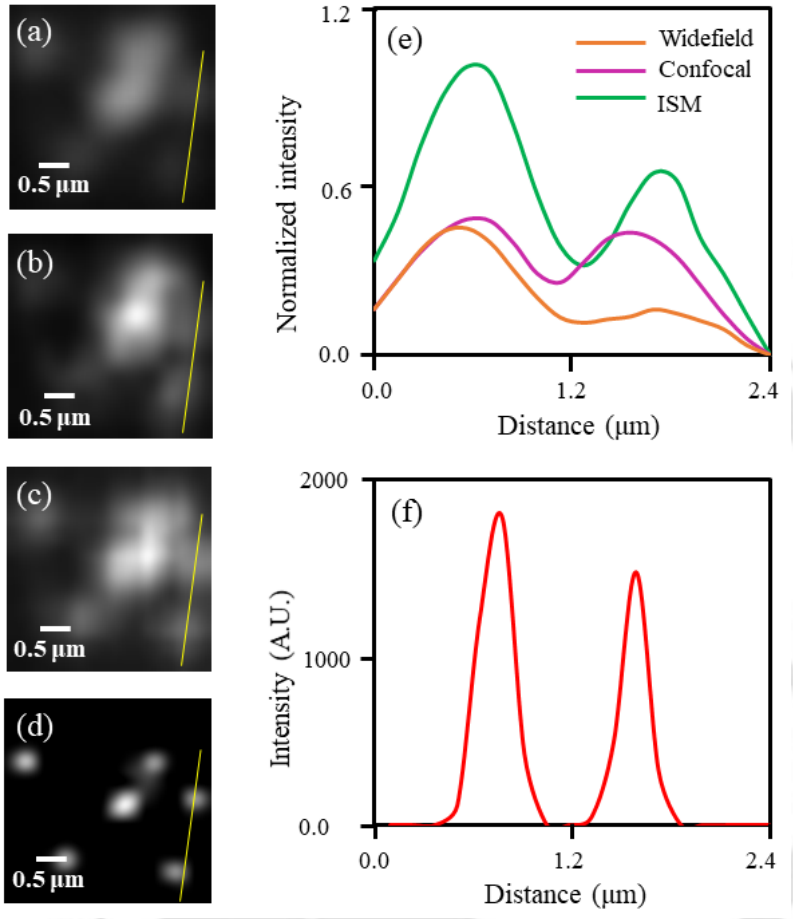

Figure 6.11: (a) is the widefield image of an area from a sample of quantum dots imaged on the CMOS camera using 638 nm excitation. (b) and (c) are the respective confocal and image scanning images over 16×16 scanned positions of the 462 nm beam. (d) The easySTORM image of the same region (a) under 638 nm excitation. (e) is the intensity line plots across the region marked as yellow in (a), (b), and (c), while (f) is the intensity line plot of the same region in the easySTORM image (d).

We then use the combined STORM and beam scanning microscope in the fluorescence mode to image the QD sample slide. First, a widefield image of an area of the QD sample is captured by using the 638 nm excitation, and the same is shown in Figure 6.11 (a). We then perform beam scanning microscopy of the same region using the 462 nm beam, and a scan is performed over 16×16 positions. The confocal and ISM images thus constructed are shown in Figures 6.10 (b) and (c),

respectively. Once the beam scanning is over, we switch to perform easySTORM of the same region as in Figure 6.11 (a), by acquiring ≈ 10,000 images using the 638 nm excitation. The reconstructed super-resolved image is shown in Figure 6.10 (d). Figure 6.10 (e) shows the intensity line plots across the regions marked as yellow in Figure 6.10 (a-c). From the intensity line plots, it is clear that the ISM and confocal images provide better resolution as compared to the widefield image, while ISM delivers better signal to noise compared to confocal and widefield. Figure 6.10 (f) shows the intensity line plot across the same region, marked as yellow in Figure 6.10 (d). The plot clearly indicates that the QDs are getting super-resolved in the STORM image.

6.5 Summary

We have introduced piSTORM, a programmable illumination scheme for STORM that enables dynamic control of the intensity level and spatial distribution of the excitation beam in the sample plane using a liquid crystal spatial light modulator that functions as a dynamic hologram. Implemented on the openFrame-based modular microscope, piSTORM allows arbitrary, user-defined illumination patterns to be generated and updated in real time without mechanical movement of optical components. This capability enables selective STORM acquisitions from multiple, spatially distinct regions of the same sample plane performed at different instances of time. We have also shown that piSTORM allows simultaneous excitation of different regions within the same field of view with different intensity levels, which can address challenges arising from spatially varying fluorophore densities in the specimen. Finally, the Chapter demonstrates a combined STORM and beam scanning microscopy (confocal and image scanning microscopy) technique that integrates the illumination paths of STORM with that of a scanning microscope, in a single microscope platform. This enables super-resolution alongside high-resolution imaging of the same region in the sample plane.

* * *

Chapter 7

Conclusion and Future Work

7.1 Conclusion

Optical microscopy has long served as a fundamental tool for imaging biological and clinical samples, owing to its compatibility with both dead/dry and living samples. However, its spatial resolution is fundamentally limited due to diffraction, restricting the visualization of structures of size up to about 200 nm only. Although techniques such as confocal microscopy and image scanning microscopy offer improvements in resolution up to $\approx$ 150 nm, achieving true super-resolution beyond 100 nm requires advanced optical microscopy methods. Over the last decade, several advanced optical microscopy methods have been developed using visible light that can overcome the limitations previously imposed by diffraction, achieving true super-resolution. These methods are collectively referred to as optical super-resolution microscopy (OSRM) methods. OSRM techniques, like confocal based stimulated emission depletion microscopy (STED), widefield based structured illumination microscopy (SIM), and stochastic optical reconstruction microscopy (STORM), are widely acknowledged. Despite their transformative potential for biological research and cancer diagnostics, commercial OSRM systems remain expensive and unaffordable for many research organizations, clinics, and educational institutions. Fortunately, easySTORM, a variant of STORM, which provides nanometer scale resolution ($\leq$ 20 nm), remains comparatively simple and can be implemented cost-effectively in a widefield microscope. However, the efficacy of such low-cost systems needs to be investigated properly, especially in the geographical and physical settings where the system needs to be operated. Equally important is the upgradation of the capabilities of easySTORM in terms of resolution and practical considerations that become important while imaging biological specimens.

This thesis has focused on the development of an open-source, affordable, and modular microscope, which was augmented to perform easySTORM. The modular microscope is constructed using industry-grade, cost-effective components and open-source software. The system works in both brightfield and widefield mode and, as already mentioned, its working is extended to STORM for super-resolved fluorescence imaging. The system's performance has been systematically evaluated on biological specimens prepared and imaged under hot and humid sub-tropical conditions (specific to Asia and the Indian subcontinent), where environmental factors such as temperature and humidity pose additional challenges to system stability and imaging reliability. Further, optimized sample preparation and preservation strategies tailored for STORM imaging in these conditions have also been discussed in the thesis. To enhance resolution in STORM, a UV–violet photoinduced recovery strategy has been employed that extended fluorophore blinking and increased localization events. In addition, a programmable holographic illumination approach has been introduced to enable selective excitation of arbitrarily shaped regions with spatially controlled intensity, thereby reducing unnecessary photobleaching of unilluminated regions and improving reconstruction quality. Finally, we have integrated the excitation paths of STORM with beam scanning microscopes (confocal microscopy and image scanning microscopy (ISM)) in a single optical microscope platform, allowing both super-resolved and high-resolution imaging of the same sample region. Overall, this thesis work has demonstrated a robust, flexible, and cost-effective open-source framework for advanced optical super-resolution microscopy, thereby expanding accessibility to nanoscale imaging and supporting biological and biomedical research in resource-limited settings. While the developed system is not an immediate clinical diagnostic solution, it provides a step toward increasing accessibility of advanced microscopy, with potential future applications in biomedical research and clinical diagnostics after further validation.

A summary of the main contributions of the thesis Chapters is presented below.

1. Chapter 1 has introduced optical super-resolution microscopy and highlighted the need for cost-effective STORM implementation. It has outlined challenges in the current state-of-art, and then presented the objectives of the thesis, which tried to address some of the challenges.

2. Chapter 2 has provided a historical perspective on microscopy, explained the importance of resolution, and discussed methods to surpass the diffraction

limit. It has detailed STORM fundamentals, including fluorophore blinking and the image reconstruction process, along with the working of easySTORM.

3. Chapter 3 has described the development of an affordable, modular, research-grade optical microscope using accessible components, lasers, cameras, and open-source software. Performance of the developed system has been validated using physical targets, biological cells, and tissue sections, and performance has been compared with that of commercial microscopes.

4. Chapter 4 has outlined the implementation of easySTORM in the modular microscope for single-color and multi-color imaging of physical and biological samples. It has explained in detail the image acquisition, reconstruction, sample preparation, and implementation challenges.

5. Chapter 5 has introduced the photoinduced recovery mechanism and presented its experimental validation to enhance STORM resolution. It explored various combinations of excitation and recovery beam parameters for fluorophores in an imaging buffer that could yield the best super-resolved images. The Chapter has further applied the optimized STORM settings to image multiple human non-cancerous and cancerous cell lines to investigate the variations of their cytoskeletal filament widths.

6. Chapter 6 has presented a novel dynamic holographic beam modulation scheme for user-defined illumination in STORM. The Chapter has demonstrated this novel technique by imaging quantum dots and biological samples. The Chapter has further presented a multimodal imaging system by integrating STORM with beam scanning microscopy techniques (confocal and ISM). Its performance has been validated by acquiring STORM, confocal, and image scanning images from the same region of a quantum dot sample.

7. Chapter 7 has summarized the key findings in thesis Chapters and outlined the future research directions, including potential improvements to existing methods.

7.2 Future Work

This thesis work can be further extended to implement some of the essential tasks needed for the present state-of-art STORM. Below, we present a few of them.

1. Optimization of STORM for various dyes in different imaging buffers like PVA-based Mowiol, Vectashield, EC-Oxyrase, and Glucose Oxidase. This task aims to assist users in selecting the most suitable dye-buffer combinations via optimization of imaging protocols by determining the best signal to noise ratios, switching cycle periods, and overall resolution across a range of laser illumination intensities.

2. Combined STORM-beam scanning microscopy with Hyperspectral imaging of the same area on the sample plane in a single microscope platform. With STORM and beam scanning, we can simultaneously obtain a super-resolved image and a high-resolution image, while Hyperspectral imaging allows detailed information about the spectral properties of the sample. Thus, we can have a spatially resolved and spectrally resolved image of the same area on the sample using a single microscope platform.

3. Another future direction involves time-sequential scanning in STORM using programmable illumination with a spatial light modulator and live image reconstruction. Targeting of small, user-defined regions dynamically and sequentially will enable efficient scanning of the full field of view while minimizing unnecessary exposure and photobleaching. Real-time localization and reconstruction will reduce post-processing time and will be useful in fundamental biological research to investigate molecular organization, protein interactions, cellular structures, and nanoscale biological processes, along with clinical applications.

4. Another new research direction involves developing a high-throughput STORM system with a large field of view (FOV), enabling simultaneous imaging of thousands to millions of molecules. This goal can be realized by (a) upgrading microscopy hardware with high-speed and high-sensitivity detectors, (b) implementing advanced algorithms to handle large datasets, and (c) optimizing the optical setup with larger FOV cameras.

5. Yet another task is to develop an affordable, smart STORM platform utilizing a smartphone camera for image acquisition. Integrating on-device computation into the smartphone itself for real-time localization, along with autofocus and adaptive imaging into the system, will enable high-quality super-resolution imaging. This approach will make STORM more accessible and suitable for point of care or field applications.

* * *

Appendix A

Softwares used during the research work

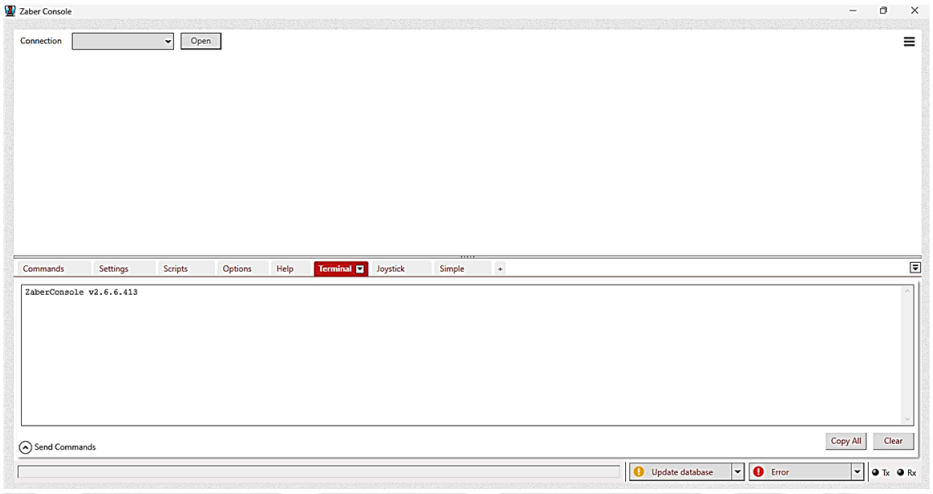

Figure A.1: A screenshot showing the Zaber Console Software.

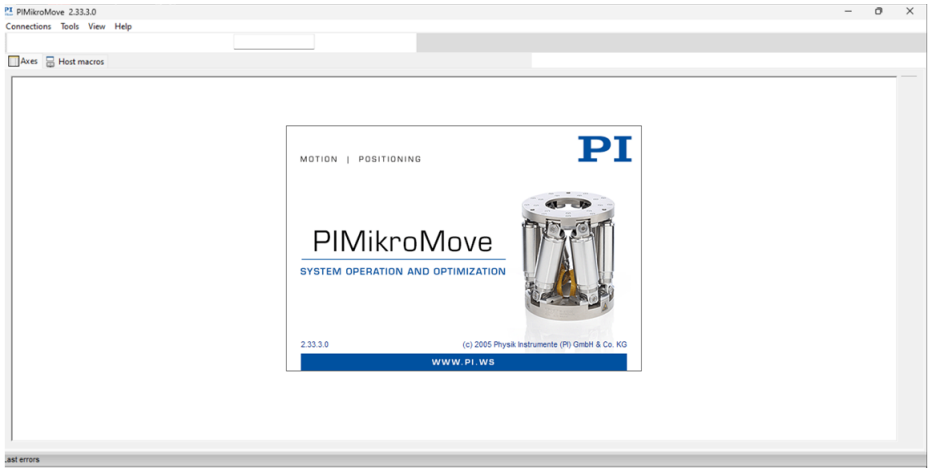

Figure A.2: A screenshot showing the PIMikroMove software.

Figure A.3: A screenshot showing on the left the Arduino IDE software and on the right a sketch page to upload the Arduino Firmware software code.

(a) (b)

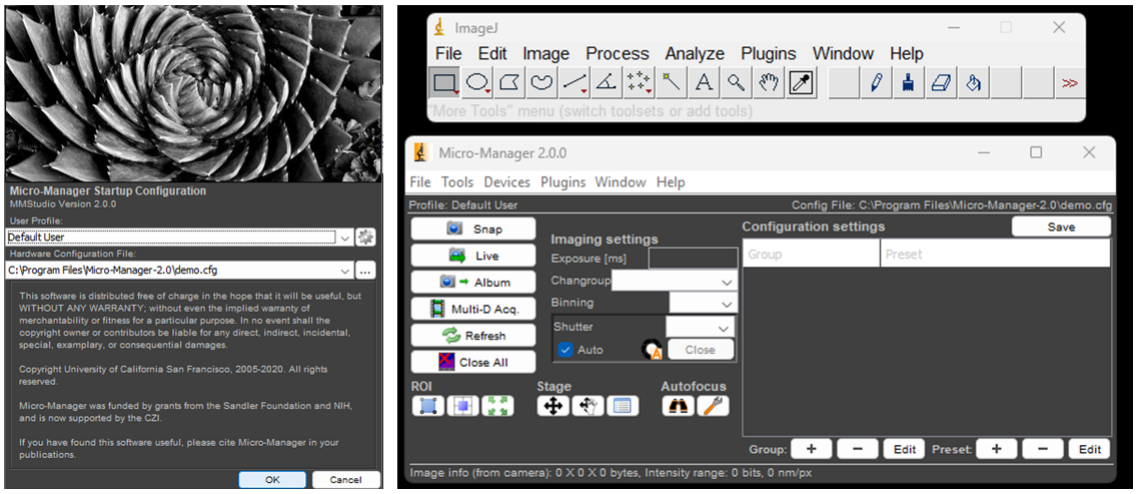

Figure A.4: Screenshots showing in (a) the μManager software startup configuration and in (b) (top) the ImageJ integration with the (bottom) μManager panel.

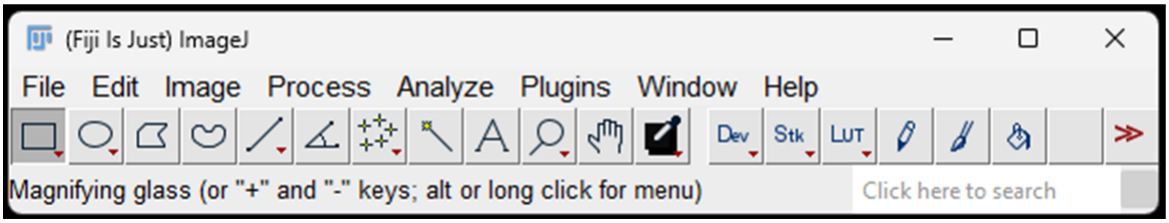

Figure A.5: A screenshot showing the Fiji software.

Appendix B

Adding Arduino into μManager

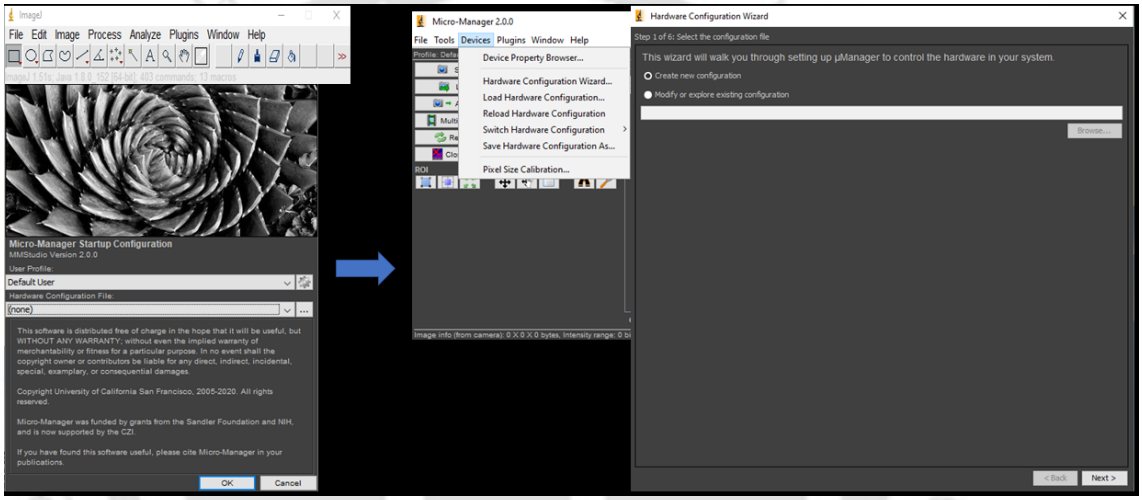

Figure B.1: A screenshot showing the μManager setup configuration and the Hardware Configuration Wizard under the Device option.

To add an Arduino in the μManager, at first, the μManager is run, and in the Startup Configuration, the Hardware Configuration File is set to "none". This is followed by clicking the Devices→Hardware Configuration Wizard→Create a new configuration as shown in Figure B.1. Then we choose the Arduino→*Arduino-Hub: Hub (required) in the Hardware Configuration Wizard as shown in Figure B.2. This is followed by clicking the Add icon and then setting the Port Value and Port Properties in the Device Arduino-Hub; Library Arduino. In the Port Properties, the BaudRate is set to 57600, Verbose is kept to 0, and other properties are set to the default. This is followed by checking the Arduino-DAC2 option in the Peripheral Devices Setup and then writing an appropriate Device name in the Device Arduino-DAC2; Library Arduino. This Device name must be carefully chosen so that it does not conflict with other file names. Subsequently, we click the "next" option

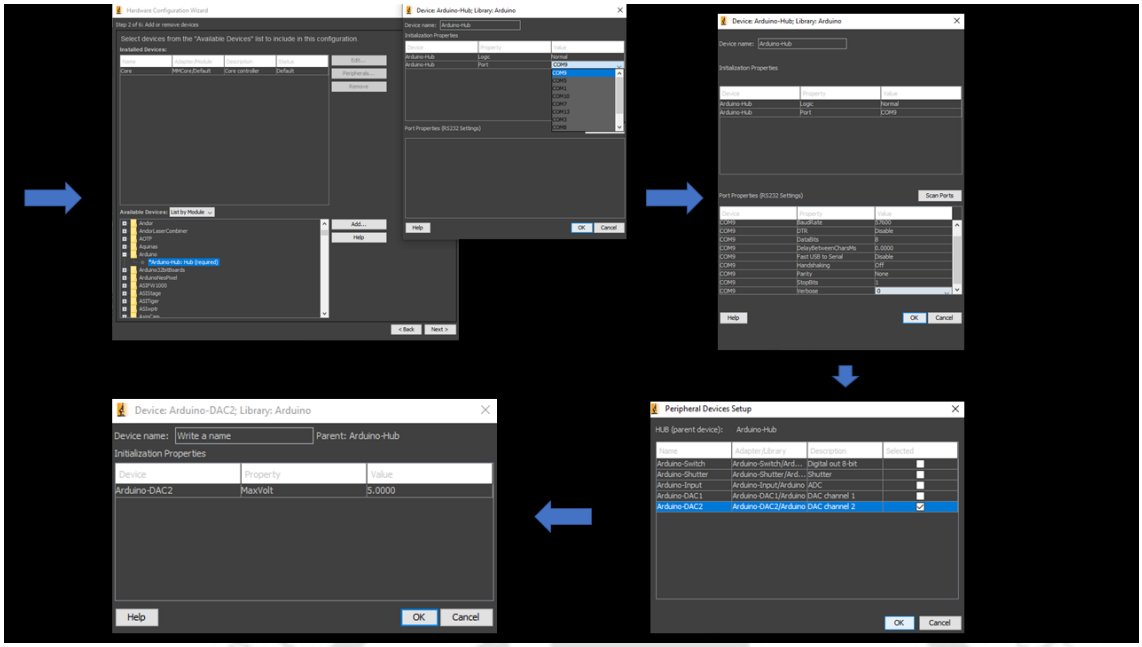

Figure B.2: Screenshots showing the addition of Arduino, setting the communication (COM) port, port properties, peripheral device setup, and putting a device name.

till we arrive at the Hardware Configuration Wizard, where we put the name of the configuration (.cfg) file as shown in Figure B.3. The .cfg file must be included in the μManager installation folder (default C:\Program Files\Micromanager). This is possible by browsing for the same in this wizard itself. Once done, we get back to the μManager panel and click on the (+) icon near the Group option available at the bottom of the μManager panel. This opens the Group Editor. Here we check the Device name-volts and put a suitable name in the Group name. Once done, we get the Device name under the Configuration Settings with a slider, allowing us to change the Arduino voltage between 0 and 5 volts. Before closing the μManager, we need to save the .cfg file for the first time.

Later on, when we run the μManager, we can browse and choose the same .cfg file that was created earlier, and it does not require setting a new Hardware Configuration File in the Startup Configuration. However, if we want to add other Arduino or hardware into the same .cfg file, we choose the same in the Startup Configuration and then go to the Devices→Load Hardware Configuration→Modify or explore existing configuration. This allows us to add, remove, or change devices in the existing .cfg file.

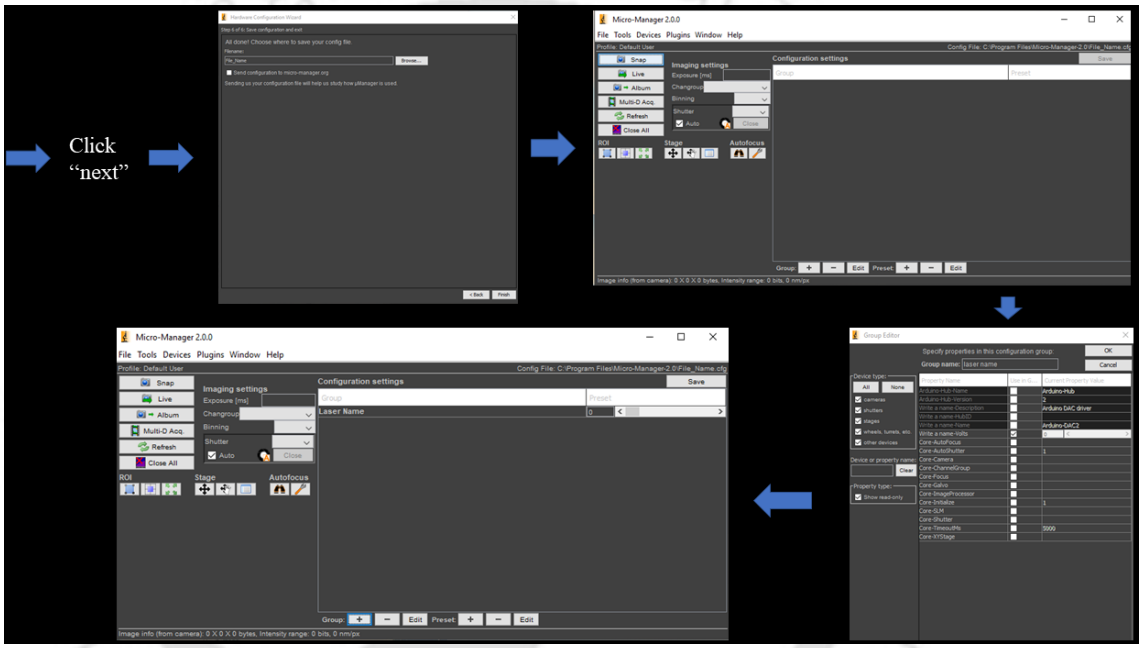

Figure B.3: Screenshots showing the final file name configuration and adding the Arduino to the group.

Appendix C

Plot of transmission against wavelength for the multiline dichroic splitter and optical filters

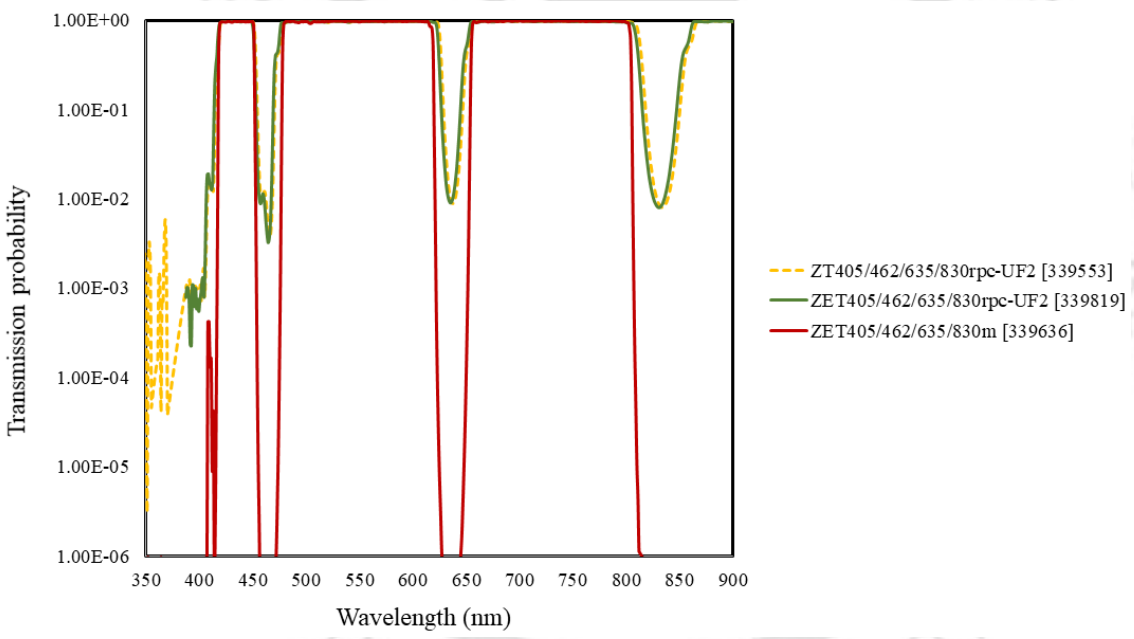

Figure C.1: Plot showing the transmission probability against the wavelength for the multiline dichroic beam splitter (orange), excitation (green), and emission (red) filters used in Layer 3 of the openFrame-based modular microscope.

References

[1] E. Abbe. Beiträge zur theorie des mikroskops und der mikroskopischen wahrnehmung. *Archiv für Mikroskopische Anatomie*, 9(1):413–468, Dec 1873. ISSN 0176-7364. doi: 10.1007/BF02956173. URL `https://doi.org/10.1007/BF02956173`. 1

[2] Sylvain Trépout, Philippe Bastin, and Sergio Marco. Preparation and observation of thick biological samples by scanning transmission electron tomography. *Journal of visualized experiments: JoVE*, 121:55215, 2017. 1, 8

[3] Jong Bo Park, Yong-Jin Kim, Seong-Min Kim, Je Min Yoo, Youngsoo Kim, Roman Gorbachev, II Barbolina, Sang Jin Kim, Sangmin Kang, Myung-Han Yoon, et al. Non-destructive electron microscopy imaging and analysis of biological samples with graphene coating. *2D Materials*, 3(4):045004, 2016. 1, 8

[4] Valentina Parodi, Emanuela Jacchetti, Roberto Osellame, Giulio Cerullo, Dario Polli, and Manuela Teresa Raimondi. Nonlinear optical microscopy: From fundamentals to applications in live bioimaging. *Frontiers in bioengineering and biotechnology*, 8:585363, 2020. 1

[5] Kirti Prakash, Benedict Diederich, Rainer Heintzmann, and Lothar Schermelleh. Super-resolution microscopy: a brief history and new avenues. *Philosophical Transactions of the Royal Society A: Mathematical, Physical and Engineering Sciences*, 380(2220):20210110, 2022. doi: 10.1098/rsta.2021.0110. URL `https://royalsocietypublishing.org/doi/abs/10.1098/rsta.2021.0110`. 1

[6] Mark AA Neil, Rimas Juškaitis, and Tony Wilson. Method of obtaining optical sectioning by using structured light in a conventional microscope. *Optics letters*, 22(24):1905–1907, 1997. 1

[7] M. G. L. Gustafsson. Surpassing the lateral resolution limit by a factor of two using structured illumination microscopy. *Journal of Microscopy*, 198(2):82–87, 2000. doi: https://doi.org/10.1046/j.1365-2818.2000.00710.x. URL `https://onlinelibrary.wiley.com/doi/abs/10.1046/j.1365-2818.2000.00710.x`. 1, 11, 75

[8] Stefan W Hell. Far-field optical nanoscopy. *science*, 316(5828):1153–1158, 2007. 1, 12

[9] Michael J Rust, Mark Bates, and Xiaowei Zhuang. Sub-diffraction-limit imaging by stochastic optical reconstruction microscopy (storm). *Nature methods*, 3(10): 793–796, 2006. 2, 10, 17

[10] Matthew K Creech, Jing Wang, Xiaolin Nan, and Summer L Gibbs. Superresolution imaging of clinical formalin fixed paraffin embedded breast cancer with single molecule localization microscopy. *Scientific reports*, 7(1):40766, 2017. 2, 41

[11] Ray R Zhang, Alexandra B Schroeder, Joseph J Grudzinski, Eben L Rosenthal, Jason M Warram, Anatoly N Pinchuk, Kevin W Eliceiri, John S Kuo, and Jamey P Weichert. Beyond the margins: real-time detection of cancer using targeted fluorophores. *Nature reviews Clinical oncology*, 14(6):347–364, 2017. 2, 41

[12] Yalan Yu, Jianing Yu, Zhen-Li Huang, and Fuling Zhou. Application of superresolution fluorescence microscopy in hematologic malignancies. *Journal of Innovative Optical Health Sciences*, 15(02):2230005, 2022. 2, 41

[13] Johannes Hohlbein, Benedict Diederich, Barbora Marsikova, Emmanuel G Reynaud, Séamus Holden, Wiebke Jahr, Robert Haase, and Kirti Prakash. Open microscopy in the life sciences: quo vadis? *Nature methods*, 19(9):1020–1025, 2022. 2

[14] Jesse S. Aaron, Caron A. Jacobs, Leonel Malacrida, Antje Keppler, Paul French, Daniel A. Fletcher, Christopher Wood, Claire M. Brown, Graham D. Wright, Satoshi Ogawa, Mahmoud Maina, and Teng-Leong Chew. Challenges of microscopy technology dissemination to resource-constrained communities. *Nature Methods*, May 2025. ISSN 1548-7105. doi: 10.1038/s41592-025-02690-7. URL `https://doi.org/10.1038/s41592-025-02690-7`. 2, 19

[15] Benjamin D. Knapp and Kerwyn Casey Huang. The effects of temperature on cellular physiology. *Annual Review of Biophysics*, 51(Volume 51, 2022):499–526, 2022. ISSN 1936-1238. doi: https://doi.org/10.1146/annurev-biophys-112221-074832. URL `https://www.annualreviews.org/content/journals/10.1146/annurev-biophys-112221-074832`. 3

[16] James Joubert and Deepak Sharma. Using cmos cameras for light microscopy. *Microscopy Today*, 19(4):22–28, 07 2011. ISSN 1551-9295. doi: 10.1017/S155192951100054X. URL `https://doi.org/10.1017/S155192951100054X`. 3

[17] Thomas H Jamieson. Thermal effects in optical systems. *Optical Engineering*, 20(2):156–160, 1981. 3

[18] Ingo Gregor and Jörg Enderlein. Image scanning microscopy. *Current Opinion in Chemical Biology*, 51:74–83, 2019. ISSN 1367-5931. doi: https://doi.org/10.1016/j.cbpa.2019.05.011. URL `https://www.sciencedirect.com/science/article/pii/S1367593119300456`. Chemical Genetics and Epigenetics • Molecular Imaging. 4, 10

[19] Anupam Bharadwaj, Ranjan Kalita, Amalesh Kumar, Anupam Sarma, Bithiah G Jaganathan, Sunil Kumar, Frederik Gorlitz, Jonathan Lightley, Chris Dunsby, Mark Neil, et al. A cost-effective, modular, research-grade optical microscope. *Curr. Sci.*, 126(2):244–254, 2024. 4, 5, 19, 20, 21, 29

[20] Kwasi Kwakwa, Alexander Savell, Timothy Davies, Ian Munro, Simona Parrinello, Marco A Purbhoo, Chris Dunsby, Mark AA Neil, and Paul MW French. easystorm: a robust, lower-cost approach to localisation and tirf microscopy. *Journal of biophotonics*, 9(9):948–957, 2016. 5, 18

[21] Sebastian Van De Linde, Ivan Krstić, Thomas Prisner, Sören Doose, Mike Heilemann, and Markus Sauer. Photoinduced formation of reversible dye radicals and their impact on super-resolution imaging. *Photochemical & Photobiological Sciences*, 10(4):499–506, 2011. 5, 57, 69

[22] Yong Wang, Xiushuo Zhang, Jing Xu, Xiangyu Sun, Xiaolong Zhao, Hongsheng Li, Yanping Liu, Jingjing Tian, Xiaorui Hao, Xiaofei Kong, et al. The development of microscopic imaging technology and its application in micro-and nanotechnology. *Frontiers in Chemistry*, 10:931169, 2022. 7

[23] Clara Sue Ball. The early history of the compound microscope. *Bios*, pages 51–60, 1966. 7

[24] King-Thom Chung and Jong-Kang Liu. *Pioneers in microbiology: the human side of science*. World Scientific, 2017. 7

[25] Robert Hooke. *Micrographia: or some physiological descriptions of minute bodies made by magnifying glasses, with observations and inquiries thereupon*. Courier Corporation, 2003. 7

[26] Pedro J Mestres Ventura. The electron microscope on the eve of its first centenary. *HISTORY*, 27(1):111–127, 2023. 7

[27] Joseph W Goodman. *Introduction to Fourier optics*. Roberts and Company publishers, 2005. 9, 16

[28] Amicia D Elliott. Confocal microscopy: principles and modern practices. *Current protocols in cytometry*, 92(1):e68, 2020. 9

[29] Douglas B Murphy and Michael W Davidson. *Fundamentals of light microscopy and electronic imaging*. John Wiley & Sons, 2012. 9

[30] Redmond P Aylward. Advanced galvanometer-based optical scanner design. *Sensor review*, 23(3):216–222, 2003. 9

[31] Peter Saggau. New methods and uses for fast optical scanning. *Current opinion in neurobiology*, 16(5):543–550, 2006. 9

[32] M Minsky. Microscopy apparatus, 1961. US Patent 30,130,467. 9

[33] Colin JR Sheppard, Shalin B Mehta, and Rainer Heintzmann. Superresolution by image scanning microscopy using pixel reassignment. *Optics letters*, 38(15): 2889–2892, 2013. 10

[34] Sebastian Van de Linde, Anna Löschberger, Teresa Klein, Meike Heidbreder, Steve Wolter, Mike Heilemann, and Markus Sauer. Direct stochastic optical reconstruction microscopy with standard fluorescent probes. *Nature protocols*, 6(7):991–1009, 2011. 13, 17, 69

[35] Graham T Dempsey, Mark Bates, Walter E Kowtoniuk, David R Liu, Roger Y Tsien, and Xiaowei Zhuang. Photoswitching mechanism of cyanine dyes. *Journal of the American Chemical Society*, 131(51):18192–18193, 2009. 14, 57, 69

[36] Robert M Dickson, Andrew B Cubitt, Roger Y Tsien, and William E Moerner. On/off blinking and switching behaviour of single molecules of green fluorescent protein. *Nature*, 388(6640):355–358, 1997. 15, 59

[37] Russell E Thompson, Daniel R Larson, and Watt W Webb. Precise nanometer localization analysis for individual fluorescent probes. *Biophysical journal*, 82 (5):2775–2783, 2002. 15

[38] Hendrik Deschout, Francesca Cella Zanacchi, Michael Mlodzianoski, Alberto Diaspro, Joerg Bewersdorf, Samuel T Hess, and Kevin Braeckmans. Precisely and accurately localizing single emitters in fluorescence microscopy. *Nature methods*, 11(3):253–266, 2014. 16, 52

[39] Photo-Switchable Fluorescent Probes. Multicolor super-resolution imaging with. *science*, 1146598(1749):317, 2007. 17

[40] Mike Heilemann, Sebastian Van De Linde, Mark Schüttpelz, Robert Kasper, Britta Seefeldt, Anindita Mukherjee, Philip Tinnefeld, and Markus Sauer. Subdiffraction-resolution fluorescence imaging with conventional fluorescent probes. *Angewandte Chemie-International Edition*, 47(33), 2008. 17, 54

[41] Guillaume Jacquemet, Alexandre F Carisey, Hellyeh Hamidi, Ricardo Henriques, and Christophe Leterrier. The cell biologist's guide to super-resolution microscopy. *Journal of Cell Science*, 133(11):jcs240713, 2020. 19

[42] Karl-Jürgen Halbhuber and Karsten König. Modern laser scanning microscopy in biology, biotechnology and medicine. *Annals of Anatomy-Anatomischer Anzeiger*, 185(1):1–20, 2003. 19

[43] Jan Willem Borst and Antonie JWG Visser. Fluorescence lifetime imaging microscopy in life sciences. *Measurement Science and Technology*, 21(10):102002, 2010. 19

[44] Edwin Garcia, Jonathan Lightley, Sunil Kumar, Ranjan Kalita, Frederik Gőrlitz, Yuriy Alexandrov, Terry Cook, Christopher Dunsby, Mark AA Neil,

Candice A Roufosse, et al. Application of direct stochastic optical reconstruction microscopy (dstorm) to the histological analysis of human glomerular disease. *The Journal of Pathology: Clinical Research*, 7(5):438–445, 2021. 19, 41, 49, 78

[45] Arthur Edelstein, Nenad Amodaj, Karl Hoover, Ron Vale, and Nico Stuurman. Computer control of microscopes using μmanager. *Current protocols in molecular biology*, 92(1):14–20, 2010. 21

[46] J Lightley, S Kumar, MQ Lim, E Garcia, F Görlitz, Y Alexandrov, T Parrado, C Hollick, E Steele, K Roßmann, et al. openframe: a modular, sustainable, open microscopy platform with single-shot, dual-axis optical autofocus module providing high precision and long range of operation. *Journal of Microscopy*, 292(2):64–77, 2023. 23

[47] Johannes Schindelin, Ignacio Arganda-Carreras, Erwin Frise, Verena Kaynig, Mark Longair, Tobias Pietzsch, Stephan Preibisch, Curtis Rueden, Stephan Saalfeld, Benjamin Schmid, et al. Fiji: an open-source platform for biological-image analysis. *Nature methods*, 9(7):676–682, 2012. 29

[48] Caroline A Schneider, Wayne S Rasband, and Kevin W Eliceiri. Nih image to imagej: 25 years of image analysis. *Nature methods*, 9(7):671–675, 2012. 29

[49] Hongki Yoo, Incheon Song, and D-G GWEON. Measurement and restoration of the point spread function of fluorescence confocal microscopy. *Journal of microscopy*, 221(3):172–176, 2006. 35

[50] Jianxin Chen, Jian Xu, Deyong Kang, Meifang Xu, Shuangmu Zhuo, Xiaoqin Zhu, and Xingshan Jiang. Multiphoton microscopic imaging of histological sections without hematoxylin and eosin staining differentiates carcinoma in situ lesion from normal oesophagus. *Applied Physics Letters*, 103(18), 2013. 39

[51] Summer L Gibbs, Elizabeth Genega, Jeffery Salemi, Vida Kianzad, Haley L Goodwill, Yang Xie, Rafiou Oketokoun, Parmeshwar Khurd, Ali Kamen, and John V Frangioni. Near-infrared fluorescent digital pathology for the automation of disease diagnosis and biomarker assessment. *Molecular imaging*, 14(5): 7290–2015, 2015. 39

[52] Z Jehan, S Uddin, and K S Al-Kuraya. In-situ hybridization as a molecular tool in cancer diagnosis and treatment. *Current medicinal chemistry*, 19(22): 3730–3738, 2012. 41

[53] A Orfao, J Ciudad, M Gonzalez, A Lopez, M Del Mar Abad, JI Paz Bouza, JJ Cruz, A Gomez Alonso, and JF San Miguel. Flow cytometry in the diagnosis of cancer. *Scandinavian Journal of Clinical and Laboratory Investigation*, 55 (sup221):145–152, 1995. 41

[54] John SH Danial, Jeff YL Lam, Yunzhao Wu, Matthew Woolley, Eleni Dimou, Matthew R Cheetham, Derya Emin, and David Klenerman. Constructing a cost-efficient, high-throughput and high-quality single-molecule localization microscope for super-resolution imaging. *Nature protocols*, 17(11):2570–2619, 2022. 41

[55] Anupam Bharadwaj, Amalesh Kumar, Ranjan Kalita, Rumela Mitra, Amit Sharma, Bithiah Grace Jaganathan, Jina Bhattacharyya, Anupam Sarma, Edwin Garcia, Sunil Kumar, et al. Super-resolved fluorescence imaging utilising accessible stochastic optical reconstruction microscopy (easystorm) implemented on a low-cost, modular open-source (openframe) microscope. *Measurement Science and Technology*, 35(12):125402, 2024. 41, 46

[56] Martin Ovesnỳ, Pavel Křížek, Josef Borkovec, Zdeněk Švindrych, and Guy M Hagen. Thunderstorm: a comprehensive imagej plug-in for palm and storm data analysis and super-resolution imaging. *Bioinformatics*, 30(16):2389–2390, 2014. 42

[57] Kim I Mortensen, L Stirling Churchman, James A Spudich, and Henrik Flyvbjerg. Optimized localization analysis for single-molecule tracking and super-resolution microscopy. *Nature methods*, 7(5):377–381, 2010. 45

[58] I Izeddin, J Boulanger, V Racine, CG Specht, A Kechkar, D Nair, A Triller, D Choquet, M Dahan, and JB Sibarita. Wavelet analysis for single molecule localization microscopy. *Optics express*, 20(3):2081–2095, 2012. 45

[59] David W Scott. Averaged shifted histograms: effective nonparametric density estimators in several dimensions. *The Annals of Statistics*, pages 1024–1040, 1985. 45

[60] Atul Kumar, Jina Bhattacharyya, and Bithiah Grace Jaganathan. Adhesion to stromal cells mediates imatinib resistance in chronic myeloid leukemia through erk and bmp signaling pathways. *Scientific reports*, 7(1):9535, 2017. 46

[61] Jianquan Xu, Hongqiang Ma, and Yang Liu. Stochastic optical reconstruction microscopy (storm). *Current protocols in cytometry*, 81(1):12–46, 2017. 46, 49, 57

[62] Rachel E Mahaffy and Thomas D Pollard. Influence of phalloidin on the formation of actin filament branches by arp2/3 complex. *Biochemistry*, 47(24): 6460–6467, 2008. 46

[63] Kyuseok Im, Sergey Mareninov, M Fernando Palma Diaz, and William H Yong. *An introduction to performing immunofluorescence staining*. Springer, 2019. 46, 47

[64] Mike Heilemann, Emmanuel Margeat, Robert Kasper, Markus Sauer, and Philip Tinnefeld. Carbocyanine dyes as efficient reversible single-molecule optical switch. *Journal of the American Chemical Society*, 127(11):3801–3806, 2005. 47

[65] Mickaël Lelek, Melina T Gyparaki, Gerti Beliu, Florian Schueder, Juliette Griffié, Suliana Manley, Ralf Jungmann, Markus Sauer, Melike Lakadamyali, and Christophe Zimmer. Single-molecule localization microscopy. *Nature reviews methods primers*, 1(1):39, 2021. 57

[66] Graham T Dempsey, Joshua C Vaughan, Kok Hao Chen, Mark Bates, and Xiaowei Zhuang. Evaluation of fluorophores for optimal performance in localization-based super-resolution imaging. *Nature methods*, 8(12):1027–1036, 2011. 57

[67] Xinghua Shi, John Lim, and Taekjip Ha. Acidification of the oxygen scavenging system in single-molecule fluorescence studies: in situ sensing with a ratiometric dual-emission probe. *Analytical chemistry*, 82(14):6132–6138, 2010. 57

[68] Nicolas Olivier, Debora Keller, Vinoth Sundar Rajan, Pierre Gönczy, and Suliana Manley. Simple buffers for 3d storm microscopy. *Biomed. Opt. Express*, 4(6):885–899, Jun 2013. doi: 10.1364/BOE.4.000885. URL `https://opg.optica.org/boe/abstract.cfm?URI=boe-4-6-885`. 57

[69] Shamala Ravikumar, R Surekha, and Rooban Thavarajah. Mounting media: An overview. *Journal of Dr. YSR University of Health Sciences*, 3(Suppl 1): S1–S8, 2014. 57

[70] Colin Echeverría Aitken, R Andrew Marshall, and Joseph D Puglisi. An oxygen scavenging system for improvement of dye stability in single-molecule fluorescence experiments. *Biophysical journal*, 94(5):1826–1835, 2008. 57

[71] Kai Kikuchi, Liam D Adair, Jiarun Lin, Elizabeth J New, and Amandeep Kaur. Photochemical mechanisms of fluorophores employed in single-molecule localization microscopy. *Angewandte Chemie*, 135(1):e202204745, 2023. 57

[72] Leila Nahidiazar, Alexandra V Agronskaia, Jorrit Broertjes, Bram van den Broek, and Kees Jalink. Optimizing imaging conditions for demanding multicolor super resolution localization microscopy. *PloS one*, 11(7):e0158884, 2016. 57

[73] Yasser Gidi, Liam Payne, Viktorija Glembockyte, Megan S Michie, Martin J Schnermann, and Gonzalo Cosa. Unifying mechanism for thiol-induced photoswitching and photostability of cyanine dyes. *Journal of the American Chemical Society*, 142(29):12681–12689, 2020. 57

[74] Marcus Dyba, Giulio A Simonutti, and Jonas Fölling. Recent developments in gsdim microscopy. *Single Molecule Spectroscopy and Superresolution Imaging V*, 8228:148–153, 2012. 57, 59

[75] Benoit Roubinet, Michael Weber, Heydar Shojaei, Mark Bates, Mariano L Bossi, Vladimir N Belov, Masahiro Irie, and Stefan W Hell. Fluorescent photoswitchable diarylethenes for biolabeling and single-molecule localization microscopies with optical superresolution. *Journal of the American Chemical Society*, 139(19):6611–6620, 2017. 59

[76] Sina Wäldchen, Julian Lehmann, Teresa Klein, Sebastian Van De Linde, and Markus Sauer. Light-induced cell damage in live-cell super-resolution microscopy. *Scientific reports*, 5(1):15348, 2015. 59, 60

[77] Jörg Enderlein. Breaking the diffraction limit with dynamic saturation optical microscopy. *Applied physics letters*, 87(9), 2005. 59

[78] Jonas Fölling, Mariano Bossi, Hannes Bock, Rebecca Medda, Christian A Wurm, Birka Hein, Stefan Jakobs, Christian Eggeling, and Stefan W Hell. Fluorescence nanoscopy by ground-state depletion and single-molecule return. *Nature methods*, 5(11):943–945, 2008. 59

[79] Jan Vogelsang, Christian Steinhauer, Carsten Forthmann, Ingo H Stein, Britta Person-Skegro, Thorben Cordes, and Philip Tinnefeld. Make them blink: Probes for super-resolution microscopy. *ChemPhysChem*, 11(12):2475–2490, 2010. 59

[80] Griša G Prinčič, Tina Jarc, Katja Kristan, Mateja Erdani Kreft, and Peter Veranič. Uv light induced fluorescence recovery of gfp after photobleaching in microscopy imaging. *Image Analysis and Stereology*, 41(2):161–169, 2022. 59

[81] Anupam Bharadwaj, Amalesh Kumar, Bithiah Grace Jaganathan, and Bosanta R. Boruah. pistorm: programmable illumination in stochastic optical reconstruction microscopy. *Opt. Lett.*, 50(21):6477–6480, Nov 2025. doi: 10.1364/OL.575930. URL `https://opg.optica.org/ol/abstract.cfm?URI=ol-50-21-6477`. 59, 75

[82] Partha Pratim Mondal. Minimizing photobleaching in fluorescence microscopy by depleting triplet states. *Applied Physics Letters*, 92(1), 2008. 59

[83] Anupam Bharadwaj, Amalesh Kumar, Rumela Mitra, Bithiah Grace Jaganathan, and Bosanta R Boruah. Enhanced fluorescence blinking of af647 fluorophores in mowiol via violet and uv light induced recovery for superior localization microscopy. *Methods and Applications in Fluorescence*, 12(3):035007, 2024. 60

[84] Masafumi Minoshima and Kazuya Kikuchi. Photostable and photoswitching fluorescent dyes for super-resolution imaging. *JBIC Journal of Biological Inorganic Chemistry*, 22:639–652, 2017. 60

[85] Qinsi Zheng, Steffen Jockusch, Zhou Zhou, and Scott C Blanchard. The contribution of reactive oxygen species to the photobleaching of organic fluorophores. *Photochemistry and photobiology*, 90(2):448–454, 2014. 60

[86] Anupam Bharadwaj, Amalesh Kumar, Sam Padalumavunkal Mathew, Rumela Mitra, Jina Bhattacharyya, Bithiah Grace Jaganathan, and Bosanta R Boruah.

Advancing cellular insights: Super-resolution storm imaging of cytoskeletal structures in human stem and cancer cells. *Biochemistry and Biophysics Reports*, 39:101798, 2024. 61

[87] Niccolo Banterle, Khanh Huy Bui, Edward A Lemke, and Martin Beck. Fourier ring correlation as a resolution criterion for super-resolution microscopy. *Journal of structural biology*, 183(3):363–367, 2013. 68

[88] Sami Koho, Giorgio Tortarolo, Marco Castello, Takahiro Deguchi, Alberto Diaspro, and Giuseppe Vicidomini. Fourier ring correlation simplifies image restoration in fluorescence microscopy. *Nature communications*, 10(1):3103, 2019. 68

[89] Robert PJ Nieuwenhuizen, Keith A Lidke, Mark Bates, Daniela Leyton Puig, David Grünwald, Sjoerd Stallinga, and Bernd Rieger. Measuring image resolution in optical nanoscopy. *Nature methods*, 10(6):557–562, 2013. 68

[90] Sudeepa Rajan, Dmitri S Kudryashov, and Emil Reisler. Actin bundles dynamics and architecture. *Biomolecules*, 13(3):450, 2023. 72

[91] Alexander Rigort, David Günther, Reiner Hegerl, Daniel Baum, Britta Weber, Steffen Prohaska, Ohad Medalia, Wolfgang Baumeister, and Hans-Christian Hege. Automated segmentation of electron tomograms for a quantitative description of actin filament networks. *Journal of structural biology*, 177(1):135–144, 2012. 72

[92] Bosanta R Boruah. Dynamic manipulation of a laser beam using a liquid crystal spatial light modulator. *American Journal of Physics*, 77(4):331–336, 2009. 74, 75

[93] Quentin Hanley, Rainer Heintzmann, Donna Arndt-Jovin, and Thomas Jovin. Programmable Array Microscopes. *Microscopy Today*, 8(8):16–23, 03 2018. ISSN 1551-9295. doi: 10.1017/S1551929500060417. URL `https://doi.org/10.1017/S1551929500060417`. 75

[94] Jiunn-Yuan Lin, Ru-Ping Huang, Pei-Shiu Tsai, and Chau-Hwang Lee. Wide-field super-resolution optical sectioning microscopy using a single spatial light modulator. *Journal of Optics A: Pure and Applied Optics*, 11(1):015301, dec

2008. doi: 10.1088/1464-4258/11/1/015301. URL `https://dx.doi.org/10.1088/1464-4258/11/1/015301`. 75

[95] Yao L Wang, Noa WF Grooms, Sabrina C Civale, and Samuel H Chung. Confocal imaging capacity on a widefield microscope using a spatial light modulator. *Plos one*, 16(2):e0244034, 2021. 75

[96] Karuna Sindhu Malik, Nagendra Kumar, and Bosanta R Boruah. Dynamic modulation of spatial intensity profile of a laser beam using a binary hologram. *Optics Communications*, 515:128201, 2022. 75

Publications/Conferences/Employment/Workshops

List of Publications

I. **Patent**

(1) **Anupam Bharadwaj**, Amalesh Kumar, Bithiah Grace Jaganathan, and Bosanta Ranjan Boruah, "SYSTEM AND METHOD FOR DYNAMIC MODULATION OF ILLUMINATION BEAM INTENSITY IN STOCHASTIC OPTICAL RECONSTRUCTION MICROSCOPY." Indian Patent Application No.: 202431097118, Dec 9, 2024.

(2) **Anupam Bharadwaj**, Neeraj Kumar, and Bosanta Ranjan Boruah, "SYSTEM AND METHOD FOR A COMBINED WIDEFIELD, SINGLE MOLECULE LOCALIZATION AND BEAM SCANNING MICROSCOPES." Submitted for IPR filing (2026).

II. **Journals**

(1) **Anupam Bharadwaj**, Ranjan Kalita, Amalesh Kumar, Anupam Sarma, Bithiah Grace Jaganathan, Sunil Kumar, Frederik Gorlitz, Jonathan Lightley, Chris Dunsby, Mark Neil, Callum Hollick, Jeremy Graham, Paul M W French, and Bosanta Ranjan Boruah, "A cost-effective, modular, research-grade optical microscope." Curr. Sci. 126 (2024): 244-254.

(2) **Anupam Bharadwaj**, Amalesh Kumar, Ranjan Kalita, Rumela Mitra, Amit Sharma, Bithiah Grace Jaganathan, Jina Bhattacharyya, Anupam Sarma, Edwin Garcia, Sunil Kumar, Jonathon Lightley, Yuriy Alexandrov, Christopher Dunsby, Mark Neil, Paul M W French, and Bosanta Ranjan Boruah, "Super-resolved fluorescence imaging utilising accessible stochastic optical reconstruction microscopy (easySTORM) implemented on a low-cost, modular open-source (openFrame) microscope." Measurement Science and Technology 35.12 (2024): 125402.

(3) **Anupam Bharadwaj**, Amalesh Kumar, Rumela Mitra, Bithiah Grace Jaganathan, and Bosanta Ranjan Boruah, "Enhanced fluorescence blinking of AF647 fluorophores in Mowiol via violet and UV light induced recovery for superior localization microscopy." Methods and Applications in Fluorescence 12.3 (2024): 035007.

(4) **Anupam Bharadwaj**, Amalesh Kumar, Sam Padalumavunkal Mathew, Rumela Mitra, Jina Bhattacharyya, Bithiah Grace Jaganathan, and Bosanta Ranjan Boruah, "Advancing cellular insights: Super-resolution STORM imaging of cytoskeletal structures in human stem and cancer cells." Biochemistry and Biophysics Reports 39 (2024): 101798.

(5) **Anupam Bharadwaj**, Amalesh Kumar, Bithiah Grace Jaganathan, and Bosanta Ranjan Boruah, "piSTORM: programmable illumination in stochastic optical reconstruction microscopy." Optics Letters 50.21 (2025): 6477-6480.

III. **Conference Proceedings**

(1) **Anupam Bharadwaj**, Pranjal Choudhury, Ranjan Kalita, Amit Sharma, Amalesh Kumar, Bithiah Grace Jaganathan, Sunil Kumar, Jonathan Lightley, Edwin Garcia, Paul M W French, and Bosanta Ranjan Boruah, "A cost-effective implementation of optical super-resolution microscopy with STORM." Advances in Biophotonics, Nanofabrication, Optical Metrology and Nonlinear and Ultrafast Photonics: Proceedings of PHOTONICS 2023, Volume 3: 1242 (Lecture Notes in Electrical Engineering, 1242).

IV. **Book**

(1) Bosanta Ranjan Boruah,**Anupam Bharadwaj**, Pranjal Choudhury, and Amalesh Kumar, "Super-resolution Imaging using Stochastic Optical Reconstruction Microscopy." Submitted to Springer Nature (2025).

V. **Book Chapters**

(1) **Anupam Bharadwaj**, Amalesh Kumar, Ranjan Kalita, Bithiah Grace Jaganathan, Sunil Kumar, Jonathon Lightley, Edwin Garcia, Paul M W

French, and Bosanta Ranjan Boruah, "An affordable and table top research-grade optical super-resolution microscope using STORM." IConTOP-2023, ISBN-978-81-966527-8-4, University of Calcutta.

(2) Amalesh Kumar, **Anupam Bharadwaj**, Sam P Mathew, Bithiah Grace Jaganathan, and Bosanta Ranjan Boruah, "Optimization of the excitation laser power for stochastic optical reconstruction microscopy (STROM) using Vectashield mounted fluorophores." IConTOP-2023, ISBN-978-81-966527-8-4, University of Calcutta.

VI. **Other relevant publications (Not directly related to the thesis)**

(1) Amalesh Kumar, **Anupam Bharadwaj**, Pranjal Choudhury, Sam P Mathew, Bithiah Grace Jaganathan, and Bosanta Ranjan Boruah, "Tuning the excitation laser power in a stochastic optical reconstruction microscope for Alexa Fluor 647 dye in Vectashield mounting media." Review of Scientific Instruments 95.8 (2024).

(2) Pranjal Choudhury, Nagendra Kumar, **Anupam Bharadwaj** and Bosanta Ranjan Boruah, "Advancing Super-Resolution Imaging: A Comprehensive Analysis of Gaussian Fitting in STORM Microscopy." 2023 IEEE Workshop on Recent Advances in Photonics (WRAP). IEEE, 2023.

(3) Nedup Sherpa, **Anupam Bharadwaj**, Nagendra Kumar, Akanshu Chauhan, and Bosanta Ranjan Boruah, "Synchronization and clock recovery in a ferroelectric liquid crystal spatial light modulator based free-space optical communication link." Review of Scientific Instruments 94.5 (2023).

(4) Pranjal Choudhury, **Anupam Bharadwaj**, and Bosanta Ranjan Boruah, "Real-Time Lateral Drift Stabilization in Single Molecule Localization Microscopy Using Live Image Re-Registration." manuscript under preparation.

Conference Presentation

(1) "A Cost-Effective Implementation of Optical Super-Resolution Microscopy with STORM." PHOTONICS-2023, IISC Bangalore.

(2) "An affordable and table top research-grade optical super-resolution microscope using STORM." IConTOP-2023, University of Calcutta.

(3) "Advanced and affordable optical nanoscopy using Stochastic Optical Reconstruction Microscopy." PANE-2024, Tezpur University.

Academic employment/achievement

(1) Employed as a **Research Assistant (Photonics)** in the Department of Physics, Imperial College, London, 2022.

Workshops attended

(1) FCS 2020 IIT Bombay, Mumbai, India, A National Workshop on Fluorescence And Raman Spectroscopy December 7-12, 2020.

(2) EUROPEAN ADAPTIVE OPTICS SUMMER SCHOOL (Online Mode) - 2021 (https://aoschooleurope.sciencesconf.org/)

(3) Microscience Microscopy Congress 2021 (incorporating EMAG 2021) in Virtual Mode. (https://www.mmc-series.org.uk/)

(4) Online workshop on Software in Mathematics and Statistics (WSMS – 2021) on 02 – 06 August 2021, organized by the Department of Mathematics, National Institute of Technology Tiruchirappalli, India.

(5) Horiba Optical School 2021 in virtual mode, Organized by Indian Association for the Cultivation of Sciences (IACS), Kolkata, and Horiba Scientific India from 06 - 08 September 2021.

(6) North East Research Conclave - 2022, IIT Guwahati, Assam, India.

(7) Research and Industrial Conclave - Integration, 2023, IIT Guwahati, Assam, India.

(8) openScopes Africa (Online Workshop) - 2024.

(9) Research and Industrial Conclave - Integration, 2024, IIT Guwahati, Assam, India.

(10) Workshop on Fluorescence Activated Cell Sorting (FACS): Techniques and Application, 2026, IIT Guwahati, Assam, India.

(11) One-Day Workshop on Dynamic Light Scattering (DLS), March 2026, Jyoti and Bhupat Mehta School of Health Sciences and Technology, Centre for Educational Technology, Online Education and Skilling Section, IIT Guwahati, Assam, India.